Organic and Inorganic Nanostructured Materials as Electrodes for Hybrid Capacitors

by

Sahar Hemmati

A thesis

presented to the University of Waterloo

in fulfillment of the

thesis requirement for the degree of

Doctor of Philosophy

in

Chemical Engineering (Nanotechnology)

Waterloo, Ontario, Canada, 2020

EXAMINING COMMITTEE MEMBERSHIP

The following served on the Examining Committee for this thesis. The decision of the Examining Committee is by majority vote.

External Examiner	**Name:** Dr. Eric McCalla **Title:** Assistant Professor Department of Chemistry, McGill University
Supervisor	**Name:** Dr. Zhongwei Chen **Title:** Professor Department of Chemical Engineering, University of Waterloo
Internal Member(s)	**Name:** Dr. Michael Fowler **Title:** Professor Department of Chemical Engineering, University of Waterloo
	Name: Dr. Ting Sui **Title:** Associate Professor Department of Chemical Engineering, University of Waterloo
Internal-external Member	**Name:** Dr. Xioasong Wang **Title:** Professor Department of Chemistry, University of Waterloo

AUTHOR'S DECLARATION

This thesis consists of material all of which I authored or co-authored: see Statement of Contributions included in the thesis. This is a true copy of the thesis, including any required final revisions, as accepted by my examiners.

I understand that my thesis may be made electronically available to the public.

STATEMENT OF CONTRIBUTIONS

The body of this thesis is based on a combination of both published and unpublished works.

Chapter 4

S. Hemmati, G. Li, Z. Chen. "N-doped interconnected carbon structure from polyaniline as the cathode for hybrid capacitors". (Manuscript under preparation)

- I performed all the experiments.
- G. Li gave me guidance for the data analysis.

Chapter 5

S. Hemmati, G. Li, X. Wang, Y. Ding, Y. Pei, A. Yu, Z. Chen. "3D N-doped hybrid architectures assembled from 0D T-Nb_2O_5 embedded in carbon microtubes toward high-rate Li-ion capacitors". *Nano Energy* **2019**, *56* , 118–126

- I designed all the experiments and data analysis with guidance from G. Li and X. Wang
- Y. Pei helped with some of the half-cell testing and charcterizations.
- G. Li and Y. Ding helped with the review of the manuscript.

Chapter 6

S. Hemmati, K. Kaliyappan, G. Li, M. Mousavi, S. Sy, A. Yu, and Z. Chen. "MoS2 nanosheets anchored to a nitrogen-doped crosslinked carbon structure towards a high-energy sodium-ion capacitor". (To be submitted as it is)

- I designed and performed all the electrochemical testing (half-cell and full cell).
- K. Kaliyappan and G. Li helped with the review of the manuscript.
- M. Mousavi and S. Sy helped with characterizations and designing a schematic, respectively.

ABSTRACT

Global energy demands are expected to continuously grow in the coming decades, while the dominant source of energy remains finite fossil fuels. In addition to this challenge, excessive consumption of fossil fuels has resulted in severe environmental problems. Motivated by these problems, research on the development of electrochemical energy storage and conversion devices, as environmentally friendly alternatives to fossil fuels, has increased drastically.

Even though the high energy density and high power density of, respectively, secondary batteries and electric double layer capacitors allow these devices to drive many advanced technologies, the gap between their electrochemical performances has offered tremendous opportunities for researchers to investigate new chemistries. One exciting approach is to design a device comprised of electrodes with two different charge storage mechanisms: fast delivery of low energy on one electrode, and slow delivery of high energy on the other. This design produces hybrid devices such as lithium-ion capacitors and sodium-ion capacitors, both of which have attracted considerable research attention. On the Ragone plot, the electrochemical performances of these devices are located between those of secondary batteries and electrochemical supercapacitors, meaning that they offer fast delivery of moderate energies.

These devices, however, face several technological obstacles such as unsatisfactory rate performance and limited energy density. Additionally, the cyclability of hybrid capacitors is insufficient. These challenges originate from the slow kinetics of ion insertion or extraction into or from the anode, which is typically an intercalation-type material, and the kinetic imbalance between the electrodes due to the different charge-storage mechanisms that govern the charge storage on the cathode and on the anode. Since the charge-storage performance directly depends on the surface and bulk characteristics of the electrodes, nanocomposites possessing novel

morphological features with doped heteroatoms are needed to enhance these devices' rate performances and energy densities.

To address the problems, research on the electrode materials of hybrid devices has considerably advanced. For the cathode side, the focus has been on designing biomass-derived high specific surface area carbon materials. Moreover, designing nanocomposites that can offer pseudocapacitance mechanism and enhanced electronic conductivity, thus facilitating ion transfer, has been the focus for preparing anode materials. In particular, research on the anode materials for sodium ion devices has become very attractive due to the large availability of sodium resources. Despite the advancement of the hybrid devices in research, however, a set of challenges remains. In response, this thesis, through three studies, attempts to address the difficulties of limited energy density and low rate performance in hybrid devices.

In the first study, a facile approach has been used to prepare polyaniline as a precursor to synthesizing highly porous and nitrogen-doped carbon material. Oxidative polymerization of aniline in the presence of a multidentate acid has been employed followed by annealing and activation. The resulting carbon materials were then optimized and used as the cathode of lithium-ion capacitors and sodium-ion capacitors. Physicochemical characterizations have revealed an interesting interconnected morphology, offering abundant macropores for the electrolyte infiltration and reduction of ion transfer pathways. Moreover, the analysis of specific surface area has revealed the hierarchical structure of the synthesized carbon, with the majority of micropores enhancing the double layer capacitance. Electrochemical half-cell tests, one with lithium and the other with sodium, have shown that the carbon material prepared in this research greatly outperforms commercial activated carbon in terms of specific discharge capacitance. A study of the synthesized carbon’s properties before the activation suggests that this

low surface area scaffold can also serve as a substrate for the deposition of intercalation-type materials to boost the electronic conductivity as well as diffusional properties on the anode side.

In the second study, inspired by the synthesis procedure in the first study, a new nanocomposite of a T-Nb_2O_5/tubular carbon structure was synthesized. For the oxidative polymerization of aniline, the multidentate acid in the first study has been replaced with an acidic precursor of niobium dioxide to yield an in-situ incorporation of T-Nb_2O_5 nanoparticles, a pseudocapacitive material, into a nitrogen-doped tubular carbon structure. The Li^+ storage enhancement has been ascribed to increased electron conductivity and the unique morphology of the composite with its hollow interior and abundant pores. Moreover, according to the calculated pseudocapacitive mechanism contribution to the total charge storage, the fast-electrochemical reaction has benefited from the pseudocapacitive property of nitrogen-doped T-Nb_2O_5.

In the third study, motivated by the need for a sustainable alternative to lithium-ion devices, we searched for a promising anode material for sodium-ion capacitors. Molybdenum disulfide has been selected for investigation. To suppress the volume variation and agglomeration of MoS_2 nanosheets during charge and discharge, nanosheets were deposited on the crosslinked polyaniline scaffold prepared in the first study. The half-cell electrochemical performance has shown an enhanced rate capability compared to that of pure MoS_2. To dig into the underlying cause, the diffusion coefficients of Na^+ in the nanocomposite and the control groups were calculated using galvanostatic intermittent titration technique. The results revealed an increased diffusion coefficient owing to the unique morphological feature of the nanocomposite. Moreover, X-ray photoelectron spectroscopy analysis explained the reason behind the longevity of a full cell NIC, based on MoS_2/NC as the anode and the carbon material prepared in the first study as the cathode, to be the strong interaction between nitrogen moieties and MoS_2.

All the work in this thesis centers around the search and enhancement of electrode materials for hybrid lithium-ion capacitors and sodium-ion capacitors, and yet, plenty of opportunities remain to further extend the knowledge gained here to improve the performance of hybrid devices. As an example, other metal oxides or dichalcogenides can be selected to study the in-situ polymerization of aniline, enabling the resulting carbon structure to boost the electron conductivity of these materials, allowing them to benefit from high power density and high energy density.

ACKNOWLEDGEMENTS

I would like to thank my supervisor, Professor Zhongwei Chen, for believing in me and allowing me to gain experience in different research areas. His support and guidance throughout my studies have helped me to handle the Ph.D. studies' ups and downs. I would also like to thank all of my colleagues in Chen's lab who helped me to explore, learn new things, keep trying, and look ahead during these years. Specifically, I would like to thank Dr. Ge Li, and Dr. Xiaolei Wang for taking the time to have discussions with me. Thanks too to Mary McPherson at the University of Waterloo Writing and Communication Center for helping me to improve my English writing skills. Thanks, Rekha, for always keeping me in your prayers, and thank you, Elnaz, Mina, Maya, Siamak, Kiyoumars, and Altamash for supporting and uplifting me during stormy moments.

I would like to thank my family. Maman, I have, and I always will admire you for who you were. Baba, thank you for always challenging me to step out of my comfort zone. Soheil, thank you for believing in me and always being there for me. Firouzeh, thank you for taking care of me during this journey, and Sina, thank you for giving me hope.

Shervin, thank you for your love and support. Nikki, our toddler, thank you. Everything is a lot more beautiful, joyful, and hilarious when you are around. Thank you for your support, my in-laws, mom, Dr. Espahbod, Arian, and Camelia.

Examining committee membership ii
Author's declaration iii
Statement of contributions iv
Abstract v
Acknowledgements ix
List of figures xiv
List of tables xvi
List of acronyms xvii
1. Introduction 1
1.1. The energy storage challenge 1
1.2. Electrochemical capacitors and pseudocapacitors 4
1.3. Lithium-ion batteries and sodium-ion batteries 6
1.4. Hybrid devices 9
1.4.1. Lithium-ion capacitors (LICs) 10
1.4.2. Sodium-ion capacitors (NICs) 17
1.4.3. Criteria for the material selection 21
2. Thesis objectives 24
2.1. Thesis outline 25
3. Physicochemical and electrochemical characterizations 28
3.1. Electron microscopy techniques and energy dispersive x-ray spectroscopy (EDS) 28
3.2. X-ray diffraction (XRD) 29
3.3. X-ray photoelectron spectroscopy (XPS) 30

3.4. Brunauer-Emmett-Teller (BET) surface analysis 30

3.5. Raman spectroscopy 31

3.6. Half-cell electrochemical evaluations 31

3.6.1. Constant current charge discharge (CCCD) 32

3.6.2. Cyclic Voltammetry (CV) 34

3.6.3. Electrochemical impedance spectroscopy (EIS) 34

3.6.4. Galvanostatic Intermittent titration technique (GITT) 35

3.7. Full-cell electrochemical evaluation 35

4. N-doped interconnected carbon structure from polyaniline as the cathode for hybrid capacitors 37

4.1. Introduction 37

4.2. Experimental 38

4.2.1. Preparation of N-doped high surface area carbon 38

4.2.2. Physicochemical and electrochemical studies 39

4.3. Results and discussion 40

4.4. Summary 49

5. 3D N-doped Hybrid Architectures Assembled from 0D T-Nb_2O_5 Embedded in Carbon Microtubes Toward High-rate Li-ion capacitors 50

5.1. Introduction 50

5.2. Experimental 53

5.2.1. Material synthesis 53

5.2.2. Electrochemical characterizations 55

5.3. Results and discussion 55

5.4. Summary 70

6. MoS_2 nanosheets anchored to a nitrogen-doped crosslinked carbon structure towards a high-energy sodium-ion capacitor 72

6.1. Introduction 72

6.2. Experimental 74

6.2.1. Preparation of crosslinked polyaniline 74

6.2.2. Preparation of MoS_2/NC, MoS_2, AC, and 3D-NC 75

6.2.3. Materials characterization 76

6.2.4. Electrode fabrication and electrochemical measurements 77

6.3. Results and discussion 78

6.3.1. Morphology, structure, and composition of as-synthesized MoS_2/NC 78

6.3.2. Electrochemical properties tied with diffusion coefficient analysis 80

6.3.3. MoS_2/NC//AC: a hybrid high-rate sodium-ion capacitor 88

6.4. Summary 93

7. Conclusions and Future Work 95

7.1. Conclusions 95

7.1.1. N-doped interconnected carbon structure from polyaniline as the cathode for hybrid capacitors 95

7.1.2. 3D N-doped Hybrid Architectures Assembled from 0D T-Nb_2O_5 Embedded in Carbon Microtubes toward High-rate Li-ion capacitors..... 96

7.1.3. MoS_2 nanosheets anchored to a nitrogen-doped crosslinked carbon structure towards a high-energy sodium-ion capacitor..... 97

7.2. Future work 98

7.2.1. Analysis of capacitance fading of hybrid capacitors' cathodes 98

7.2.2. Doping porous carbon materials with pseudocapacitive materials for cathodes 99

7.2.3. Novel composites as hybrid capacitors anodes..... 99

Refrences..... 101

LIST OF FIGURES

Figure 1-1 Illustration of charge storage in EDLCs and pseudocapacitors 4

Figure 1-2 Illustration of lithium-ion charge storage mechanism..... 7

Figure 1-3 Ragone plot for EESs 8

Figure 1-4 Illustration of charge storage mechanism in a hybrid device..... 11

Figure 2-1 Schematic of this thesis work flow 25

Figure 3-1 Illustration of a CR2032 half-cell device 32

Figure 3-2 Differentiating EDLC, pseudocapacitive, and battery materials' electrochemical signature..... 33

Figure 4-1 Schematic for the preparation of polyaniline 39

Figure 4-2 N_2 adsorption/desorption isotherms of NC-800 and NAC-800 41

Figure 4-3 SEM images of (a-b) NC-800 and (c-d) NAC-800-3..... 43

Figure 4-4 Raman spectra for NC800 and NAC-800-3 and N 1s spectrum of NAC-800-3..... 44

Figure 4-5 LIC half-cell performance of NAC-800-3 47

Figure 4-6 NIC half-cell performance of NAC-800-3 48

Figure 5-1 Schematic of the preparation steps for the pseudocapacitive intercalation electrode as anode (N-NbOC)..... 54

Figure 5-2 XRD patterns of N-NbOC and Nb_2O_5, SEM, elemental mapping, HAAD-STEM image and corresponding EELS line-scan profiles, and HRTEM of N-NbOC..... 58

Figure 5-3 SEM images of control groups, (a,b) Nb_2O_5, and (c,d) CP..... 59

Figure 5-4 Raman Spectra of N-NbOC, Nb_2O_5, and CP, and XPS result of N-NbOC 61

Figure 5-5 XPS spectra of Nb 3d for Nb_2O_5..... 62

Figure 5-6 Thermogravimetric analysis of N-NbOC..... 63

Figure 5-7 CV profiles of N-NbOC at 1 mV s^{-1} 64

Figure 5-8 Electrochemical performance of N-NbOC electrode 67

Figure 5-9 Electrochemical performance of N-NbOC//AC 69

Figure 5-10 Ragone plot for the optimization of electrodes ratio and corresponding EIS measurements at OCV. 70

Figure 6-1 SEM images 3D-NC and MoS2/NC-1, TEM image of MoS2/NC-1 and elemental mapping of C, Mo and S and the corresponding SEM image 79

Figure 6-2 XPS spectra of Mo 3d, S 2s core level peak regions in MoS_2/NC-1 and MoS_2, and TGA and DTG curve of MoS_2/NC nanocomposites 81

Figure 6-3 Half-cell electrochecmial performance of MoS_2/NC-1 83

Figure 6-4 Cyclic voltammograms of bulk MoS_2 and MoS_2/NC-2 84

Figure 6-5 Raman spectra for 3D-NC and its relative ratio of I_D to I_G 85

Figure 6-6 Galvanostatic charge/discharge curves of MoS_2, and MoS_2/NC-2 85

Figure 6-7 EIS spectra of MoS_2, MoS_2/NC-2, MoS_2/NC-1 electrodes 86

Figure 6-8 GITT program steps during discharge and charge 90

Figure 6-9 GITT curves of MoS2/NC-1 and diffusion coefficients of all samples 89

Figure 6-10 Full cell electrochemical performance of MoS2/NC-1//AC and the Ragone plot of the prepared NIC device 92

Figure 6-11 Galvanostatic charge/discharge for MoS_2/NC-1//AC with presodiated anode. 93

Figure 6-12 Comparison of the charge stored in MoS_2/NC-1//AC with and without presodiation 93

LIST OF TABLES

Table 1-1 Capacitive electrodes as cathodes of LICs 18

Table 1-2 Insertion electrodes as anodes of LICs 19

Table 1-3 Recent NIC devices 23

Table 4-1 Electrochemical performance of NAC samples and their surface area analysis 42

LIST OF ACRONYMS

EDLCs – Electric double-layer capacitors

LICs – Lithium-ion capacitors

NICs – Sodium-ion capacitors

LIBs – Lithium-ion batteries

NIBs – Sodium-ion batteries

AC – Activated carbon

Pani – Polyaniline

CNT– Carbon nanotube

TMDs – Transition metal dichalcogenides

CV – Cyclic voltammetry

CCCD – Constant current charge/discharge

DDI – Distilled de-ionized water

EDS – Energy dispersive X-ray spectroscopy

EES – Electrical energy storage

PVDF – Poly (vinylidene fluoride)

SEM – Scanning electron microscopy

STEM – Scanning transmission electron microscopy

TEM – Transmission electron microscopy

TGA – Thermogravimetric analysis

XPS – X-ray photoelectron spectroscopy

XRD – X-ray diffraction

BET – Brunauer-Emmett-Teller

1. Introduction

1.1. The energy storage challenge

The world's growing demand for energy over the past decades is leading to a critical fossil fuel shortage as most of the current energy requirement is fulfilled from combusting fossil fuels. According to the *International energy outlook* presented by the U.S Energy Information Administration (EIA), energy consumption will grow by 56% between 2010 and 2040. Moreover, energy-related greenhouse gas emission will rise by 46% in that period causing warming seas, rising coastlines and localized air pollution.[1] These paramount concerns about the fossil fuel depletion and environmental crisis have directed many researchers to put significant efforts on harnessing safe, clean, and renewable energy resources. Accordingly, there is an essential need for the proper storage and subsequent delivery of energy. Electrochemical energy storage systems such as lithium-ion batteries (LIBs) and electrochemical double-layer capacitors (EDLCs) are among the most developed and widely distributed energy storage devices.[2] Similarly, sodium-ion batteries (NIBs) have been extensively studied due to the wide accessibility of raw materials, offering an in-expensive energy storage option.[3]

Although LIBs can provide high gravimetric and volumetric energy densities, slow kinetics in their electrodes results in low or moderate power densities of~1 kW kg^{-1}. Likewise, NIBs show poor rate capabilities. On the other hand, EDLCs possess excellent power capability and cycle life but mediocre energy density (5-10 Wh kg^{-1}).[2] Batteries and supercapacitors are known as mutually complementary systems. The battery/supercapacitor hybrid energy systems have been proposed for large-scale applications such as electric and hybrid electric vehicles (EV, HEV) in which the capacitive storage propels the car during acceleration when the high-power operation is

necessary, and stores energy from regenerative braking. The battery supplies energy during lower-power cruising.[4] Unifying these high-power and high-energy systems into hybrid capacitors is a recent development that has attracted researchers' attention.

Hybrid capacitors possess higher energy density than EDLCs and have a higher cycle life and power density than Li/Na-ion batteries. Li-ion capacitors (LICs) and Na-ion capacitors (NICs), more specifically, utilize an intercalation-type anode and the cathode of EDLCs, which are electrically separated. A lithium/ sodium-based salt in organic solvents is employed as the electrolyte. The storage mechanism on the cathode is the adsorption/desorption of charges, while ion intercalation/deintercalation or fast surface reactions take place on the anode.[5,6]

Since the charge storage mechanism on the cathode relies on the electrostatic separation of charges, large surface area carbon materials such as activated carbon and graphene are commonly used as cathodes. The materials used for anodes include carbon-based materials, metal oxides, metal nitrides, and their composites.[7,8] Since the introduction of hybrid capacitors by Plitz et al.,[9] two approaches have been pursued to further improve their performance: (1) widening the operating potential by rational selection of electrodes to enlarge the operating potential and electrolytes with broad operating voltage, and (2) Increasing the charge storage capacity by designing novel materials for the positive and negative electrodes. In the first approach, the electrolyte electrochemical voltage window must be considered to avoid the decomposition of the electrolyte. The difference in the chemical potential of each electrode is another factor determining the working potential of the capacitor cell. For the second approach, many studies have tried to improve the anode's anode, oxide materials such as V_2O_5,[10], Nb_2O_5,[11] TiO_2,[12] TiP_2O_7,[13] $Li_4Ti_5O_{12}$[14] and their composite with carbon nanostructures; however, very few studies have focused on improving the capacity on the cathode side. Therefore, more in-depth research effort is

required in this area to design novel carbon-based materials with higher capacity, without lowering the life cycle and power density.

Ultrahigh surface area carbon materials with optimized pore size distribution and pore volume are known to significantly affect the performance of hybrid capacitors through advancing the electrical double layer capacitance on the cathode side.[15] Heteroatom doping can further enhance the capacity by fast reversible surface reactions, known as pseudocapacitive behavior. Heteroatom doping can also affect the interaction between the electrolyte and electrode, thus influencing the wettability of the electrodes toward a higher capacity and lower equivalent series resistance.[16] It is also well established that the electrolyte diffusion within the bulk electrode materials is one of the major rate-limiting factors influencing the performance of these devices. Therefore, the electrolyte transport paths must be optimized without sacrificing electron transport. In this regard, a templating method to provide mesoporosity to the system is drawing considerable attention as it provides desirable electrode materials with intriguing properties such as electrical conductivity, chemical inertness, high surface area, and uniform pore size.[17]

Electrochemically active metal oxides integrated with carbonaceous nanostructures have been widely investigated, as they supply high energy density through faradaic reactions using their different electronic states. Additionally, the presence of a graphitized carbon framework is believed to mitigate the conductivity and stability problems with these materials. As a result, designing novel hybrid materials is a matter of ongoing research. Evaluating the physicochemical and electrochemical characteristics of heteroatom-doped high surface area carbon framework, templated carbon framework and metal oxides, this research aims to design and develop novel electrode materials with enhanced performance towards charge adsorption/desorption at the cathode and Li/Na ion storage at the anode in hybrid organic capacitors.

1.2. Electrochemical capacitors and pseudocapacitors

EDLCs, also referred to as electrochemical supercapacitors, utilize the interfaces between electrodes and the electrolytes for energy storage, by employing electrostatic separation and accumulation of charged ions. In fact, the energy of these devices is stored in the electrical double layer in the solution and electrode surface interface, thereby balancing the charge. Most EDLCs are comprised of porous carbonaceous materials that act as electrodes, aqueous or organic electrolytes, and porous separators. More than 80% of the commercially available supercapacitors are fabricated based on the high surface area carbon materials, because they are abundant, highly conductive and cost-efficient.[18,19] The mechanism of charge storage for EDLCs is included in **Figure 1-1.**

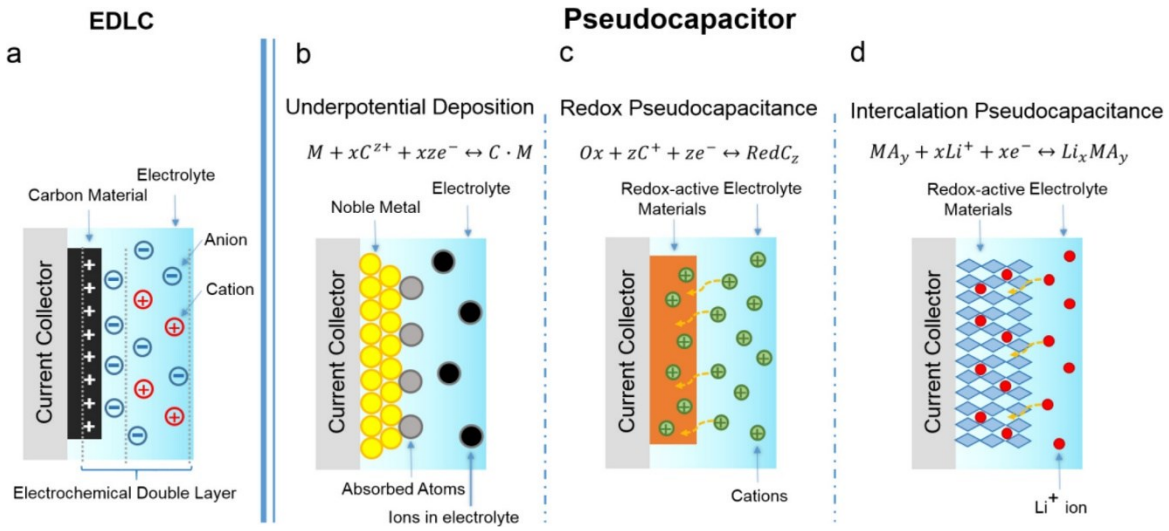

Figure 1-1 Illustration of charge storage in (a) EDLCs, and (b-d) in capacitive pseudocapacitors with permission from Ref. [20].

During the application of an external load (charging), electrolyte ions migrate to the micropores of the negative or positive electrode depending on the type of ions and the electrons migrate from the negative electrode to the positive electrode through the external circuit; the reverse process

takes place during discharge. No redox reaction is involved in this mechanism.[19,21] Since the ion adsorption and desorption are fast surface processes, EDLCs can provide high-power and long-term cycling stabilities. The capacitance of the supercapacitors can be calculated from the following equation:[19]

$$C = \frac{\epsilon_r \epsilon_0 A}{d} \qquad (1\text{-}1)$$

Where ε_r represents the permittivity of the electrolyte, ε_0 is the permittivity of the vacuum, A is the interface area of the electrodes and the electrolyte interface and, *d* is the Helmholtz double layer. According to equation 1-1, one can significantly increase the capacitance by designing nanostructures with abundant pores and ultrahigh surface area. At the current state, EDLCs display a much higher power delivery (1–10 kW kg^{-1}) when compared to LIBs (150 W kg^{-1}). Moreover, EDLCs possess very high capacity retention (90%) even after many cycles (>10,000).[7] The life expectancy for EDLCs is estimated to be up to 30 years, compared to 5 to 10 years for LIBs. However, their energy density is far from satisfactory compared to that of LIBs, as, unlike in LIBs, the bulk material of EDLCs is not involved in the storage mechanism. The highest energy storage density of commercially available activated carbon-based EDLCs is 12 Wh kg^{-1}, an order of magnitude smaller than that of LIBs.[22]

Another type of electrochemical capacitors is called pseudocapacitors. Their charge storage mechanisms are very different from the EDLCs', however they show a very similar electrochemical features to EDLCs.[23] According to Conway, there are three types of faradaic mechanisms that results in capacitive behavior (shown in Figure 1-1).[19] The first one is underpotential deposition, during which metal ions' monolayers are adsorbed on the metal's own surface at a potential less negative than its Nernst reduction potential. Second is the Redox

pseudocapacitance, which is a Faradaic charge transfer at or near the surface of material. The other mechanism is intercalation pseudocapacitance, which occurs when ions intercalate into the crystalline layers of a material, followed by charge transfer reaction with no phase change.[19,24] The relationship between the capacitance and the interface between electrolyte and electrodes follows that of EDLCs, thus down-sizing the electrode structure to achieve high surface area is a common strategy to enhance these material' energy density.

1.3. Lithium-ion batteries and sodium-ion batteries

Charge storage in LIBs relies on the Li^+ insertion/ extraction into and from the electrodes, or alloying/dealloying of Li with negative electrodes.[25,26] LIBs have been successfully commercialized since 1991 and have been used in portable and stationary instruments. The most widely commercialized anode material for these devices is graphite, wherein Li^+ occupy the interstitial sites between every hexagonal ring of carbon atoms in the form of LiC_6, which has a theoretical storage capacity of 372 mA h g^{-1}. $LiCoO_2$ has been employed as the cathode material in commercialized cells due to its high Li^+ storage capacity (120 mA h g^{-1}). A separator immersed in a Li salt-containing organic electrolyte such as $LiPF_6$ separates the anode from the cathode. During charging, Li^+ are extracted from the $LiCoO_2$ and liberated to the electrolyte with concomitant oxidation of Co_3^+ and Co_4^+. Simultaneously, Li^+ uptake occurs at the anode to form a Li_xC_6 compound. The electrons at the positive electrode pass through the external circuit to reach the anode. The reverse occurs during discharge, as illustrated in **Figure 1-2**.[27]

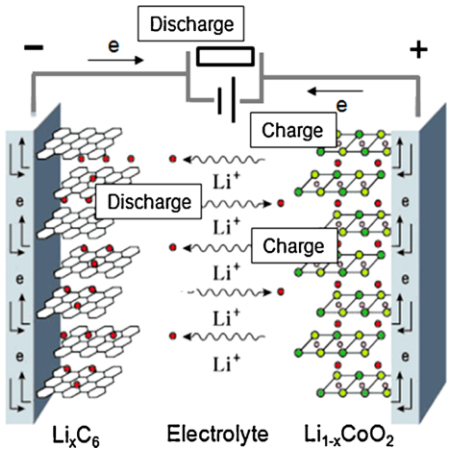

Figure 1-2 Illustration of lithium-ion charge storage mechanism with permission from Ref. [27].

The corresponding reactions at both electrodes are shown in the following:

$$LiCoO_2 \leftrightarrow Li_{1-x}CoO_2 + xLi^+ + xe^- \quad (1\text{-}2)$$

$$C + xLi^+ + xe^- \leftrightarrow Li_xC \quad (1\text{-}3)$$

with a stoichiometry close to LiC_6 when fully charged.[28] Other existing materials involved in commercial LIBs are typically $LiCoO_2$, $LiMn_2O_4$, $LiFePO_4$ for the cathode; Graphite, $Li_4Ti_5O_{12}$ for the anode; ethylene carbonate (EC), dimethyl carbonate (DMC), $LiPF_6$, $LiBF_4$, $LiClO_4$ as the electrolytes/salts; and polypropylene, polyethylene as the separator.[29]

The challenges with these devices are relatively low power density and inferior cycle life, originating from the intrinsically sluggish ion diffusion into electrode bulk; the typical charging time of LIBs is in hours while EDLCs can be charged in seconds. Additionally, during lithiation/delithiation or alloying/dealloying, electrodes experience mechanical stress because of the volumetric change and structural phase transitions, resulting in a capacity loss. Since our

society is addicted to power, these challenges are the focus of many studies.[30,31] The power/energy trade-off of electrochemical devices is plotted in a so-called Ragone plot (**Figure 1-3**).

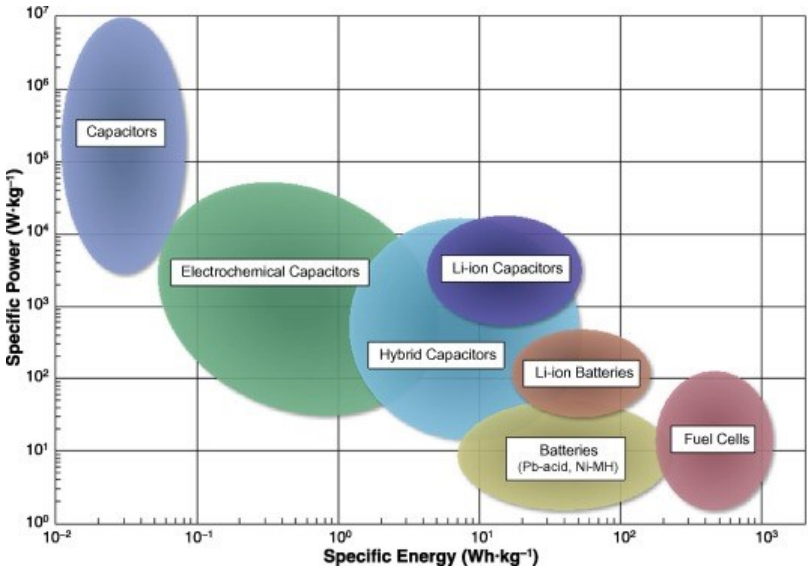

Figure 1-3 Ragone plot for EESs with permission from Ref. [32].

Energy storage research generally focuses on moving every device's performance closer to the upper right-hand corner of the Ragone plot. For capacitors, increasing specific energy is crucial and remains a challenge. For batteries, many directions are currently being pursued to enhance the performance, including the development of high-energy electrode materials such as silicon anodes and high capacity Li-rich cathodes.

Sodium-ion batteries have also received a great attention due to larger global abundance of sodium than that of lithium. In fact, sodium resources considered as "infinite" in some studies. With this incentive and the fact that Li^+ and Na^+ have similar insertion chemistry, research focus has been shifted to NIBs and the number of published papers was rapidly increased by five-fold between years of 2012 and 2018.[33] Similar to LIBs, NIBs operate based on electrochemical reactions that occur between the cathode that is sodium-containing layered materials, and the

anode that is usually made of hard carbon. A separator between the two electrodes allow ionic flow and are immersed in an electrolyte with organic solution containing salts such as $NaClO_4$ or $NaPF_6$.[34] During charge Na atoms in the cathode release electrons to the external circuit and Na^+ in the electrolyte migrate to the anode, where they react with the layered anode material; the opposite process occurs during the discharge. Slow kinetics, poor rate capabilities, and short cycle life are the major challenges that need to be responded to.[3,35]

In response to the inferior power density and cycle life of batteries and low energy density of EDLCs and pseudocapacitors, hybrid devices, and more specifically, Li-ion capacitors (LICs) and Na-ion capacitors (NICs) are receiving considerable interest, because they mitigate LIBs, NIBs, and EDLCs weaknesses while combining their distinct advantages to bridge the gap between these devices.[36] Hybrid capacitors can take advantage of the faradaic energy storage mechanism on the anode to boost the energy density while improving the electrochemical performance at high rates by using a capacitive electrode as the cathode.

1.4. Hybrid devices

Electrochemical supercapacitors are classified into symmetric or asymmetric electrode configurations. Symmetric devices use identical electrodes for their anodes and cathodes, whereas asymmetric devices have significantly different capacitance values for each electrode.[8] The advantage of using asymmetric systems is in their additional electrochemical potential difference, which boosts operating potential and provides higher energy density due to the faradaic redox mechanism on the battery type electrode.[18] As an example, Wu et al. fabricated a high energy density asymmetric supercapacitor using MnO_2 nanowires and graphene, with an energy density of 30.4 Wh kg^{-1}. The authors explain that symmetric supercapacitors show much lower energy

density than the asymmetric device (2.8 Wh kg-1 for graphene/graphene and 5.2 Wh kg-1 for MnO_2/MnO_2 configurations).[37] Hybrid devices, associated with asymmetric devices, refer to devices that store energy using a combined charge-storage mechanism: Faradaic and electrical double layer capacitance (mainly capacitive at the positive and pseudocapacitive or faradaic at the negative electrode).

One advanced type of the hybrid capacitors is organic metal-ion capacitors, in which carbon-based electrodes are implemented as the cathode and metal oxides or intercalation material as the anode. Li/Na-salt containing organic electrolytes such as 1 M $LiPF_6$/ 1M $NaClO_4$ in EC/DMC are used as the electrolyte.

1.4.1. Lithium-ion capacitors (LICs)

One of the earliest LICs, patented by Amatucci et al. in 2001, was made of a nanostructured $Li_4Ti_5O_{12}$ (LTO) anode and an activated carbon cathode (AC), providing an energy density of 20 Wh kg^{-1} and bridging the gap between LIBs and EDLCs.[38] LICs have been commercialized by *JM* E*nergy* containing graphite as the anode and activated carbon as the cathode and operate such that during a load application, Li-ions migrate through the electrolyte and intercalate into the negative electrode (graphite layers to form LiC_6), when the device is fully charged (**Figure 1-4**). At the same time, PF_6 anions adsorb on the surface of the activated carbon and electrons pass through the external circuit to combine with the intercalated Li-ions at the negative electrode. The reverse occurs during discharge. [39,40] Equations (3) and (4) illustrate the reactions that take place on the activated carbon (AC) and graphite.[41]

$$AC + PF_6^- \leftrightarrow AC^+.PF_6^- + e^- \quad (3)$$

$$C + xLi^+ + xe^- \leftrightarrow Li_xC \quad (4)$$

Currently, the commonly used cathode materials for this technology are AC, carbon nanotubes, and graphene. The conductivity, surface area, and pore size distribution (PSD) for these capacitive electrodes are the critical factors influencing the capacitance. Several other capacitive and pseudocapacitive electrodes will be discussed later. It is worthwhile mentioning that cathode materials for LICs need a high rate capability and long cycle life. The insertion type electrodes commonly used as anode materials for these devices are graphite and LTO, offering high energy density and power density for the cell, respectively. For example, Lee et al. fabricated a full cell based on activated carbons as a cathode, and LTO as the negative electrode. The device delivered a capacitance of 209 F g^{-1}; however, conductivity quickly became an issue as internal resistance increased when LTO was delithiated.[41]

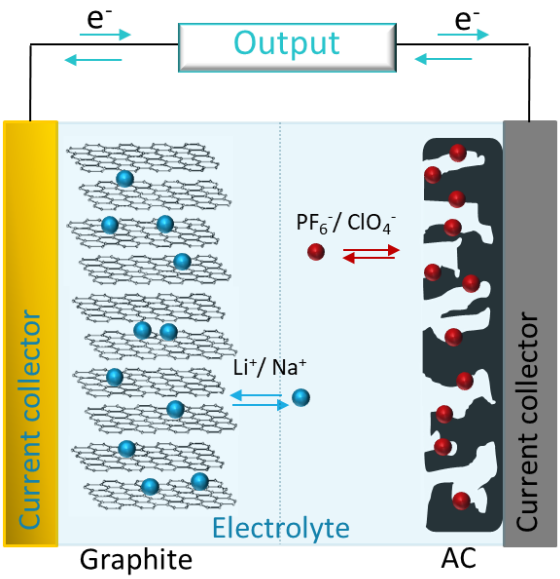

Figure 1-4 Illustration of charge storage mechanism in a hybrid device

The frequently implemented aqueous electrolytes are alkaline sulfates, hydrate, or nitrates such as $LiSO_4$, LiOH, or $LiNO_3$. Aqueous electrolytes have higher ionic conductivity than organic electrolytes; however, they have only narrow electrochemical potential (less than 1.2 V, due to water electrolysis). In contrast, organic-based electrolytes provide considerably higher energy

density as they possess a wider electrochemical window (up to 3 V). In these systems, the most commonly used electrolyte is $LiPF_6$ in an organic solvent, EC, and DMC.[42]

Separators are located between the two electrodes to prevent the short circuit and are generally made of cellulose, polymer membranes and glass fibers. Current collectors are other components of electrochemical cells and have been used to enhance the contact of the electrode materials within the cell. Typical current collectors that are compatible with organic electrolytes are aluminum or carbon-coated aluminum foil for cathode and copper foil for anodes.[42]

Developing the storage capacity and energy density of LICs has become a crucial area of research since, in their present states, LICs have compromised power density and cycle life due to striving for increasing energy density. Several strategies have been suggested to enhance the performance of these devices, such as enhancing the capacity storage of their electrodes, the capacitive materials for cathode and pseudocapacitive or insertion type materials for anode.[43] It is worthwhile to mention that balancing the capacity of the electrodes by varying the mass loading is critical, as the capacity of the anode is significantly higher than that of the cathode.

1.4.1.1. Electrode materials as the cathode

This section reviews the literature on progress made in the field of capacitive electrode technologies, which is the main focus in selecting cathode materials. Table 1 summarizes several cathode materials reported as cathodes for LICs.

Several carbon structures can be employed in LICs, such as activated carbon (AC), carbide-derived carbon (CDC) and graphene. These structures can provide a long-life cycle and excellent conductivity but limited specific capacitance. One effective strategy for enhancing the specific capacitance is to design high surface area and large pore volume carbon materials. Highly porous materials enlarge the double layer capacitance by improving the contact between electrodes and

electrolyte; moreover, large pore volume facilitates the accessibility of ions to the active sites. Therefore, optimizing pore size has a substantial impact on the charge storage capability of the carbon materials. Templating techniques and chemical activation are the two major approaches for creating macro (pore size larger than 50 nm) meso (pore size of 2-50 nm) and micropores (pore size less than 2 nm).[44,45]

Chemical activation of carbon-based materials using KOH is a broad strategy for creating high surface area carbon-based materials. The activation of carbon with KOH in an inert environment at high-temperature proceeds as $6KOH + C \rightarrow 2K + 3H_2 + 2K_2CO_3$, followed by decomposition of K_2CO_3 and/or reaction of $K/K_2CO_3/CO_2$ with carbon, resulting in abundant pores in the carbon products.[45] This approach delivers mostly micropores and mesopores with a surface area of up to 3175 $m^2 g^{-1}$.[46]

Introducing heteroatoms to functionalize porous carbon is a promising strategy to enhance the limited capacitance and benefit from pseudocapacitive behavior. Pseudocapacitors exhibit a linear dependence between charge storage and potential, similar to ideal capacitors, yet, with a very different charge-storage mechanism. Unlike EDLCs, pseudocapacitors involve a fast-reversible redox reaction at the electrode surface and the passage of electrons across the double layer. As a result, a pseudocapacitor generally stores more charge than EDLCs. The major difference between batteries and pseudocapacitive materials is in the charging and discharging time scale, which is approximately within seconds and minutes for pseudocapacitive materials.[47]

The mechanism by which heteroatoms contribute to the increment in capacity has not been clearly explained. It has been suggested that the heteroatoms in a carbon matrix can significantly change the electron/donor characteristics of the carbon electrode material, thereby introducing pseudocapacitive behavior. Moreover, functional groups improve the wettability of pore walls.

Some recent studies also suggest that heteroatom doping can increase the conductivity of porous carbon materials. Nitrogen, boron, phosphorus, and sulfur are the heteroatoms that could potentially be employed in metal-ion capacitors.[48,49]

Nitrogen has been the most extensively heteroatom studied for modifying surface properties of the carbon materials in supercapacitors. Nitrogen atoms can act as electron donors, resulting in a shift of the Fermi level in carbon electrodes. Also, nitrogen-doping can enhance the capacitance of carbon-based materials due to a fast redox pseudocapacitance contribution. Another effect of the presence of heteroatoms is the increased wettability of the electrodes. Nitrogen doping can be achieved using heat treatment of the carbon-based material with ammonia or urea.[49] As an example, Li et al. prepared nitrogen-doped activated carbon using biomass as the carbon precursor and heat treatments in NH_3 atmosphere to introduce nitrogen doping.[16] The capacity reported for the device is 189 F g^{-1} at 0.4 A g^{-1} in an organic electrolyte which is significantly higher than that of activated carbon (40-100 F g^{-1}) in organic electrolyte.[7] In addition, nitrogen can be intrinsically present in the carbon structure when nitrogen-rich precursors such as polyaniline, polypyrrole, and polyacrylonitrile or some biomass are employed.[50,51]

1.4.1.2. Electrode materials as the anode

Several insertion-type electrodes as anodes such as carbonaceous materials with various morphologies have been proposed to construct high-performance LICs. Aida et al. used graphite as the anode and AC as the cathode for a LIC device, and the device is reported to deliver power and energy density of 8.5 kW L^{-1} and 81.4 Wh L^{-1}, respectively, showing higher energy density than that of EDLC (15.8 Wh L^{-1}).[52] Aside from graphite, hard carbon has also been employed for LICs. The energy density of Graphite/AC cell outperforms the energy density provided by the hard

carbon/AC cells. However, the cell's rate performance containing hard carbon is superior (70% of the initial capacity at a 40C rate).[53]

Few studies suggest using polyanions as anode compounds for LICs with different anionic groups such as phosphates (TiP_2O_7). For example, Aravindan et at. synthesized TiP_2O_7 with a cubic structure.[13] CV curves show a reversible Li-ion intercalation and deintercalation at 2.54 V and 2.67 V in the half-cell system versus Li/Li+. The discharge capacity in a full cell containing TiP_2O_7 for anode and AC as a cathode in the organic electrolyte at 30 mA g^{-1} is 29 F g^{-1}, which is even lower than the symmetric device with AC electrodes. Overall, there are no polyanions-based materials as electrodes for LICs' electrodes studied in the literature that can compete with AC-based materials.

Metal oxides are the most widely investigated insertion-type electrode materials in LICs. They possess high theoretical capacity and high voltage output within 1 to 4 V vs. Li/Li^+. Table 2 summarizes several types of the metal oxides as anode materials and their performance. Metal-ion capacitors prepared from transition-metal oxides are predicted to have a high capacitance while they are inexpensive and environmentally friendly. In addition, they can provide enhanced energy density, however, with sacrificing the power density due to poor electrical conductivity. The also show inferior cycling performance compared to carbon materials as their crystal structure undergo volume change during lithium insertion/extraction. To tackle these problems, many studies have focused on composite materials made of carbonaceous materials and metal oxides.[53] V_2O_5,[54] Nb_2O_5,[55] TiO_2,[56] are several metal oxides that have been integrated into hybrid electrode materials for LICs. V_2O_5 as an example has a high capacity of 443 mA h g^{-1} when three Li ions are inserted into the host lattice, and 294 mA h g^{-1} when two Li-ions are intercalated into the lattice. This material is also attractive because of its layered structure, ease of preparation, high output voltage,

and capability to accommodate the reversible intercalation of lithium ions in organic solutions. Challenges associated with this material are mainly structural instability due to volumetric expansion, poor conductivity, and ion diffusivity of electrode materials. Therefore, bringing the size of V_2O_5 particles to nanoscales and coating with carbon materials can relatively solve these problems.[54,57] For instance, Nagaraju at al. synthesized a two-dimensional composite of V_2O_5 nanosheets and reduced graphene oxide. They reported that the composite electrode's energy density of 79.5 Wh kg^{-1} at 900 W kg^{-1} is 2.5 times higher than V_2O_5 electrodes' energy density, concluding that the reduced graphene oxide significantly contributes to the conductivity of the LIC cell.[58]

Recently, researchers have also shown an increased interest in niobium pentoxide, Nb_2O_5, as one of the promising materials for LICs. It has high theoretical capacity (200 mA h g^{-1}) and slight structural changes during intercalation/deintercalation, which provide an excellent power performance. Moreover, it possesses high potential window, which can prevent the formation of lithium dendrites. However, the low conductivity of the metal oxide has led researchers to design hybrid nanocomposites of Nb_2O_5 and conductive materials. As an example, Wang et al. uniformly encapsulated Nb_2O_5 in ordered mesoporous carbon (CMK-3), using the hard-templating method and $NbCl_5$ for the Nb_2O_5 precursor. The resulting orthorhombic 20% Nb_2O_5/CMK-3 composite delivers the capacity of 243.6 mA h g^{-1} within the potential window of 1-3 V vs. Li/Li^+ at 0.2C in a half-cell test. Their synthesis methodology includes impregnation of $NbCl_5$ into CMK structure followed by a combination of drying, heat treatment at high temperature (700°C) in an inert environment, and calcination at 300°C in air. According to their result, the capacity retention of the LIC device is 87% of the initial capacity after 1000 cycles. In another study, Murugan et al. employed the hydrothermal method to prepare a nanocomposite containing Nb_2O_5 nanoparticles

and reduced graphene oxide. In the half-cell test, the cell delivers capacitance of 321 F g^{-1} (equal to 267.5 mA h g^{-1}) at the scan rate of 10 mV s^{-1} with 86% capacity retention after 500 cycles.[59] Although the author claims the uniform dispersion of the Nb_2O_5 nanoparticles, SEM images reveal distributed aggregates.

1.4.2. Sodium-ion capacitors (NICs)

Although the number of research on NIBs has been considerably increased, research on NICs is in its infancy. The first published work on NICs in 2012 introduced interpenetrated carbon nanofibers/ V_2O_5 nanowires as the anode and commercial AC as the cathode, outperforming EDLCs in terms of energy and power densities, but not cyclability.[60] NICs have similar components to LICs, containing a capacitive cathode, an insertion type material as the anode, and a separator soaked in organic electrolytes with $NaPF_6$ or $NaClO_4$.[36] In the following section, several examples of the electrodes is given.

Table 1-1 Capacitive electrodes as cathodes of LICs

Electrode	Surface area, $m^2 g^{-1}$	Practical capacity or capacitance Half-cell testing (Li metal as reference and counter electrode)	Energy density Wh kg^{-1}	Power density W kg^{-1}	Capacity Retention/ cycles
			Full cell anode		
N-doped activated carbon from corncob[16]	2852	129 mA h g^{-1} at 0.4A g^{-1} 2-4.5V vs. Li/Li^+	Max:230 Si/C	1747	76% /8000
Activated carbon from coconut shell[15]	1652	120 $F.g^{-1}$ at 0.1 A g^{-1} 3-4.6 vs. Li/Li^+	69 $Li_4Ti_5O_{12}$	-	80% /2000
Pani/ $Li(Mn_{1/3}Ni_{1/3}Fe_{1/3})O_2$ [61]	57	-	Max 49 AC	3000	90%/1000
Activated exfoliated graphene oxide[62]	3100	130 mA h g^{-1} at 1.1 A g^{-1} 2.7 V (Symmetric)	40.8 $Li_4Ti_5O_{12}$	-	-
Activated graphene[63]	3290	19 mA h g^{-1} at 4.2 Ag^{-1} (symmetric) 0-3.5 V (ionic liquid)	Max:74 Symmetric device	33800	94%/ 1000
3D porous graphitic carbon[50]	4073	225 F g^{-1} at 0.5 A g^{-1} 2.7 V (Symmetric)	- Symmetric device		96%/10000
Carbon from poly (acrylamide-co-acrylic acid) potassium salt[64]	1490	123 F g^{-1} at 0.1 A g^{-1} 3-4.6 vs. Li/Li^+	5 $Li_4Ti_5O_{12}$		87% /2000
Zeolitic imidazolate framework-8 (ZIF-8)[65]	1110	168 F g-1 at 0.1 A g-1 2.5-4 vs. Li/Li+	100 Ni/NiO/C	100	87%/12000

Table 1-2 Insertion electrodes as anodes of LICs

Nanocomposites	Morphology	Practical capacity Half-cell testing (Li metal as reference and counter electrode), mA h g^{-1}	Energy density Wh kg^{-1}	Power density W kg^{-1}	Capacity Retention /cycles
			Full-cell cathode		
V_2O_5[10]	Nanofibers	316 at 0.1 C rate 1.75-4 V vs. Li/Li^+	18	at 315	80% /3500
			SWCNT		
V_2O_5-rGO[57]	Nanoparticles	129.7 at .1 A g^{-1} -0.8-0.8 V vs. Ag/AgCl	Max: 13.3	Max: 625	85% /8000
			Free standing rGO		
MnO/CNS[66]	Nanoparticles	567 at 5 A g^{-1} 0-3 V vs. Li/Li^+	90	Max:15000	76% /5000
			CNS		
Anatase TiO_2[12]	Microsphere	148 at 0.2 A g^{-1} 1-3 V vs. Li/Li^+	42	800	80% /100
			AC		
TiO_2 decorated LTO[14]	Nanosheets	-	74.8	300	92.3% / 3000
			N-CNT		
Nb_2O_5@Carbon[11]	Core-Shell	180 at 0.05 A g^{-1} 1.1-3 V vs. Li/Li^+	Max: 63	Max:16528	-
			AC		
Niobium nitride (NbN)[67]	Cubic crystals	332 at 0.1 A g^{-1} 0.01-3 V vs. Li/Li^+	149	200	95% /15000
			AC		
Carbon nanofiber/T-Nb_2O_5	Nanofibers/ nanoparticles	120 at 1 A g^{-1} 1.2-3 V vs. Li/Li^+	80	180	80%/ 35000
			AC nanosheets		

1.4.2.1. Electrode materials as cathodes

Since the operation principle on the cathode side in NICs is like that of LICs, ideas on how to develop a high-performance cathode for NICs have been mostly borrowed from LICs' cathode literature. The most common cathode materials for NICs is activated carbon possessing high surface area (~ 3000 m^2 g^{-1}) and average pore diameter of 2 nm. This property is beneficial for electrolyte diffusion and the large double layer separation of charge. Additionally, AC is a stable material within 1-4.3 V vs. Na/Na^+ in organic electrolytes containing $NaClO_4$. Biomass or polymer-derived activated carbon is reported to show higher capacitance values due to presence of doped heteroatoms (such as N and S atoms) that offer fast surface processes, contributing to the total capacitance of the electrode.[68,69]

Since the Na^+ storage capacity of AC is limited (about 50 mA h g^{-1}), some research work has been focusing on using layered pseudocapacitive or insertion materials as cathodes of NICs. For instance, Wei et al. suggested layered ferric vanadate nanosheets as the cathode and employed hard carbon as the anode for a NIC device.[70] Although the device shows an excellent energy density at high rates, delivering a 100 Wh kg^{-1} in 6 minutes, the capacity retentions drop to ~65% only after 800 cycles. This poor capacity retention challenges the advantages of using layered materials as cathodes for capacitors. Other insertion-type materials from NIBs literature have also been tried as NICs' cathodes, including $Na_2Fe_2(SO_4)_3$ with theoretical capacity of 120 mA h g^{-1}, and V_2C-MXene with wide working potential window.[71,72] However, the cycling stability cannot meet the requirement for capacitors device due to the intrinsically slow and irreversible chemical reactions in these types of materials. Accordingly, AC materials still hold promise for NICs as they can provide moderate capacity and long cycle life.

1.4.2.2. Electrode materials as anodes

Most of the research work on NICs that published in the past few years have been focused on anode materials with attempts to increase the rate capability of Na^+ insertion. For instance, hard carbons (HCs) synthesized by the pyrolysis of carbon sources such as polymers or sustainable biomass has been suggested as the anodes for NIBs and NICs.[69,73] HCs with graphene-like carbon layers and abundant nano-size pores have shown promising and reversible Na^+ insertion with the capacity of 300 mA h g^{-1}. Nevertheless, HCs applied in NICs has shown inferior capacity retention compared to when it was used for LICs with the identical cathode as the NIC.[74] Jayaraman et al. synthesized natural plant-based hard carbon and tested its Na^+ and Li^+ storage properties against AC as the cathode, synthesized from the coconut shell. They concluded that although HCs can offer a high energy and power density NIC device, the cycling stability drop to 60% only after 2000 cycles, raising doubts about the benefits of using HCs as the anode of NICs.[75]

Several layered oxide materials and their composites with carbon materials have been studied as the anodes.[60,76–78] As an example, $NiCo_2O_4$, as the anodes for NIBs, can provide an exceptional capacity of 890 mA h g^{-1}, however, as the NIC anode, can only provide 20 F g^{-1} due to small layer distance that could not accommodate the Na^+ insertion.[76] Table 3 summarizes some of the recent reported NIC devices.

1.4.3. Criteria for the material selection

As discussed earlier, selection of each component of the hybrid devices such as the cathode and the anode strongly affect the electrochemical performance. Selection of the electrode materials for anode and cathode is limited by the electrochemical potential window of the electrolyte. The chemical potential of anode should fall below the lowest unoccupied molecular orbital (LUMO) and the chemical potential of the cathode should be located higher than the highest occupied

molecular orbital (HOMO) of the electrolyte. Selection of cathode has been limited to highly porous carbon-based materials in which the storing of charge mechanism relies on the separation of charges but not faradic reactions.

Constraints influencing material selection for anodes stems from capacity fading of these materials due to the volume change during Li^+/Na^+ insertion/extraction. Also, high redox voltage of the couples in metal oxides such as $Co^{2+/3+}$ in $LiCoPO_4$ results in larger capacity fading. The low working potential of some of the anode materials is another constraint for the material selection as the formation of lithium dendrites at low potential causes strong capacity fading and severe safety concerns.

In the design of these devices, Simon et al.[2] determine two specific characteristics: (1) a linear time-dependent change in potential, and (2) a cyclic voltammogram with no apparent redox peaks. This will limit the selection of many materials to be utilized for LICs and NICs. According to their comprehension, for example, graphite may not serve as a proper selection as it possesses an excellent plateau in the voltage vs. time curve.

Table 1-3 Recent NIC devices

Electrodes for NICs Anode//Cathode[ref.]	Potential window V	Max energy density (E_{max}) Wh kg^{-1}	Max power density (P_{max}) W kg^{-1}	Capacity Retention/ cycles
		E at P_{max}, Wh kg^{-1}		
$MoSe_2$/graphene// commercial AC[79]	0.5-3	82 30	10752	81%/ 5000
Carbon microsphere//activated carbon microsphere[69]	0-2.5	52 15	3000	85%/ 2000
NiF_2//AC[80]	0-4	50 15	8500	50%/ 1000
CoF_2//AC[80]	0-4	60 15	8500	60%/ 1000
$Na_2Ti_9O_{19}$//AC[77]	1-4.5	54 11	5000	75%/ 2000
Molybdenum phosphide// $Na_3V_2O_2(PO_4)_2F$@ rGO[78]	0.1-4.3	120 50	10000	81%/ 250
ZnO templated carbon// salt-templated carbon[81]	1-4	61 10	11500	90% / 1300
MoS_2-C//Activated carbon[82]	1-3.8	111.4 19.1	12000	77.3%/ 10000
Hard carbon// Fe-V-O nanosheets[70]	0-3.8	200 30	4000	65%/ 800
MoS_2/carbon fibers//AC[83]	1-4.3	60 28	900	-
Polyimide//Polyimide-derived activated carbon[84]	0-4.2	66 13.3	1200	82.4%/ 1000

2. Thesis objectives

To address the performance gap between batteries and supercapacitors mentioned in the introduction, the research carried out for this thesis is focused on the design and development of highly porous and durable cathode materials for hybrid capacitors. Moreover, high-rate anodes that can facilitate the Li/Na ion insertion and enhance the kinetic imbalance between the cathode and anode are also explored. For the capacitive electrode, the focus is on tuning the surface characteristics of the carbon materials to maximize the Li^+/Na^+ charge storage capacity. For the insertion materials, the focus is on the rational design of nanostructured materials to enhance the pseudocapacitive charge storage or electronic and diffusional properties of insertion materials. Additionally, facile material synthesis techniques have been used to fabricate composite materials with nanostructures and large carbon-content to bring the Faradaic charge storage to the surface of the electrodes. Following the composite materials' design and preparation, several physicochemical and electrochemical characterization techniques have been employed to establish a link between electrochemical behavior and the nanostructure at the molecular level.

The research carried out in this thesis is divided in to three main categories.

1. Design and optimization of a crosslinked and ultrahigh surface area carbon derived from polyaniline to serve as both an LIC cathode and an NIC cathode, and then study the cathodes' physicochemical and electrochemical performances.
2. Design pseudocapacitive nanostructured materials to act as the anodes of LICs, and evaluate a full cell device based on the synthesized anode and the material prepared in the first category as the cathode.
3. Utilize the carbon crosslinked structure prepared in the first step as a backbone to deposit transition metal dichalcogenides such as MoS_2 and conduct characterization to examine

the molecular properties of the synthesized anode. Carry out electrochemical testing and study a full cell NIC comprised of the anode synthesized in step 3 and the cathode prepared in step 1.

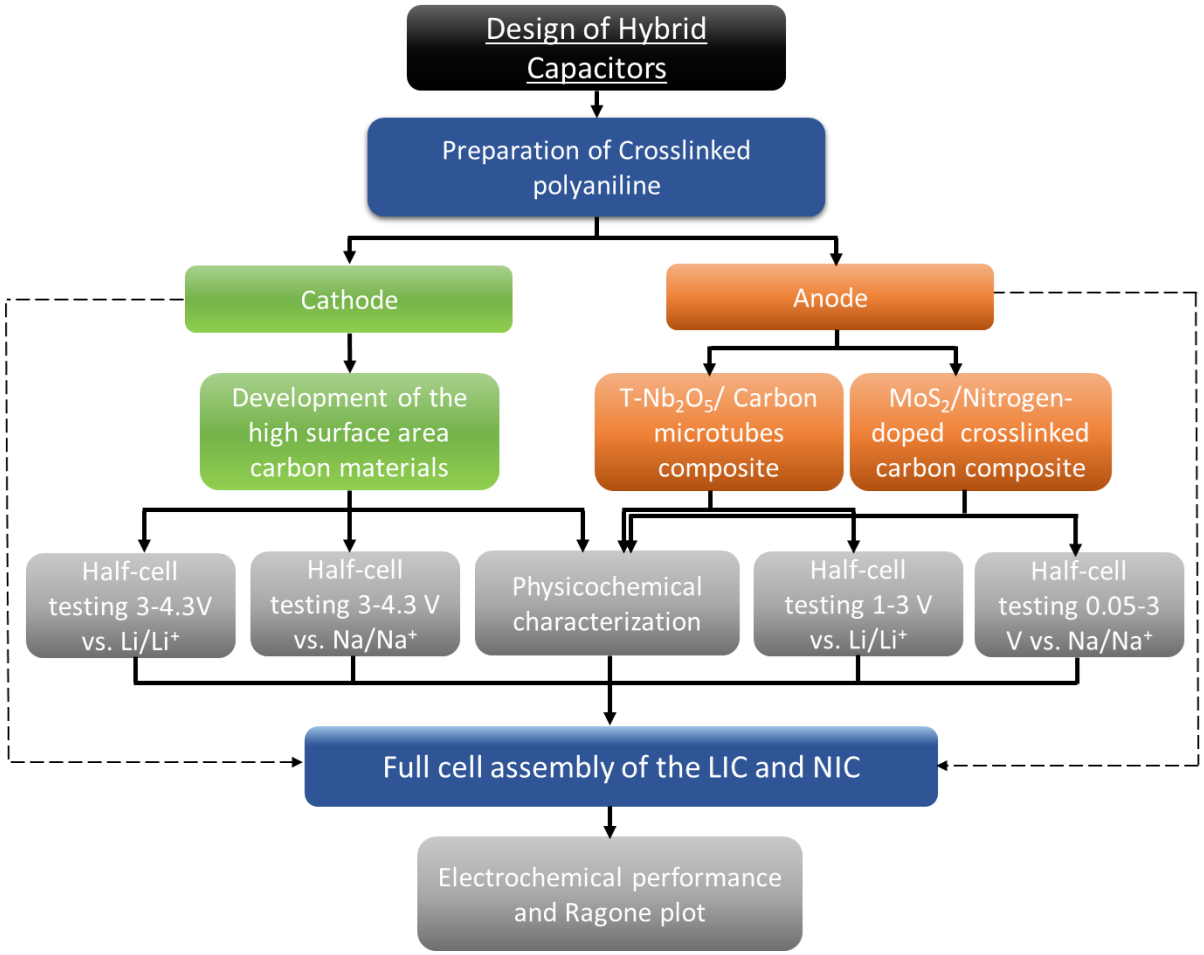

Figure 2-1 Schematic of this thesis work flow

2.1. Thesis outline

Chapter 1 introduces the topic of this thesis and briefly reviews the literature related to organic hybrid Li-ion and Na-ion capacitors. **Chapter 2** outlines the thesis organization. **Chapter 3** covers the physicochemical and electrochemical characterization techniques that are relevant to this project as well as the key metrics that can be evaluated using the characterization

techniques. **Chapter 4** starts with the preparation and optimization of polyaniline-derived carbon material. This material was chosen to serve several roles throughout this thesis owing to its unique characteristic such as nitrogen content, electronic conductivity, and distinctive morphology with abundant macropores for easy electrolyte access and ion diffusion. In this chapter, the carbon material is further activated to serve as the high surface area cathode of hybrid capacitors (LICs and NICs) and to enhance the double layer capacitance. The activation procedure of the carbon materials is optimized such that the best charge storage capacity in half-cell configurations is realized. **Chapter 5** introduces an in-situ formed nitrogen-doped composite of T-Nb_2O_5 and carbon by studying the polymerization of aniline in the presence of the niobium oxide precursor. The in-situ formed Nb_2O_5 nanoparticles embedded in carbon microtubes are used as the LIC anodes. Half-cell electrochemical performances are provided as well as the performance of the full cell device based on the mentioned composite as the anode and the carbon material prepared in Chapter 4 as the cathode. The LIC device made in **Chapter 5** shows promising energy density and power density values, bridging the Li-ion batteries and supercapacitors on the Ragone plot. Despite the promising charge storage capability of the LIC, the world's defined lithium supply made us to consider an alternative to LICs. Therefore, the search for a promising anode material for NICs is the focus of **Chapter 6**, in which we presents the design of a composite containing MoS_2, a promising anode material of sodium-ion batteries, and the carbon framework prepared in Chapter 4. We have presented an NIC device based on this anode and the cathode prepared previously. The chapter shows that the nitrogen moieties in the interconnected carbon have electronic coupling with MoS_2 nanosheets, offering enhanced cycling stability compared to pure MoS_2. Also, deposition on the conductive backbone prevented the agglomeration of the MoS_2

nanosheets. **Chapter 7** concludes this thesis and suggests future work that can be built on its findings.

3. Physicochemical and electrochemical characterizations

3.1. Electron microscopy techniques and energy dispersive x-ray spectroscopy (EDS)

Scanning electron microscopy (SEM) is a powerful and well-established imaging technique used to investigate the morphology of micro and nanostructured materials. SEM uses a forced beam of electrons to illuminate the sample, and project images based on the secondary or backscattered electrons.[85] Data are collected over a selected area of the sample, and a 2-dimensional image is generated. The SEM is also capable of performing analyses of selected point locations on the sample when analyzing chemical compositions using Energy dispersive X-ray Spectrometry (EDX).

EDX which is commonly integrated with the SEM device can obtain compositional information using characteristic x-rays. This technique involves bombardment of electrons onto a materials surface which results in the emission of x-rays collected by a detector. The energy intensities of the emitted x-rays are the characteristics of certain elements, allowing their appropriate identification. Variations in the emitted x-ray intensities is an indication of the variations in the specific atomic contents at specific locations and can be used to map the concentration of different elements (elemental mapping). A typical EDX spectrum is portrayed as a plot of x-ray counts vs. energy (in keV).[86] Preparation of samples for SEM imaging involves spreading the sample onto carbon tape, secured to a sample holder stub. The stub can subsequently be placed into the SEM machine for imaging. During the proposed projects SEM and EDX will be utilized to investigate the distinct nanostructures of the fabricated electrode materials.

Transition electron microscopy (TEM) is an imaging tool which allows high-resolution imaging of samples on the nanometer scale. In this method, a beam of electrons is transmitted through the very small site of interest while interacting with it. A four-stage condenser lens system controls the aperture of illumination, which results in controlling the illumination area of the sample. Electrons are scattered either elastically or inelastically after interaction with the sample which makes thin sample preparation obligatory. The signals from the collected diffracted electrons can be processed to produce an image. With such high resolution, TEM is effective in determining nanostructures, atomic arrangements, exposed crystal facets and defects within the structure.[87]

3.2. X-ray diffraction (XRD)

X-ray diffraction (XRD) is a crystallography characterization technique that can be used to study the crystal structure of a material. The interactions between the monochromatic beam and the sample results in diffraction patterns at the angels that are the that has information about crystal orientations of a specific plane. The XRD is designed such that either the sample or the light source is swept over a range of angles. Then the diffracted beams are detected by a detector. The lattice spacing of a specific crystal can be derived using the Bragg's law.

$$n\lambda = 2d\sin\theta \qquad (3\text{-}1)$$

where n is an integer, λ is the wavelength of the beam, d is the interplanar spacing of the crystal under study. The X-ray source is used as the incident beam, as it has the same order of magnitude as the interplanar spacing of the crystallin materials. If the sample interacts with the incident beam such that the Bragg's law is satisfied, a characteristic peak in detected.

3.3. X-ray photoelectron spectroscopy (XPS)

X-ray photoelectron spectroscopy (XPS) is a quantitative technique that measures the elemental composition and electronic states existing on the surface, within 10 nm of the sample. In this method, the sample is irradiated with x-rays of known energy, resulting in the emission of electrons by the photoelectric effect. The binding energy spectrum of these photoelectrons is recorded by which the identification of the elements present on the surface of the sample is viable.[88] XPS can only analyze materials with their atomic numbers equal to or greater than 3 as the orbitals in hydrogen or helium are too small. XPS requires high vacuum (P ~ 10-8 millibar) and samples to be investigated must be in the solid form.[88,89] In this proposed project, XPS will be utilized to analyze the surface concentrations of various doped heteroatoms and elements including Nitrogen, carbon, oxygen, molybdenum and niobium as well as their types of bonding and electronic states.

3.4. Brunauer-Emmett-Teller (BET) surface analysis

Brunauer-Emmett-Teller (BET) analysis is the first choice to investigate the surface area of porous materials. The technique accurately determines the amount of gas adsorbed on a solid material: a direct measure for the porous properties and structure. Sample preparation involves degassing, in which the combination of vacuum and heat treatment is applied to remove the contaminants from the surface and pores of the sample. Then, the sample is cooled to a cryogenic temperature (77 k) and an adsorptive (nitrogen) is dosed to the sample in controlled relative pressure. After each dose of adsorptive the quantity adsorbed is calculated. The theory works based on a number of assumptions; adsorption occurs only on well-defined sites of the sample, there is no interaction between the adsorption layers, and the layer number tend to go infinity at the saturation pressure. Besides surface area, pore size and pore volume are other key parameters to

be evaluated by gas adsorption technique. Typically, t-plot is used to characterize micropores and BJH method is utilized to distinguish mesopores and small macropores and pore size distribution.[90,91] During this project, these key parameters are source of evidence as they directly influence the interaction between highly porous materials and electrolyte. It is worthwhile to mention that mesoporous facilitate ion diffusion while micropores enhance the double layer capacitance in supercapacitor applications.

3.5. Raman spectroscopy

Raman Spectroscopy is a non-destructive technique, capable of obtaining the information on the structural and electronic state of a system. This technique is a popular characterization tool for carbon-based samples, such as amorphous carbons, graphite, graphene, and nanotubes. Raman Spectroscopy is based on the inelastic scattering of a monochromatic light. Raman Effect is small but detectable and it is based on the molecular deformation in an electric field. A laser beam which can be considered as an electromagnetic wave interacts with the sample, resulting in excitation and deformation of the molecule. This transfers molecules into vibrating dipoles and results in shifting the energy of the laser photons. This shift in energy provides characteristic information of the vibrational mode of the sample.[92] In this project, Raman Spectroscopy will be used to study the degree of the graphitization or the degree of the structural disorder of the carbon-based materials (I_D/I_G).

3.6. Half-cell electrochemical evaluations

The first set of electrochemical studies after materials' design and preparation is half-cell testing where electrochemical properties of the synthesized material is tested with reference to a Li/Na metal chip, using a two-electrode system configuration n CR2032 coin cells (shown in

Figure 3-1). Separators (Celgard or glass fibers) are wetted by 1M LiPF6 in a 1:1 mixture of ethylene carbonate (EC) and diethyl carbonate (DEC)/ 1 M $NaClO_4$ in a 1:1 EC: DEC and separate the anode and cathode electrically. Coin cell assembly is conducted in an argon filled glovebox with low oxygen concentration (<0.5 ppm O2) and low humidity (<0.5 ppm H2O) to prevent unwanted reactions between water/oxygen with metal chips.

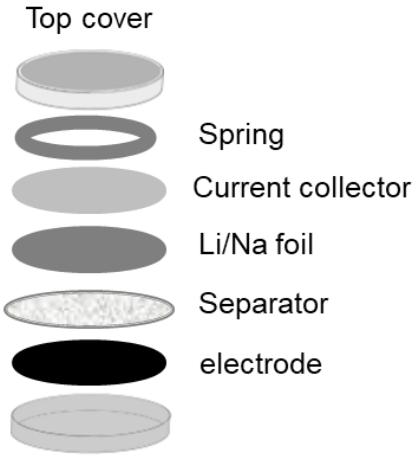

Figure 3-1 Illustration of a CR2032 half-cell device

The cathode half-cell performance is presented in **Chapter 4**, and the half-cell results for the composite materials as LIC and NIC anodes are presented in **Chapter 5** and **Chapter 6**.

3.6.1. Constant current charge discharge (CCCD)

Characterization via the charging–discharging curve at constant current is the most widely used approaches to determine specific capacity, energy density, power density, and equivalent series resistance. Also, using this method, studying the cycling stability is feasible. Although the conventional three-electrode or two-electrode test cells can be employed, the two-electrode cell configuration is advantageous because it more closely resembles practical applications. **Figure 3-2** reveals that the capacitive electrodes exhibit straight lines in their CCCD curve, while the

insertion type electrodes depict a plateau during charge and discharge, which is the characteristic of the phase transition during Li-ion/ Na-ion intercalation/deintercalation.

Specific capacitance can be determined based on the result from CCCD test. Normally, discharge time (Δt) is used for measuring the charge transferred.

$$C_s = \frac{\Delta Q}{\sigma \Delta V} = \frac{I\,\Delta t}{\sigma \Delta V} \tag{3-1}$$

where I is the constant discharge current, and ΔV is the cell potential window. σ is active material mass.

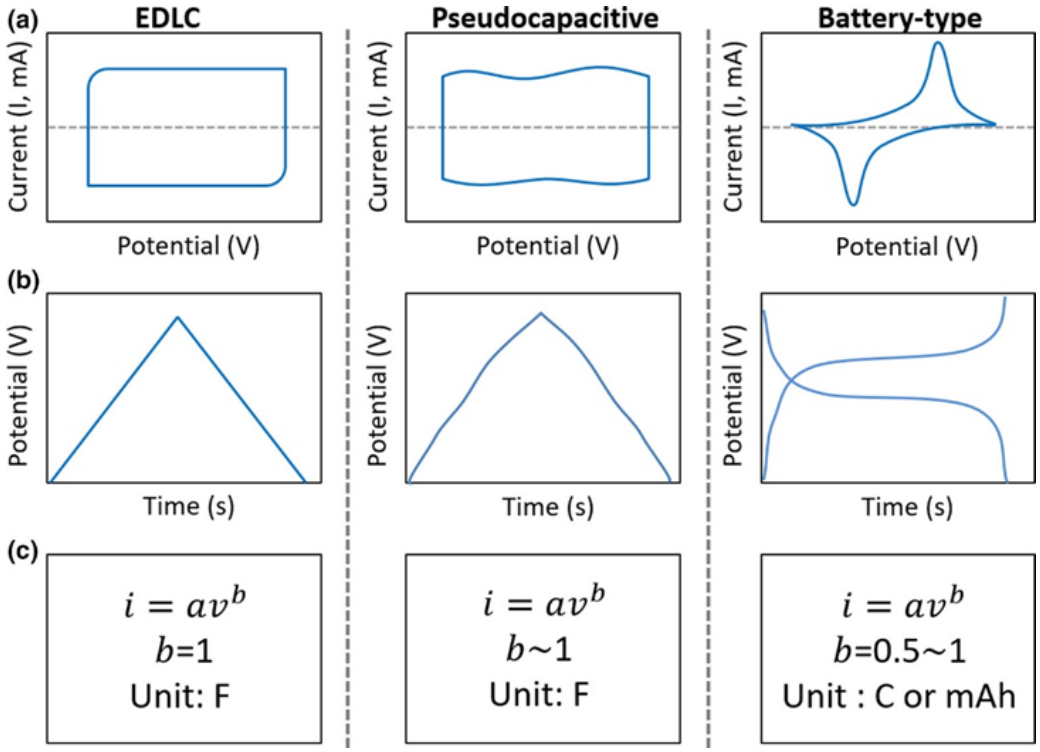

Figure 3-2 Differentiating EDLC, pseudocapacitive, and battery materials' electrochemical signature, with permission from Ref. [23]**.**

3.6.2. Cyclic Voltammetry (CV)

CV testing is a commonly used potential-dynamic electrochemical technique that applies a linearly changed electric potential between the reference and working electrodes for three-electrode configurations. The current change during the cathodic and anodic sweeps is recorded and the data are plotted as current vs. potential or sometimes as current or potential vs. time. For supercapacitors application, the test results can be analyzed by examining the shape of the CV curves. For EDLC and most pseudocapacitor materials, the shape of the resulting CV curves is rectangular or quasi-rectangular, respectively, while for some insertion type materials, reversible redox peaks may occur. In order to differentiate different charge storage mechanisms (capacitive or faradaic) , several CV testing at various scan rates is required to be done. The current induced by the electrical double layer is proportional to the scan rate, while the diffusion limited reaction current is proportional to the square root of the scan rate. **Figure 3-2** illustrates the CV profiles for a capacitive, pseudpocapacitive, and insertion type electrodes.

3.6.3. Electrochemical impedance spectroscopy (EIS)

Electrochemical impedance spectroscopy is a widely used method to measure the equivalent series resistant (ESR) and electrolyte resistance of an electrochemical device. By modeling the device to a circuit containing various elements and experimental curve fitting, reaction mechanisms can be studied. EIS' working principles consist of the application of a sinusoidal AC signal and study of the AC response. During the test, the frequency of the AC input changes, and the impedance of the system is calculated and recorded with magnitude, Z, and phase shift, Φ ($Z(\omega) = Z_0\, exp\, (cos\phi + jsin\phi)$). The Nyquist plot with the real impedance on the real axis and imaginary impedance on the y axis, contains ESR and electrolyte resistance information.

3.6.4. Galvanostatic Intermittent titration technique (GITT)

Analysis of galvanostatic intermittent titration technique is conducted to study the diffusion coefficient of the composite materials in **Chapter 6**. During this method, the coin cells, with a Na foil as the counter and reference electrode and the synthesized materials as the working electrode, were charged/discharged with a constant current density of 10 mA g^{-1} for 10 minutes. The current was then removed for 1 h to relax the system back to the equilibrium. This procedure was repeated to reach the cut-off voltage limitations. Then the chemical diffusion coefficient can be calculated at each step, with the following formula:[93]

$$D = \frac{4}{\pi}\left(\frac{IV_m}{Z_A FS}\right)^2 \left(\frac{dE(\delta)}{d\delta} \Big/ \frac{dE(t)}{d\sqrt{t}}\right)^2 \qquad (3\text{-}2)$$

Where I denotes the constant current applied during pulse time; V_m is the molar volume of the electrode which is calculated according to the rule of mixtures; F is the Faraday's constant; S is the electrode/electrolyte interface area; and Z_A is the charge number. $dE(\delta)/d\delta$ is the change in steady state voltages before and after each titration steps. $dE/d\sqrt{t}$ is the change of the voltages during the charge/discharge time (t).[93]

3.7. Full-cell electrochemical evaluation

Full cells (LICs and NICs) are assembled with the same components as half-cells replacing the Li/Na foil with negative electrode and their full cell performances are provided in **Chapter 5**, and **Chapter 6**. The first set of electrochemical experiment on full cells starts with CV for the realization of safe potential window within which the decomposition of the electrolyte is prevented. CCCD discharge curve is used to calculate energy density and power density by equation 3-3 and 3-4:[94]

$$E = \int_{t_1}^{t_2} I\,V\,dt \quad (W\,h\,kg^{-1}) \tag{3-3}$$

$$P = {}^{E}/_{t} \quad (W\,kg^{-1}) \tag{3-4}$$

where I is the discharge current density based on the total mass of the active materials in both electrodes, V is the working potentials during the discharge process, and t is the discharge time. Energy density values are plotted against power density and are plotted in **Chapter 5** and **6**. It worth to mentioning that although methodologies for electrochemical performance evaluation of supercapacitors are available in the literature,[94–96] there is still inconsistency on how to calculate the key parameters such as energy density or power density. For example, while many studies define their current density as the current applied per mass of the active material in both electrodes, others have defined it as the current per the active material in one electrode only.[66] These discrepancies have resulted in extraordinary electrochemical performance of some hybrid capacitors that outperforms batteries.[66]

4. N-doped interconnected carbon structure from polyaniline as the cathode for hybrid capacitors

4.1. Introduction

As mentioned in previous chapters, LIBs, NIBs, EDLCs, and hybrid devices are among the electrochemical energy storage devices that have received tremendous attention in research and have found their practical applications in EVs and HEVs.[30,34,97] Hybrid devices have emerged to fill in the performance gap between batteries and supercapacitors, providing high energy, power density, and long cycle life.[98] LICs and NICs are among the hybrid devices and have been thoroughly introduced in the first chapter of this thesis. Designing anode materials for these devices has been the primary focus of most research works in this area, disregarding the significance of designing the cathode materials. In these hybrid devices, cathode materials possess capacitive behavior in which charge is stored in a double layer formed in the interface of the electrode and electrolyte.[22] Commercial activated carbon, the most common electrode materials in EDLCs, offers limited energy density to hybrid devices.[36] Therefore, fine-tuning the morphology and surface area of the carbon materials and adding heteroatoms to the carbon structure, are promising approaches to improving the energy density of LICs and NICs' cathodes. As mentioned earlier, heteroatoms can add fast surface reactions or pseudocapacitive mechanism to the capacitive performance of the carbon materials as the cathode of hybrid devices.[99,100]

The study in this chapter highlights the development of nitrogen-doped, highly porous, and cross-linked carbon materials synthesized from polyaniline. More specifically, this study was done to evaluate and optimize the electrochemical and physicochemical properties of polyaniline-derived cross-linked carbon for three main purposes throughout this thesis: (1) as the LIC and NIC

cathodes after chemical activation, (2) as a scaffold to incorporate a metal oxide (Nb_2O_5) for LICs anode, and (3) a framework to deposit a metal dichalcogenide (MoS_2) for NICs anode. This type of carbon material possesses several critical features beneficial to electrode materials: (1) the unique hierarchical morphology owns many macropores, mesopores, and micropores that ensure efficient electrolyte infiltration and high surface area for large double layer separation of charge, (2) doped nitrogen atoms that introduce fast surface reactions to electrodes, and (3) and high electronic conductivity despite having ultrahigh surface area. The study in the present chapter not only offers a promising cathode candidate for hybrid capacitors, but also opens up possibilities for researchers to design composite materials as anodes to circumvent the challenges associated with anode materials' low conductivity and volume variations during ion insertion/extraction.

4.2. Experimental

4.2.1. Preparation of N-doped high surface area carbon

The synthesis procedure of the carbon materials was borrowed from Ref. [50] and was further modified and optimized to maximize the capacitance of LICs' and NICs' cathodes in this thesis. Polyaniline was synthesized using the oxidative polymerization of aniline. Briefly, 570 mg of ammonium persulfate (APS) was mixed with de-ionized distilled water (DDI) in a 20 mL vial (Solution A). In another vial, 460 µL of aniline was mixed with 2 mL DDI following by 1 mL phytic acid to prepare a homogenous solution of the monomer (Solution B). Both solutions were kept at 4°C for several minutes. Solution A was added to solution B, followed by mixing for several seconds and was then rested for one hour while polymerization occurred. The resulting dark green polyaniline, known as emeraldine salt, was immersed in DDI and washed with plenty of DDI. The prepared polymer was freeze-dried or vacuum-dried for two days followed by subsequent annealing in argon at 900 °C for 3 hours. Activation of the resulting materials was carried out by

mixing KOH with carbon in a slurry followed by drying at 60 °C, in a convection oven. The powder was loaded to a tube furnace and the material was activated at different temperatures under argon. The reactions that are involved during the chemical activation of carbon using KOH is explained in chapter 1. The prepared highly porous carbon was washed thoroughly with 2M HCl to remove potassium metals, DDI, and ethanol, followed by drying in a vacuum oven at 60°C. The activation temperature and KOH: carbon mass ratio are two key parameters that are optimized based on the electrochemical characterization of the cell (specific capacity of the half-cell against Li and Na foil). Samples before and after the activation are called NC and NAC, respectively, followed by the temperature and KOH: carbon ratio at which they are activated. **Figure 4-1** illustrates the synthesis procedure and electrode preparation.

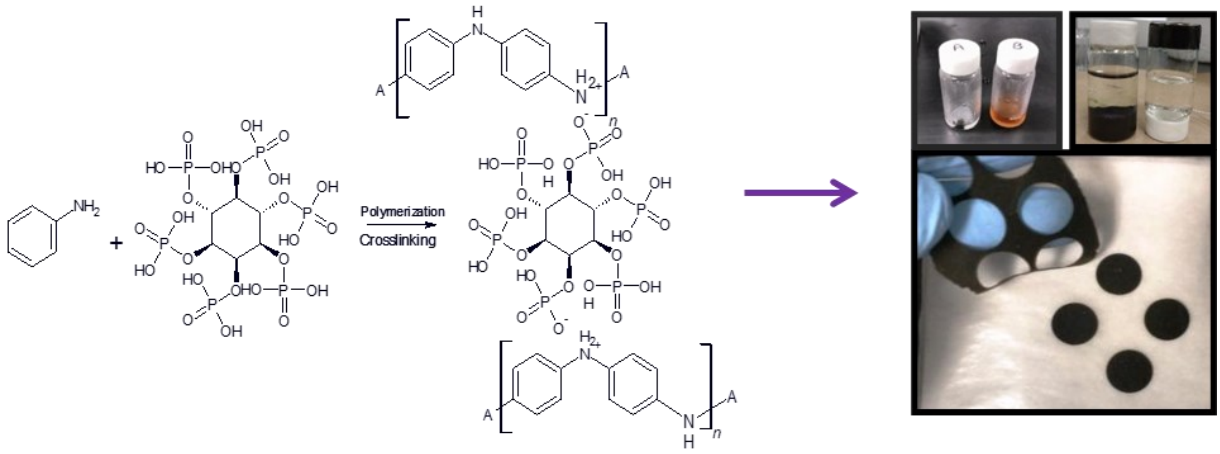

Figure 4-1 Schematic representation for the preparation of polyaniline and free-standing electrodes from NACs

4.2.2. Physicochemical and electrochemical studies

SEM (SEM, LEO FESEM 1530) was used to study the morphological properties of the samples. Raman spectroscopy was performed to determine the graphitization degree of the samples, and BET surface area analysis was done to determine the surface area and pore size

distribution of the synthesized materials in this chapter. For the electrochemical studies, free-standing electrodes are prepared using 90% of the NAC samples and 10% of polytetrafluoroethylene (PTFE). The two were uniformly mixed with ethanol and DDI (1:1 v/v), and the mixture was dried in an oven for 12 hours. Next, the dried sample was mixed with a few drops of ethanol to prepare a paste. Using a roller press, electrodes were pressed, followed by punching into circular disks. The punched electrodes are dried at 80 °C in a vacuum oven. The free-standing electrodes were transferred to the argon-filled glove box for the coin cell assembly (CR2032 coin cells were used). Li metal foil, 1 M $LiPF_6$ dissolved in a 1:1 v/v mixture of ethylene carbonate/diethyl carbonate (EC/DEC), a Whatman glass fiber, and the synthesized electrodes were used as the counter electrode, the electrolyte, separator and the working electrode, respectively. CV tests were carried out at voltage ranges of 3.0−4.3 V vs. Li/Li^+. CCCD tests were performed at different current densities within 3.0−4.3 V vs. Li/Li^+.

To test the synthesized material as cathode of NICs, the CR2032 coin cells were assembled in the glove box with sodium foil as the reference and the counter electrodes, and NACs as the working electrode. The electrodes were separated by a Whatman glass fiber wetted by the 1.0 M $NaClO_4$ in 1:1 (v/v) mixture EC/DEC as the electrolyte. Electrochemical tests were done at voltage range of 3-4.4 V vs. Na/Na^+.

4.3. Results and discussion

High surface area nitrogen-doped carbon materials were derived from cross-linked polyaniline by annealing and activation. Table 4-1 summarizes the charge storage performance of NAC samples as a LIC and NIC cathode during discharge. The activation temperature was varied between 700-900 °C, and the sample treated at 800 °C presented the highest capacity in

electrochemical LIC and NIC's half-cell tests. The ratio of KOH: NC was also changed between 3 to 5, and the NAC-800-3 showed a superior Li^+ and Na^+ charge storage capacity. **Figure 4-2** presents the nitrogen adsorption/desorption isotherms for the NC-800 and NC-800-3. NC-800 shows type II (according to IUPAC classification of nitrogen adsorption isotherms of materials) with BET specific surface area of 30 m^2 g^{-1}, indicating the macroporous (pore size> 50 nm) nature of NC-800. This suggests that this low surface area scaffold can also serve as a substrate for the deposition of intercalation-type materials to boost the electronic conductivity as well as diffusional properties on the anode side.

After activation with KOH, the isotherm transfers to type I, showing that NAC-800-3 is highly microporous with the specific surface area of 2425 m^2 g^{-1}. (relative pressure interval used for BET analysis was 0.02- 0.1).

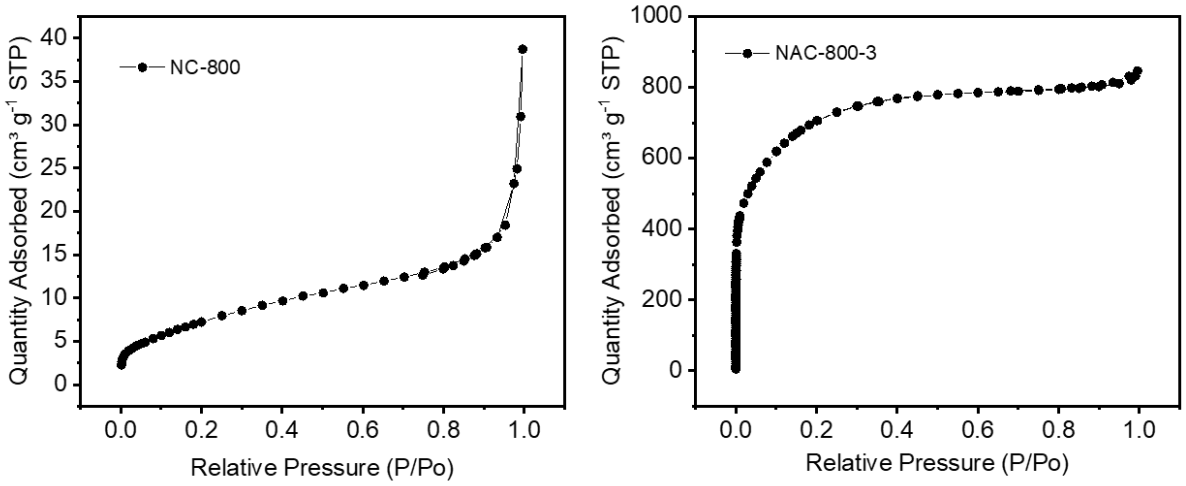

Figure 4-2 N_2 adsorption/desorption isotherms of NC-800 and NAC-800.

Using BET analysis, the surface area and the pore size distribution report for all the NAC samples are also summarized in Table 4-1. The total pore volume is defined as the volume of liquid nitrogen adsorbed at a relative pressure of 0.995. The micropores' volumes are calculated from t-

plot, and the microporosity content is calculated by dividing the result from t-plot by the total pore volume. With increasing activation temperature, an optimum in BET surface area and pore volume is seen. These results suggest that increasing the activation temperature to 800 °C creates a larger number of micropores with a higher extent of microporosity, leading to larger specific surface area. Further increase in the temperature, however, results in the formation of larger pores (mesopores, 2-50 nm). Thus, the extent of mesoporosity increases as a result of more carbon erosion, showing smaller specific surface area.[101]

Table 4-1 Electrochemical half-cell performances of NAC samples and their surface area analysis

Half-cell performance of NACs @ 0.1 A g^{-1}	Effect of the activation temperature, KOH: NC, 3:1				Effect of KOH: NC, at 800 °C	
Sample's name	NAC-700-3	NAC-750-3	NAC-800-3	NAC-900-3	NAC-800-4	NAC-800-5
Capacitance vs. Na/Na^+ ($F\ g^{-1}$)	81.8	80	132	73	98	77.4
Capacitance vs. Li/Li^+ ($F\ g^{-1}$)	118	123.2	145.9	95.81	110.4	90.8
BET Surface area ($m^2\ g^{-1}$)	1927	2017	2425	1800	2311	971
Total pore volume ($cm^3\ g^{-1}$)	1.13	1.01	1.309	1.20	1.05	0.530
Mesopores and macropores (%)/Micropores (%) distribution	24%/ 76%	17%/ 83%	18%/ 82%	66%/ 34%	20%/ 80%	32%/ 68%

On the other hand, increasing the KOH: NC ratio resulted in an excessive reaction of KOH with carbon and carbon structure collapse. Therefore, drops in total pore volume, microporosity, and

surface area were observed.[102] NAC-800-3 possessed the highest surface area and capacitance, thus was further used for physicochemical characterizations.

Figure 4-3 (a) and shows representative SEM images of NC-800 and **Figure 4-3 (b)** and is the SEM images of NAC-800-3. NAC-800 demonstrates a macroscopic interconnected network of carbon after annealing, emerged from the continuous framework of polyaniline. SEM images for NAC-800-3 relatively reveal shrinkage of the structure as a result of the activation procedure. On the other hand, it clearly demonstrates that KOH activation has introduced channels in the interconnected structure which favors the facilitated electrode wetting and mass transfer of ions.

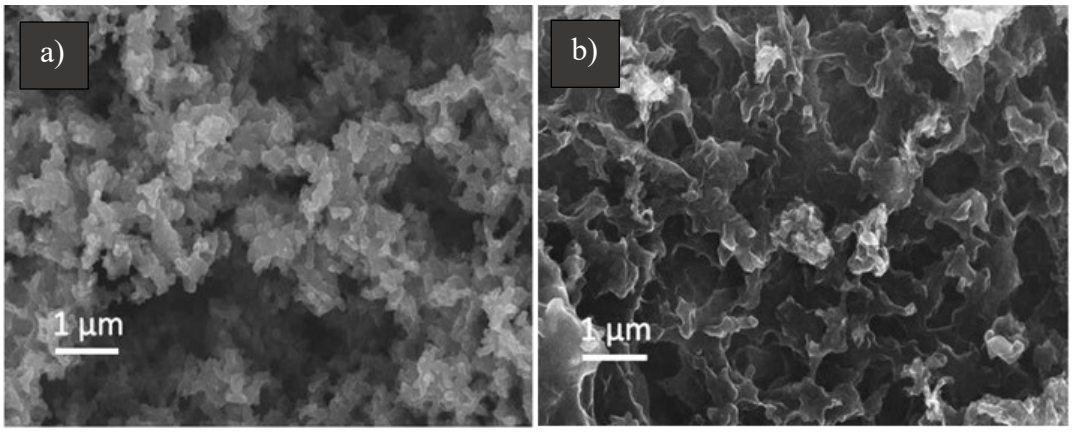

Figure 4-3 SEM images of (a) NC-800 and (b) NAC-800-3.

Figure 4-4 (a) illustrates the Raman spectra for the NC-800 and after its activation. The Raman spectra for NAC-800-3 confirms the presence of sp^2 hybridization or graphitic sheets (G-band at 1580 cm^{-1}), as well as D-band at 1333 cm^{-1} attributed to the presence of the defects, suggesting a partially graphitized structure. Generally, the relative intensity ratio of D-band and G-band (I_D/I_G) represents the degree of the graphitization of the material.[92] As shown in the figure, activation of the carbon materials resulted in producing more defects and distortion to the structure, increasing I_D/I_G from 1.03 to 1.09. It has been shown that higher carbonization temperature offers

higher graphitization degree and there is a trade-off between the degree of graphitization and the specific surface area of the carbon materials.[103] On the other hand, a higher surface area carbon structure results in an enhanced double layer capacitance at the cathode of NICs, while a higher graphitization degree favors electrode conductivity.

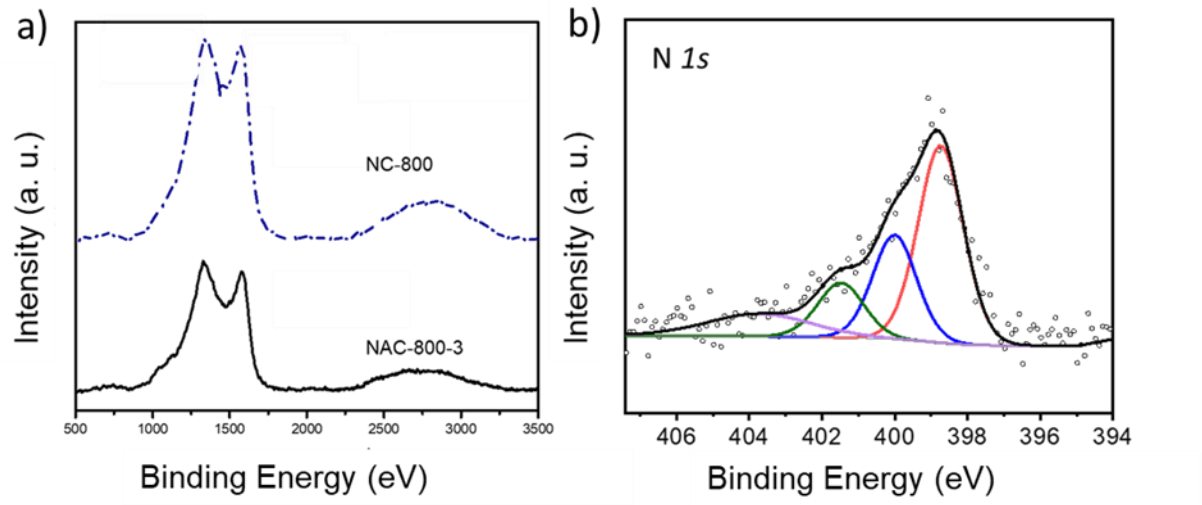

Figure 4-4 (a) Raman spectra of NC-800 and NAC-800-3 with their relative ratio of I_D to I_G, (b) XPS N 1s spectrum of NAC-800-3

For these reasons, electronic conductivity of NAC samples was measured using a home-made two-probe conductivity mold and the linear polarization resistance (LPR) technique. The electronic conductivity of NAC-700-3, NAC-750-3, NAC-800-3, and NAC-900-3 samples were, 106 S m^{-1}, 119 S m^{-1}, 104 S m^{-1}, and 86 S m^{-1}, respectively. The variation of electronic conductivities with increasing the activation temperature, denotes an initial increase in the electronic conductivity. This together with the increase in the surface area, indicates the generation of more pores without sacrificing the electronic conductivity of the sample. Further increase in the temperature presents a continuous drop in electronic conductivity due to further erosion of carbon and the creation of larger pores, as confirmed by pore size distribution.

XPS analysis was performed to study the nitrogen doping content and types of nitrogen moieties in the NAC-800-3 sample. The N 1s spectrum of NAC-800-3 is shown in **Figure 4-4 (b)** and was deconvoluted to four different nitrogen moieties with corresponding atomic percentages: Pyridinic (398.77 eV, 44.2%), pyrrolic/pyridine (399.98 eV, 30.57%), quaternary (401.4 eV, 10.96%),[104] and N-oxide species (403.6 eV, 14.2 %) resulted from carbon activation. Nitrogen atoms can introduce fast surface redox reaction and enhance the capacitance. Also, possessing the electron donor characteristics, this heteroatom is beneficial for designing robust composite materials, suppressing the active material dissolution or structural changes during electrochemical testing. These claims will be discussed in details in the following chapters of this thesis.

LICs' half-cell test of NAC-800-3 is provided in **Figure 4-5**. CV results shows the regular rectangular shape with no faradaic peaks at low scan rate, which is the characteristic of the capacitive electrodes. A linear dependence between the anodic/cathodic current densities and the applied scan rates is shown in **Figure 4-5 (b)**, suggesting that the charge storage mechanism is based on fast surface adsorption/desorption process; the formation of electric double layer at the electrode/electrolyte interface during charging/discharging process is based on the adsorption/desorption of PF_6^- anions on the surface of the NAC-800-3 electrode. The CCCD results shown in Figure 4-5 (c) reveal the effect of the drying method during the synthesis on the capacitance and more importantly, the rate performance of NAC-800-3. The freeze-dried sample maintains 87% on the initial capacity, whereas vacuum-dried sample only provide 63% of its initial capacitance at 2 A g^{-1}. This signifies the role of open pores for fast adsorption/ desorption of ions. KOH activation significantly enhances the rate performance of these materials (**Figure 4-5 (c)**). Discharge specific capacitance (capacity) at current density of 0.2 A g^{-1} for NAC-800-3 are 144 F g^{-1} (52 mA h g^{-1}) and 58 F g^{-1} (20.9 mA h g^{-1}), respectively. NAC-800-3 shows a good rate

performance maintaining 87% of initial capacitance at 2 A g^{-1}. Rate performance of NAC-800-3 can be compared to the commercial activated carbon (HDLC-20BST-UW, coconut shell derived supplied by Haycarb) which maintains 80% of the initial capacity at the 2 A g^{-1}. Moreover, the specific discharge capacitance obtained from the synthesized material is higher than that of commercial activated carbon (100 F g^{-1}) and other activated carbon materials reported in the literature.[15,63,64]

NICs' half-cell test of NAC-800-3 is provided in **Figure 4-6.** To obtain an optimal working voltage, the CV tests were performed on three coin cells with different voltage windows as shown in **Figure 4-6 (a)**. All coin cells had the NAC-800-3 as their working electrode. The cell cycled at the largest voltage window shows the onset of two broad peak on the anodic and cathodic scans at around 3.7 and 3.4 V vs. Na/Na^+, respectively. This may indicate the decomposition of the electrolyte or the reaction of the activated carbon's functional groups with the electrolyte. Following the CV test, the long cycling tests were performed (presented in **Figure 4-6 (e))** to choose an optimal voltage window based on the capacity fading after 1000 cycles. The voltage window of 3-4.4 V vs. Na/Na^+ was chosen for more electrochemical tests. The scan rates were varied between 2-5 mV s^{-1} with no apparent redox peak indicating that the N-doped activated carbon provides storage of charges by capacitive and pseudocapacitive mechanisms (**Figure 4-6 (b)**). The CCCD results provided in **Figure 4-6 (c)** and **(d)** show fast linear profile and provide 130 F g^{-1} at the current density of 0.05 A g^{-1}. These values are much larger than the commercial activated carbon (from *Calgon*) tested in our lab (35 F g^{-1}) and those reported in the literature.[68,105] These results emphasize the nitrogen-doped activated carbon as a high capacitance with promising rate performance, attributed to the morphological features and high electronic conductivity, can be a viable cathode material for hybrid capacitors.

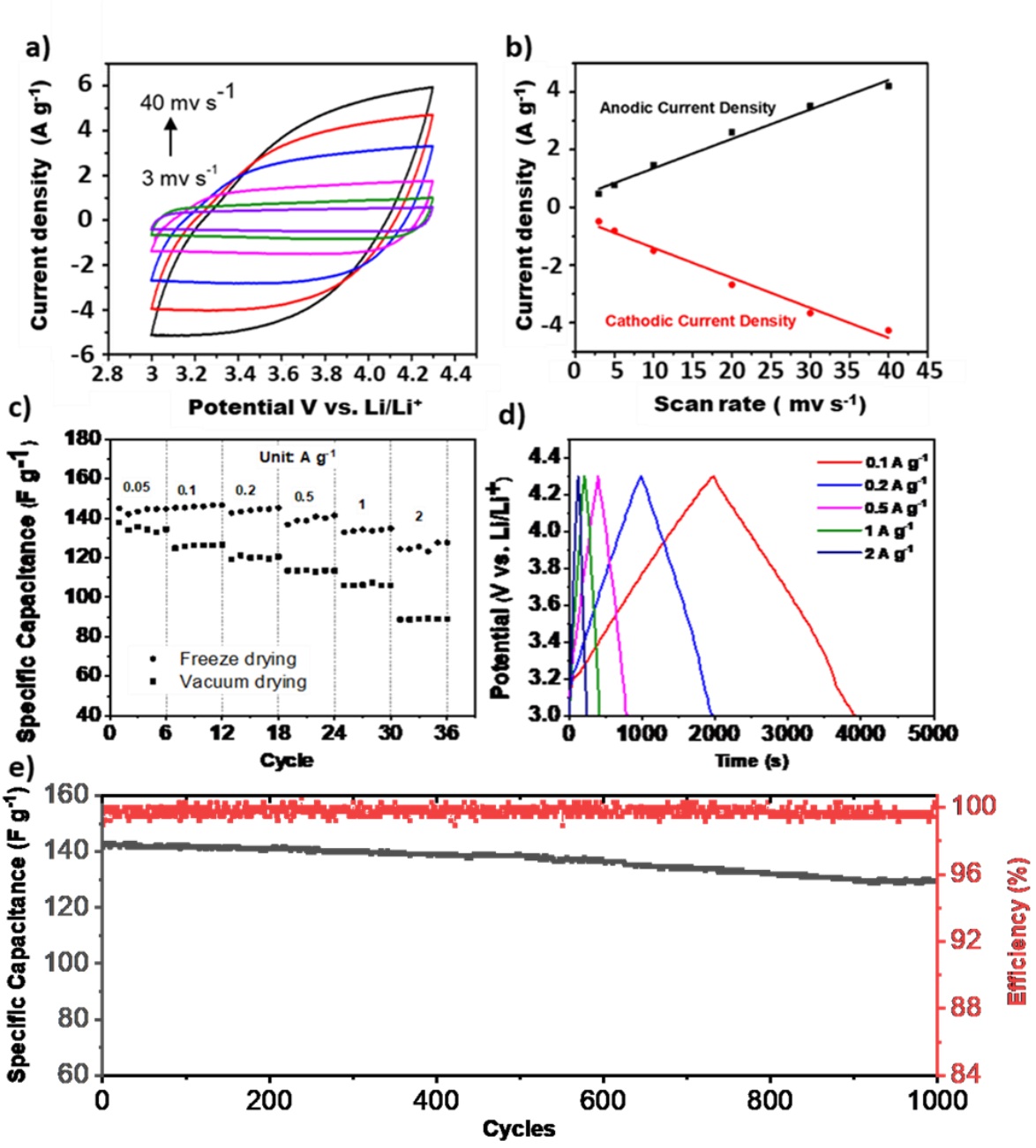

Figure 4-5 LIC half-cell performance of NAC-800-3 (a) CV at different scan rates, (b) plot of anodic and cathodic current density at 3.6 V vs. Li/Li^+ versus scan rates, (c) galvanostatic charge/discharge revealing the effect of freeze drying compared to vacuum drying (d) voltage-time curves and e) cycle stability and coulombic efficiency within 3-4.3 V vs. Li/Li^+, at 0.2 A g^{-1}.

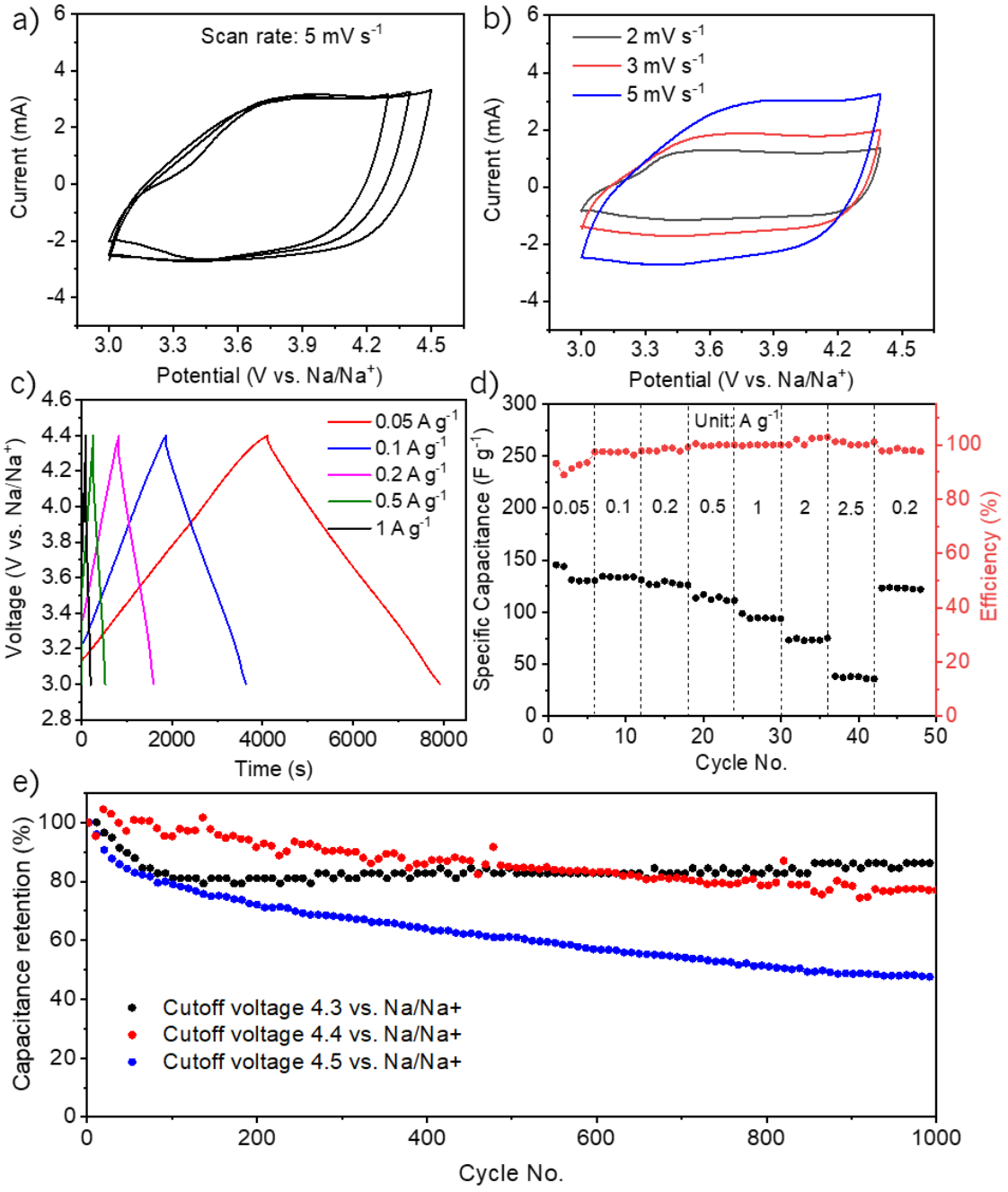

Figure 4-6 NIC half-cell performance of NAC-800-3 (a) voltage limits optimization, (b) CV curves at various scan rates, (c) Galvanostatic charge/discharge with different current densities, (d) rate capability at different current densities with the voltage window of 3-4.4 V vs Na/Na^+, (e) Long cycling performance at 0.5 A g^{-1} with different cutoff voltages.

4.4. Summary

An ultrahigh surface area carbon framework was developed and characterized by SEM, BET, XPS, CV, and CCCD techniques. The preliminary results show an improved capacity performance comparing to the records in the literature. The synthesized material meets the criteria for the cathode of LICs and NICs as it can provide relatively high capacitance and cycle stability and fast charge/discharge characteristics. Moreover, the carbon framework tunable morphology suggests that polymer-derived carbon's pore structure and degree of graphitization could be further optimized by templating and pyrolysis procedures to be employed as a scaffold for the preparation of carbon-based hybrid materials.

5. 3D N-doped Hybrid Architectures Assembled from 0D T-Nb_2O_5 Embedded in Carbon Microtubes Toward High-rate Li-ion capacitors

This chapter is reprinted in adapted form from the below article[106] with permission from Elsevier.

Hemmati, S.; Li, G.; Wang, X.; Ding, Y.; Pei, Y.; Yu, A.; Chen, Z. "3D N-Doped Hybrid Architectures Assembled from 0D T-Nb2O5 Embedded in Carbon Microtubes toward High-Rate Li-Ion Capacitors" *Nano Energy* **2019**, *56*, 118–126.

5.1. Introduction

Among energy storage systems, Li-ion capacitors (LICs) have progressively received attention because they achieve a good balance between high-energy density and high-power density systems by combining a Li-ion battery (LIB) anode with Li-ions intercalation capability and an electric double-layer capacitor (EDLC) cathode with fast surface processes.[5] Commonly used electrode materials for LICs are graphite and activated carbon as anode and cathode, respectively, and a device based on this design has been commercialized by JM Energy.[107] Nevertheless, sluggish Li-ion intercalation/deintercalation into graphite and lower operating potential of graphite (~0.3 V vs. Li^+/Li) than that of organic electrolyte reduction (around 1 V vs. Li^+/Li) results in a significant irreversible capacity decay and a poor cycle performance.[8] As a result of these limitations, designing novel anode materials for LICs is a matter of ongoing research and several comprehensive review papers on electrodes materials and their selection criteria for LICs have been published, recently.[5,53,108,109]

Among various reported LIC anodes materials, orthorhombic niobium oxide (*T*-Nb_2O_5) has received a considerable attention due to several intriguing properties, including high-rate lithium-ion transport through (001) plane with minimal energy barriers,[110] low but safe potential window, minimal volume change (3%) upon cycling,[111] and multiple redox couples (Nb^{5+}/Nb^{4+}, Nb^{4+}/Nb^{3+}). [55,112] Nevertheless, poor electron conductivity of Nb_2O_5 (3×10^{-6} S cm^{-1}) and sluggish Li-ions diffusion dynamics in bulk are two of the major obstacles that are required to be surmounted. Accordingly, three main rational approaches have been developed: 1) nanostructuring and designing enlarged surface-to-volume ratio materials, 2) incorporation of a highly conductive components, and 3) modification of the electronic structure of the metal oxide by doping heteroatoms such as nitrogen. First approach ensures accessible active sites to electrolytes, second provides sufficient inter-grain electronic pathways, and the latter noticeably meliorates the electronic conductivity by narrowing the Nb_2O_5 bandgap. [113–115] For instance, Wang et al. [116] reported that a polydopamine-derived carbon-coated *T*-Nb_2O_5 nanowires with reduced charge transfer resistance and enhanced electronic conductivity delivers an excellent rate capability and cycle lifespan. Lai et al,[117] in another study, prepared uniformly grown *T*-Nb_2O_5 nanoparticles on reduced graphene oxide which were further deposited on a carbide-derived carbon scaffold. Such a scaffold not only remarkably contributes to an effective electronic conduction, but also inhibits aggregation of active nanocomponents, enabling the realization of full potential of the active material upon lithiation/delithiation. Despite the encouraging progress, there remains the necessity to design a facile methodology encompassing all the abovementioned approaches through which no initial preparation of the metal oxide is required while incorporation of conductive materials, heteroatom doping, and the metal oxide preparation can be simultaneously carried out.

Herein, a novel and effective approach for a hollow-structured nitrogen-doped composite of niobium oxide and carbon is designed and demonstrated. This facile preparation route involving the rational selection of the niobium oxide precursor (ammonium niobate oxalate hydrate, aNbO) and the carbon source (aniline) leads to an in-situ oxidative polymerization of aniline with a unique and intriguing supramolecular structure owing to the chelation effect, electrostatic interaction, and hydrogen bonding between aNbO and aniline. Hydrothermal and heat treatments further simultaneously result in carbonization of polyaniline and reduction of aNbO to *T*-Nb_2O_5. This unique nanoarchitecture provides several favorable features for sufficient and fast Li-ion storage: (i) hollow interior and porous nanostructure facilitates electrolyte infiltration, and nanoscale active particles shorten Li-ion diffusion distance; (ii) orthorhombic niobium oxide (*T*-Nb_2O_5) nanoparticles evenly distributed, wired, and ingrained in the hollow-structure carbon component deliver enhanced electronic conductivity with high-rate lithium-ion transport through the (001) plane during lithiation and delithiation; and (iii) the presence of polyaniline ensures a high N-doping level (N: ~ 5.3 atomic%) that can contribute to an elevated electron conductivity in addition to charge storage. Owing to the distinctive structural advantages, the resulting nanocomposite, shows reversible capacitance of 370 F g^{-1} at 0.1 A g^{-1} and retains 81% of its initial capacitance after over 1100 cycles at a current density of 0.5 A g^{-1} in a half-cell configuration. Besides, an assembled LIC device based on the as-synthesized materials delivers a remarkable energy density (86.6 kW h kg^{-1}) and high-power density (6.09 kW kg^{-1}) and a promising cycle lifespan.

5.2. Experimental

5.2.1. Material synthesis

5.2.1.1. Synthesis of NbOC-N (anode)

The material preparation procedure is schematically illustrated in **Figure 5-1**. A unique synthetic approach was chosen to prepare the N-NbOC nanocomposite using an in-situ polymerization of aniline in the presence of an acidic and a water-soluble niobium oxide precursor, aNbO, followed by hydrothermal treatment and annealing. The synthesis of N-NbOC was performed through dissolving 1.3 g of aNbO (1.32 mmol based on Nb) in deionized water. Then 458 µl of aniline was added and stirred for several minutes (pH 1). Next, 0.572 mg of ammonium persulfate dissolved in deionized water is added to the solution to start the polymerization of aniline. The polymerization continued for 4 hours at ~ 0 ℃ and the resulting dark green composite of emeraldine base polyaniline (Pani) encapsulating the niobium precursor was then filtered. The hydrothermal treatment was performed by re-dispersing the composite in de-ionized water and transferring it in a 30 ml Teflon liner followed by heating at 180 ℃ for 10 h, during which the nucleation of niobium oxide nanoparticles along with the hydrothermal carbonization of polyaniline initiated. Finally, the resulting composite was dried and transferred to a tubular furnace for heat treatment at 5 ℃ min^{-1} to 700 ℃, where it was held for 3 h under argon to complete the niobium oxide crystallization and carbonization of the Pani. The resulting material is a nitrogen-doped carbon microtubes with uniformly dispersed deposited niobium oxide nanoparticles (N-NbOC).

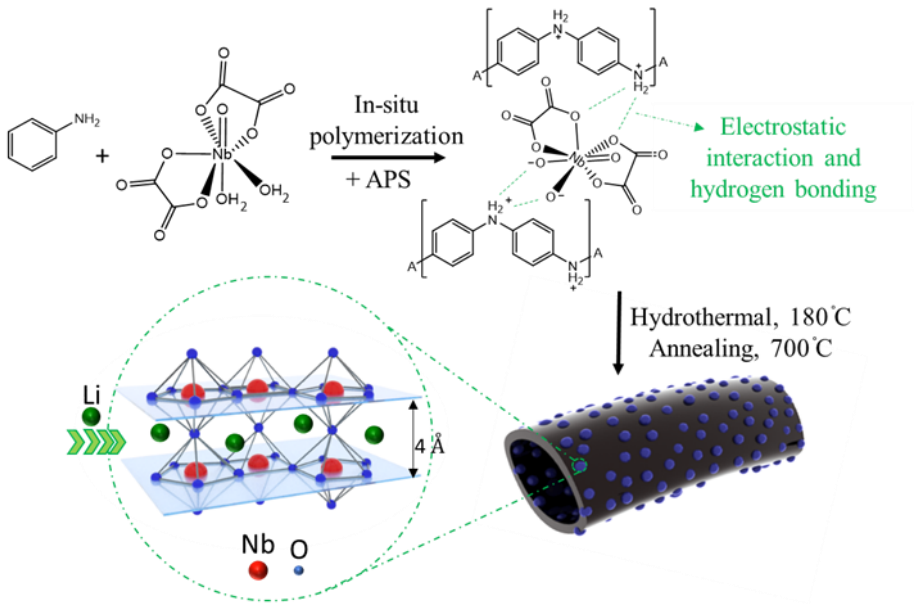

Figure 5-1 Schematic diagrams showing materials preparation steps for the pseudocapacitive intercalation electrode as anode (N-NbOC). Reproduced in adapted form from ref. 104 with permission from Elsevier.

5.2.1.2. Synthesis of the control groups

Synthesis of the comparison materials was performed to study the electrochemical performance of each component and a possible synergistic effect due to nitrogen doping and/or carbon coating. To synthesize niobium oxide nanoparticles (Nb_2O_5) and carbon from Pani (CP), an approach identical to the one that used for N-NbOC was employed, however, in the absence of aniline for the former and in the absence of aNbO for the latter.

5.2.1.3. Synthesis of the cathode

The NAC-800-3 sample which was prepared during the first project introduced in chapter 4 has been employed as the cathode of LIC for this chapter. This sample is called AC in chapter 5 and chapter 6.

5.2.2. Electrochemical characterizations

For half-cell studies a slurry of the active material was prepared with poly (vinylidene fluoride) (PVDF) as a binder and SuperP as a conductive agent (Active material: SuperP: PVDF=85:5:10 by weight). The slurry is then deposited on nickel foam current collectors and dried at 80 ℃ for 12 h in a vacuum oven. Finally, electrodes were pressed and transferred to Ar-filled glove box for coin-cell assembly. The CR2032-type coin cells were fabricated by sandwiching polypropylene separator, soaked in 1.0 M $LiPF_6$ in EC: DEC (1:1), between the Li foil as the counter electrode, and the working electrode (N-NbOC or AC). Half-cell studies for anode was performed within 1-3 V vs. Li/Li^+ and for cathode within 3-4.3 V vs. $Li\backslash Li^+$ voltage window. Specific capacitance values in the half-cell ($C_{N\text{-}NbOC}$) was calculated considering the measured capacitance based on the total mass of the electrode when the capacitance contribution of the carbon (C_{CP}) is neglected. To fabricate the hybrid device, electrodes were prepared by coating the slurry of active material (80%), SuperP (10%), and PVDF (10%) on copper and aluminium foil for anode and cathode, respectively. The electrodes were then pressed and dried at 80 ℃ for 12 h in a vacuum oven followed by coin cell fabrication with the identical separator and electrolyte as half-cell devices. CV and EIS were performed using Gamry Potentiostat (Gamry Instruments, interface 1000). The EIS were measured in the frequency range of 100 kHz to 0.01 Hz with an amplitude of 10 mV at an open-circuit potential (OCV). During CV studies, the hybrid device was cycled in the voltage range of 0.05 to 3 V with several scan rates. The galvanostatic charge-discharge cycling was conducted using a Land CT2001A battery tester.

5.3. Results and discussion

For preparation of anode material, in-situ polymerization of aniline in the presence of aNbO, as both a niobium oxide precursor and acid dopant, was performed. Then, N-doped *T*-

Nb_2O_5/N-doped carbon microtubes (N-NbOC) were obtained by hydrothermal and subsequent heat treatment. The as-synthesized N-NbOC morphological features and phases were first physically characterized (**Figure 5-2**). All XRD diffraction peaks of the as-prepared N-NbOC can be well assigned to orthorhombic crystal structure (PDF No. 030-0873).[110,118] Chen et al. have recently proposed a mechanism for li-ion migration path in *T*-Nb_2O_5. Using in operando Raman spectroscopy and computational approaches, they claimed that the planar distance (4 Å) between the highly dense layer of atomic arrangements provide spacious room for Li-ion intercalation, thus depicting a fast charge kinetics,[119] as shown in **Figure 5-1**. The morphology of the composites was characterized by SEM, TEM, and HRTEM. A tubular structure was identified for N-NbOC composite (**Figure 5-2 (b)**). The intermolecular interaction of N-H and O atoms (hydrogen bonds) and electrostatic interactions between protonated aniline and ionic species of $[NbO(C_2O_4)_2(H_2O)_2]^-$ is expected to direct the in-situ polymerization of aniline and in-situ encapsulation of Nb_2O_5 nano-active components in the N-NbOC, resulting in the formation of the unique tubular hybrid structure.

To investigate the role of the intermolecular interactions during the polymerization, the control groups, including carbon derived from polyaniline (CP) and Nb_2O_5, were separately synthesized and their corresponding SEM images (**Figure 5-3**) indicate a featureless morphology for CP, and nanosphere/nanoparticle structure for Nb_2O_5, thus validating the proposed role of the intermolecular interactions during synthesis of N-NbOC composite. **Figure 5-2 (c)** shows the SEM image of the hollow structure and corresponding elemental mapping using energy dispersive X-ray analysis (EDX), depicting a uniform distribution of the *T*-Nb_2O_5 nanoparticles and nitrogen species. **Figure 5-2 (c)** also reveals the encapsulation of niobium oxide into the microtubular structure.

It is worthwhile to note that the positively charged nitrogen atoms on the polymer chain not only can electrostatically attract the anionic precursor, but also may act as catalytic nucleation sites for the formation of niobium oxide nanoparticles via enhancing the surface energy and surface reactivity,[120] resulting in a uniform distribution of niobium oxide nanoparticles. Scanning transmission electron microscopy (STEM) together with the elemental line-scan (**Figure 5-2 (d)** and **Figure 5-2 (e)**) further confirm the hollow structure of the N-NbOC. This intriguing structure design allows for a sufficient electrolyte accessibility to the active sites by providing high specific surface area, while uniform distribution of the carbon materials secures adequate electronic pathways.[121] The HRTEM image shown in **Figure 5-2 (f)** reveals nanoparticles with sizes of approximately 11 nm, which enables efficient charge and ion transport, thus maximizing the use of the active material. Besides, the orthorhombic structure of *T*-Nb_2O_5 is confirmed as the lattice parameter 0.31 nm and 0.39 nm can be attributed to the (180) and (001) plane of *T*-Nb_2O_5, respectively. Additionally, the HRTEM image shows the presence of a thin layer of carbon coating (~2 nm). The clear lattice fringes (white arrows) indicate the formation of graphitic carbon with a sp^2-type carbon atomic arrangement. So far, only a few metal elements have been reported to be able to catalyze the graphitization of carbon including Ni, Fe, and Co. [122–124] A thorough search in the relevant literature reveals that this is the first report on niobium or niobium-containing compounds with the catalytic effect on the conversion of amorphous to graphitic carbon. This layer of the graphitized carbon coating is highly desirable due to offering enhanced electronic conductivity as well as buffering behavior of the electrode structure during lithiation/delithiation.

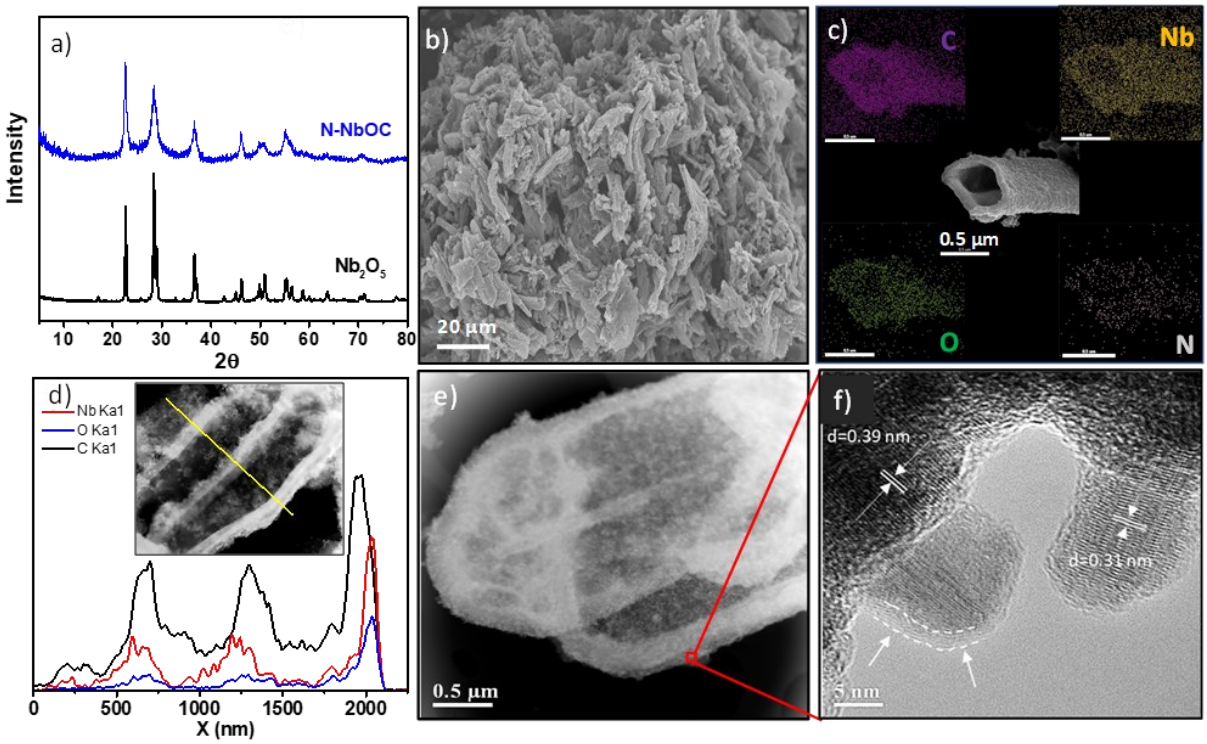

Figure 5-2 (a) XRD patterns of N-NbOC and Nb_2O_5, (b, c) SEM images with different resolution and corresponding elemental mapping (d-e) HAAD-STEM image and corresponding EELS line-scan profiles, and (f) HRTEM of N-NbOC. Reproduced in adapted form from Ref. 104 with permission from Elsevier.

Raman spectroscopy was performed to further examine the structural features of the N-NbOC compared to CP and Nb_2O_5 structures. As shown in **Figure 5-4 (a)**, for N-NbOC and Nb_2O_5 samples, signals at 500-800 cm^{-1} can be attributed to Nb-O-Nb symmetric stretching modes of NbO_6, and signals around 200 cm^{-1} can be assigned to Nb-O-Nb angular deformation.[113,125] The Raman signal with peak at 990 cm^{-1} for N-NbOC sample may be attributed to the terminal Nb=O symmetric.[113,126] The Nb-O-Nb bridging bond of distorted NbO_6 denotes a Raman red shift (626 cm^{-1}) compared to the one for Nb_2O_5 (688.5 cm^{-1}), seen also in previous studies,[127] which may be

explained by differences in niobium oxide nanoparticle sizes, as well as increased disordered structure due to the carbon and nitrogen incorporation. The CP and N-NbOC nanocomposite show distinctive D and G Raman bands at ~1332 and ~1573 cm^{-1}, respectively (**Figure 5-4 (b)**) N-NbOC nanocomposite demonstrates an elevated degree of graphitization (I_D/I_G=0.938) compared to CP (I_D/I_G=1.07), thus delineating a possible catalytic behavior of niobium-containing materials as confirmed by HRTEM.

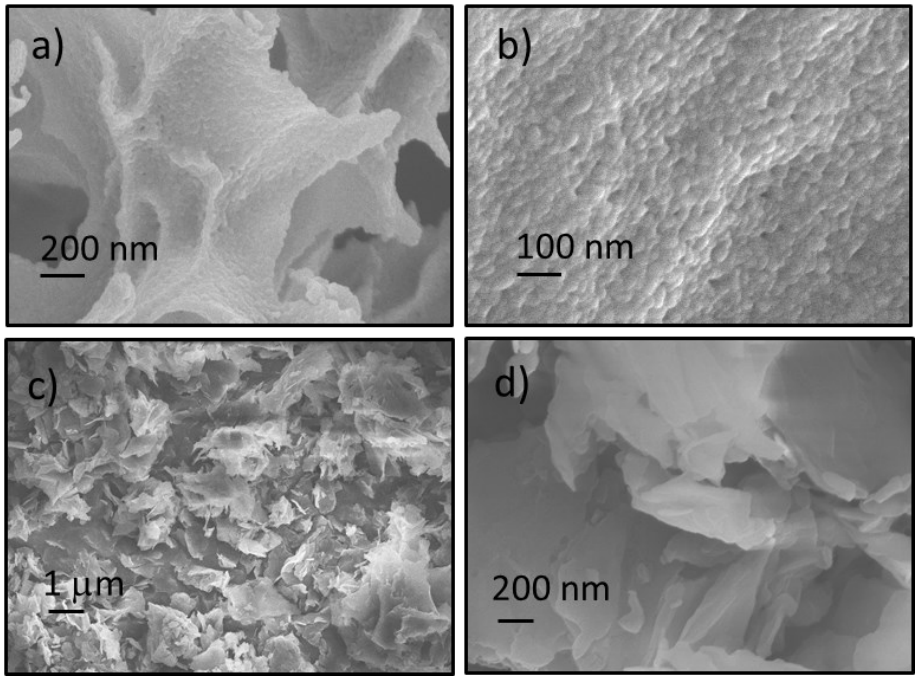

Figure 5-3 SEM images of control groups, (a,b) Nb_2O_5, and (c,d) CP. Reproduced in adapted form from ref. 104 with permission from Elsevier.

To further identify the chemical states of elements in N-NbOC, XPS was carried out. The XPS full spectrum and the characteristic spectra of Nb3d, O1s, and N1s of the N-NbOC are shown in **Figure 5-4 (c-f)**. Peaks from a strong Nb spin-orbit splitting located at 207.1 eV (Nb $3d_{5/2}$) and 209.9 eV (Nb $3d_{3/2}$) and the deconvoluted O1s peak at 530.3 eV verifies the formation of Niobium oxide. [128,129] By comparing XPS spectra of Nb 3d for Nb_2O_5 (207.3 and 210.0 eV) which is shown

in **Figure 5-5**, and that of N-NbOC, a shift in binding energy is observed, which is attributed to the increase of the electron density caused by N substituting for O around the Nb atom. The deconvolution of the O1s spectrum into peaks at 531.3 eV, 532.7 eV, and 534.4 eV indicates the presence of C=O, C-O-C, and carboxylic groups, respectively. The N 1s XPS spectrum of N-NbOC is shown in **Figure 5-4 (f, top)** and it is deconvoluted to four different nitrogen moieties: Pyridinic (398.4 eV), pyrrolic/pyridine (399.6 eV), quaternary (400.8 eV),[104] and N-oxide species (402.9 eV) [130,131] that exist on the surface of Nb_2O_5. To further investigate whether niobium oxide in the N-NbOC sample is doped with nitrogen, N-NbOC was calcined in air at 450 ℃ for 3h to remove carbon and the N 1s spectrum is presented in **Figure 5-4 (f, Bottom)**. The N 1s spectrum after calcination is deconvoluted into 395.2 eV, attributed to substitutional N,[132] and 399.4 eV, assigned to O-Nb-N linkage,[129] corroborating that nitrogen is doped into the metal oxide lattice. The presence of nitrogen-containing functions has been shown to contribute to the total capacitance of electrode by providing fast surface faradaic reaction and enhancing the conductivity of the electrode due to improvement in the electron donor properties of the nanocomposite.

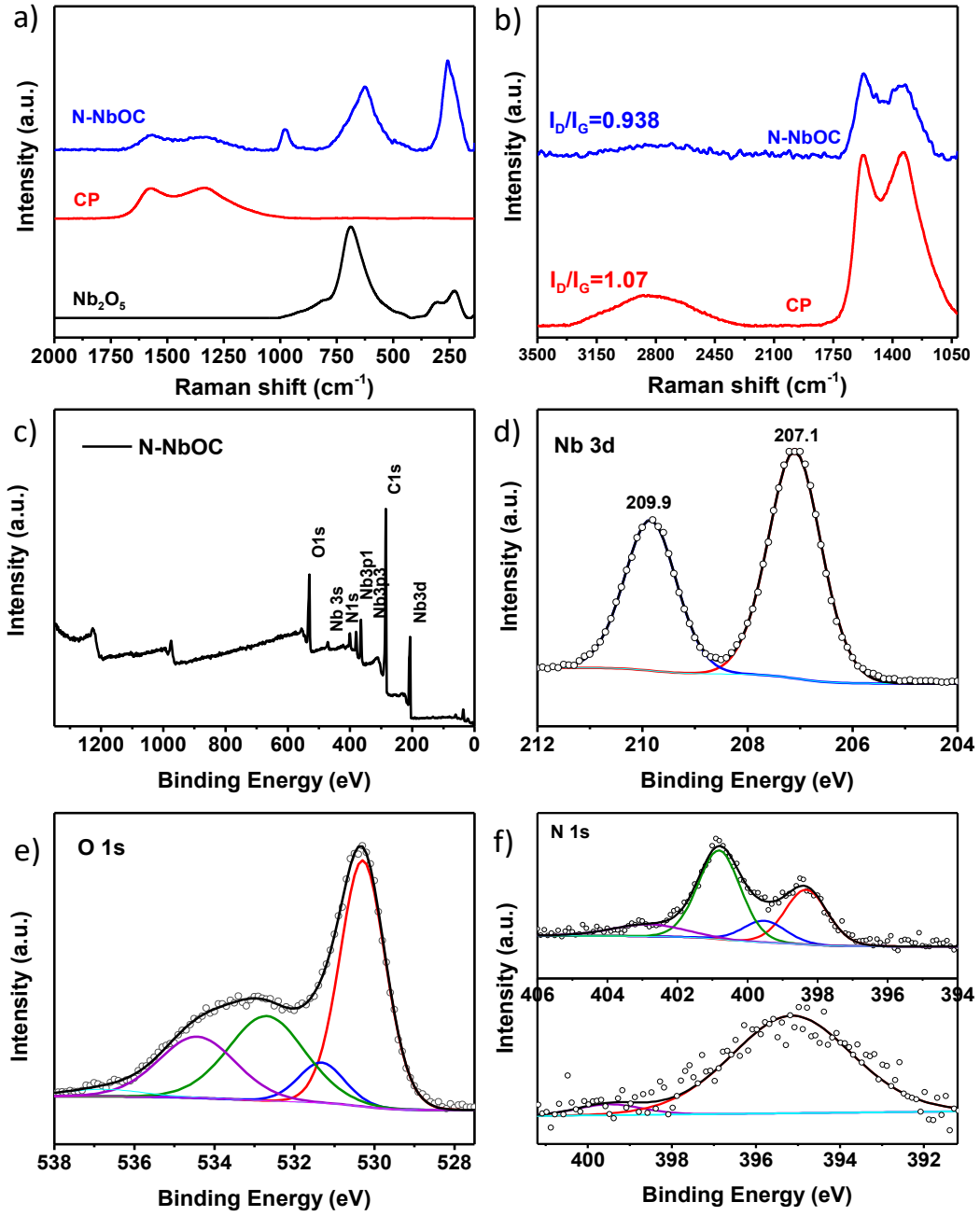

Figure 5-4 (a) Raman Spectra of N-NbOC, Nb_2O_5, and CP, (b) Raman Spectra of N-NbOC, and CP in a narrower region (c) XPS survey, (d) Nb 3d, (e) O 1s, and (f) N 1s of N-NbOC (top) after calcination (bottom). Reproduced in adapted form from ref. 104 with permission from Elsevier.

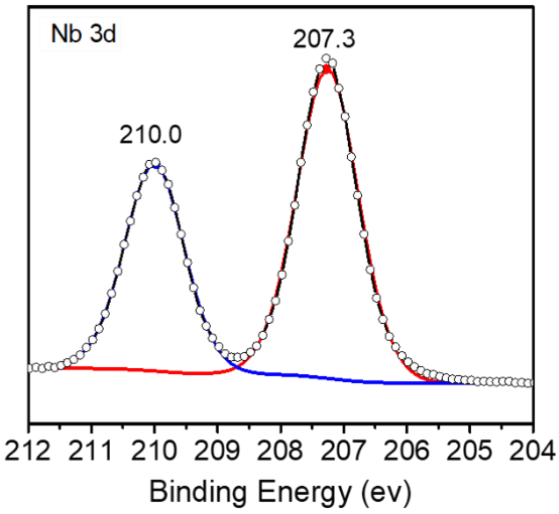

Figure 5-5 XPS spectra of Nb 3d for Nb_2O_5. Reproduced in adapted form from ref. 104 with permission from Elsevier.

Thermogravimetric analysis (TGA), shown in **Figure 5-6**, indicates the composition of the nanocomposite (43.5 wt. % Nb_2O_5). The specific surface areas measured by N_2 sorption isotherms Brunauer-Emmett-Teller (BET) surface areas measured by N_2 sorption isotherms of N-NbOC, Nb_2O_5, and CP are 193.1 m^2g^{-1}, 12.2 m^2g^{-1}, and 30 m^2g^{-1}, respectively. Therefore, the N-NbOC offers expanded electrode/electrolyte interfacial area and thus shortened ion diffusion pathways.

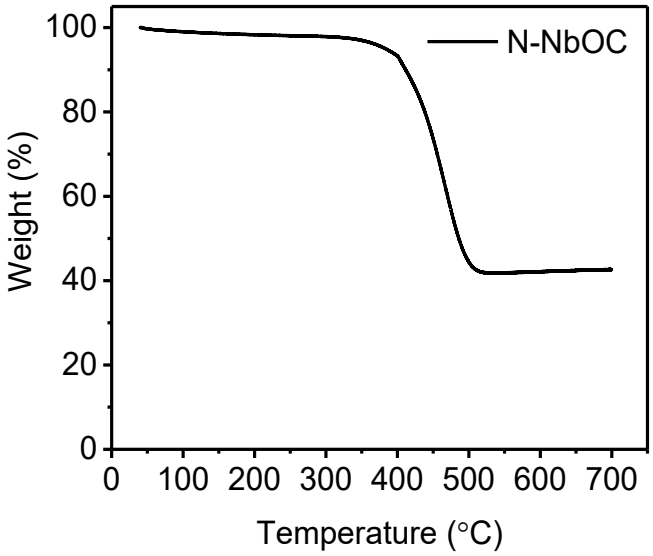

Figure 5-6 Thermogravimetric analysis of N-NbOC. Reproduced in adapted form from ref. 104 with permission from Elsevier.

The insertion/extraction behavior of Li^+ in N-NbOC were first investigated in half-cell configurations with lithium metal chip as both counter and reference electrode. The Cyclic voltammetry (CV) of the N-NbOC of first five cycles are shown in **Figure 5-7**. The first cathodic and anodic scans show one cathodic peak at ~1.79 V and one anodic peak at ~1.61 V, being in accordance with the previous CV profile reported for *T*-Nb_2O_5.[55,128] In addition, second and subsequent cycles show reversible peaks, indicating a high reversibility of Li-ion storage properties.

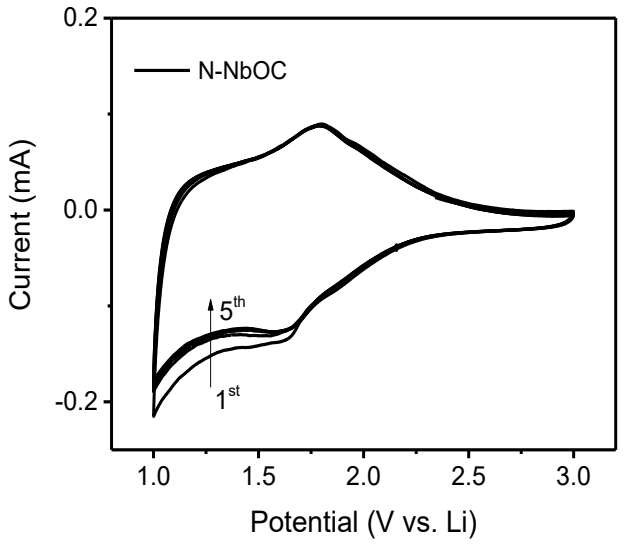

Figure 5-7 CV profile of the first five cycles of N-NbOC at 1 mV s^{-1}. Reproduced in adapted form from ref. 104 with permission from Elsevier.

To study the capacitive and diffusion-limited mechanisms' contribution to the total capacitance, CV curves with different sweep rates are provided in **Figure 5-8 (a)**. The current (*i*, A) and potential scan rate (*v*, mV s^{-1}) relation can be expressed by the power law: [67,110]

$$i = a\vartheta^b \qquad (5\text{-}1)$$

where a and b values are adjustable parameters, and b varies from 0.5, characteristic of the diffusion-controlled process, to 1, attributed to surface processes**. Figure 5-8 (b)** is a plot of log(*i*) versus log(*v*) within 0.1-50 mV s^{-1} scan rates for cathodic peak in which the slop determines *b* in Equation 5-1. From 0.1 to 10 mV s^{-1} sweep rates, the slop is 0.92, manifesting fast surface redox kinetics; in other words, capacitive and pseudocapacitive charge storage contribution surpass diffusion-controlled or slow-kinetic performance. The *b*-value reported in this paper, within 0.1-10 mV s^{-1}, is closer to 1 compared to previous studies on niobium oxide or its nanocomposites within the same or narrower scan rate range,[55,133] suggesting the as-prepared nanocomposite can

be intriguingly beneficial for hybrid capacitors applications. For sweep rates between 15-50 mV s^{-1}, the slope decreases to 0.56, showing that the charge storage is mainly diffusion-controlled.

To quantitatively analyze the charge storage mechanism, the current response (*i,* mA) at a specific potential (V) can be written as the combination of the two abovementioned charge storage mechanisms: [134]

$$i(V) = k_1\vartheta + k_2\vartheta^{1/2} \quad (5\text{-}2)$$

where v is the scan rate. Constant values (k_1 and k_2) can be calculated by plotting $i/v^{1/2}$ vs. $v^{1/2}$ followed by linear regression at a given potential. Based on these calculations, the CV profile for the capacitive currents is plotted in Figure 5-8 (c, shaded area) compared to the total current acquired at 5 mV s^{-1}, depicting a 90% capacitive contribution to the total charge storage. The broad redox peaks in the shaded area further validate that N-NbOC possesses a pseudocapacitive electrochemical performance. Specific capacitance of N-NbOC, Nb_2O_5, and CP at varied current densities is shown in **Figure 5-8 (d)**. The Li^+ insertion and extraction process for the niobium oxide can be expressed by $Nb_2O_5 + x\ Li^+ + x\ e^- \rightarrow Li_xNb_2O_5$, where x is the mole fraction of the inserted Li-ions ($0 < x < 2$) with a maximum theoretical capacitance of ~360 F g^{-1} within 1-3 V vs. Li/Li^+ when x is 2 [110,111]. As illustrated in **Figure 5-8 (d),** the as-prepared Nb_2O_5 reaches its theoretical capacitance for the first cycle, dropping to 37.6 F g^{-1} at 2 A g^{-1}. However, N-NbOC provides 471.1 F g^{-1} during the first cycle and can provide 126.9 F g^{-1} at 2 A g^{-1}, thus depicting remarkably higher capacitance and rate capability than pure Nb_2O_5 owing to the enhanced electronic conductivity and unique nano architecture. As expected, CP does not noticeably contribute to the total capacitance, providing only 28.8 F g^{-1}, due to its low surface area and low Li-ion intercalation potential in carbon materials (<1 V vs Li/Li^+) that is well below the voltage

window employed in this work. The outstanding electrochemical performance of N-NbOC can be attributed to a synergistic effect arising from: (i) nitrogen doping into the crystal lattice that not only contributes to the improved conductivity but also can provide fast surface faradaic reactions, (ii) the micrometer size of the tubes which significantly facilitates electrolyte access to the electroactive sites of N-NbOC, and nanometer size of homogeneously embedded niobium oxide nanoparticles within carbon mictrotubes that shortens the lithium transport path throughout the whole particle, and (iii) immediate contact between the carbon layer and metal oxide that efficiently provide electronic pathways.

To elucidate the difference between the conductivity of N-NbOC and Nb_2O_5 electrode, electrochemical impedance spectroscopy (EIS) was carried out and the Nyquist plots are shown in **Figure 5-8 (e)**. The equivalent series resistance (R_{ESR}) of N-NbOC and Nb_2O_5 electrodes after two cycles are 1.9 Ω and 4.6 Ω, respectively. Moreover, N-NbOC shows smaller charge transfer resistance (R_{CT}), 116 Ω, than that of Nb_2O_5, 237 Ω. Although R_{CT}s for both samples decrease after 100 cycles, a significant difference between the two remains. The decrease in resistance after 100 cycles can be explained by the improved electrolyte wetting, and as a result increased ionic conductivity upon cycling. [135] The EIS results indicate that conductivity of N-NbOC is superior due to carbon coating and nitrogen doping, manifesting the previously discussed results.

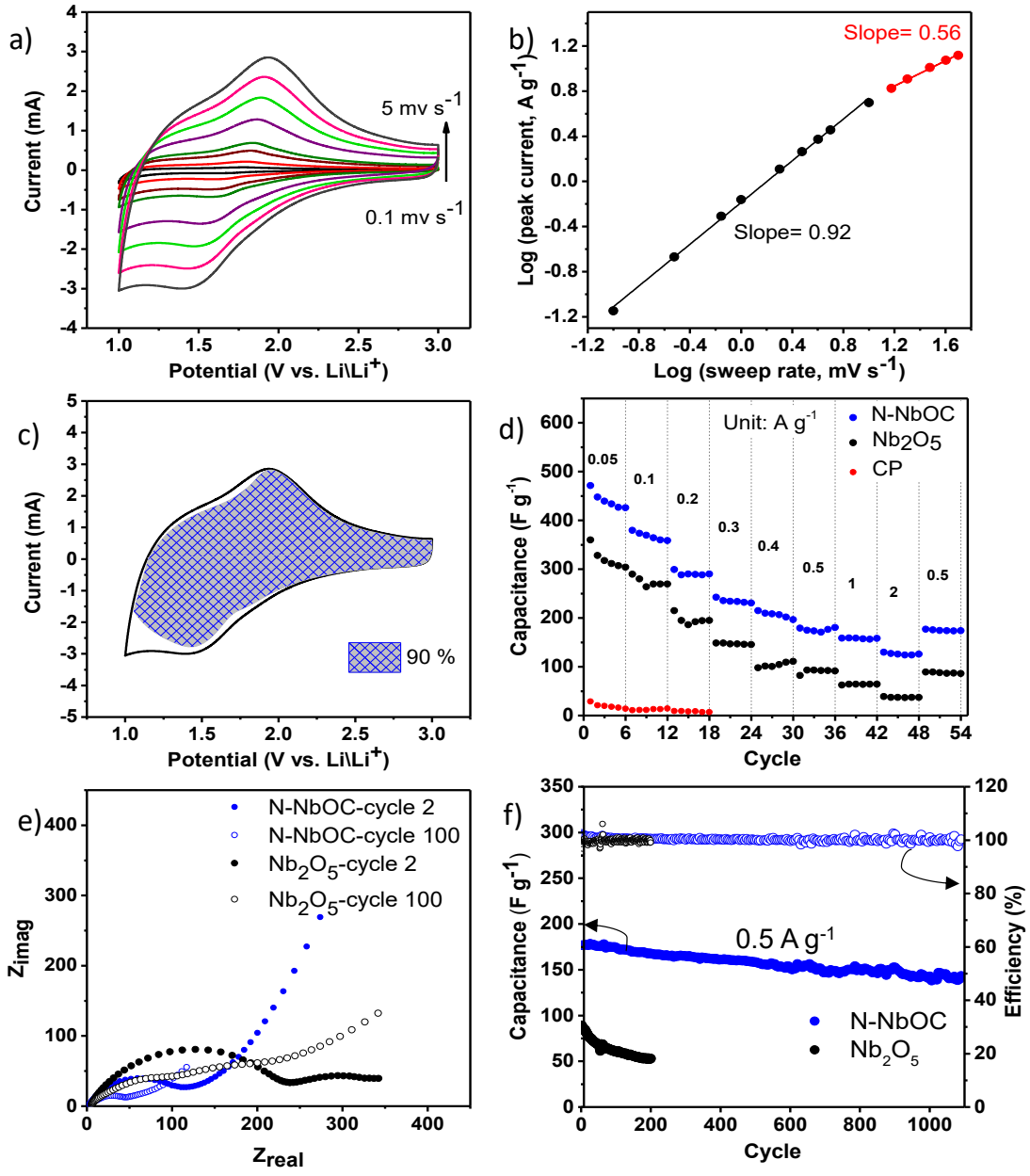

Figure 5-8 Electrochemical performance of N-NbOC electrode (a) CV with various scan rates, (b) linear dependence of the peak currents vs. various scan rates (0.1 mV s^{-1}-50 mV s^{-1}), (c) capacitance contribution (blue) to the total current at 5 mV s^{-1}, (d) rate capability of N-NbOC, Nb_2O_5, and CP (e) EIS of N-NbOC and Nb_2O_5 after 2nd and 100th cycles. (f) cycling performance of N-NbOC and Nb_2O_5 and their respective coulombic efficiencies. Reproduced in adapted form from ref. 104 with permission from Elsevier.

Cyclability at 0.5 A g^{-1} is shown in **Figure 5-8 (f)**. In a half-cell configuration, Nb_2O_5 drops to 52.9 F g^{-1} only after 200 cycles, maintaining 67% of its initial capacitance. N-NbOC, however, maintains 81% of its capacitance after 1100 cycles, exhibiting an excellent cycle stability owing to the higher conductivity and unique morphological features as discussed earlier. This cycling stability is superior than that of other niobium oxide or niobium oxide-containing composites in a half-cell configuration, reported elsewhere.[55,116,133]

A full cell device was fabricated to study the application of the as prepared N-NbOC in LICs, using N-NbOC as anode and the activated carbon (AC) as cathode. The LIC device with optimized electrodes mass ratio ($m_{cathode}$: m_{anode}, 1.2:1) was tested within 0.05 and 3.0 V and the results are presented in **Figure 5-9**. The optimization of electrodes masses is provided in a Ragone plot in **Figure 5-10**. It is worth to mention that during the electrode preparation effort is devoted to keep the cathode mass loading constant (~1 mg) while the mass loading of the anode is varied. CV curves of the N-NbOC//AC with different scan rates resembles a nearly ideal CV profile of supercapacitors (**Figure 5-9 (a)**), offering capacitive and pseudocapacitive intercalation mechanisms. The charge/discharge profiles, presented in **Figure 5-9 (b)**, reveals a quasi-symmetric triangular profile, validating the capacitive/pseudocapacitive processes. More importantly, the LIC device exhibits a promising stability with ~81% capacitance retention after 3500 cycles at 3 A g^{-1} and 0.4 A g^{-1} with approximately 100% coulombic efficiency during cycling (**Figure 5-9 (c)**) which outperforms several cycling performances previously reported. [55,116] To further explore the energy and power characteristic of N-NbOC//AC and to provide comparison with other LIC devices, a Ragone plot is provided in **Figure 5-9 (d)**. The assembled LIC device provides a maximum energy density of 86.6 W h kg^{-1} at the power density of 112 W kg^{-1}. At faster discharging time (48 s) a remarkable performance is observed with energy and power densities of

58.7 W h kg $^{-1}$ and 3.84 kW kg^{-1}, respectively. As can be seen in **Figure 5-9 (d)**, N-NbOC//AC exhibits a superior electrochemical performance compared to 3D-CNWs/T-Nb_2O_5//CAN [136], N-doped urchin-like Nb_2O_5, [115] Nb_2O_5/Graphene//AC,[127] Nb_2O_5/CMK-3//PSC,[137] and Nb_2O_5-rGO-CDC//AC, [117] owing to its distinctive structural features.

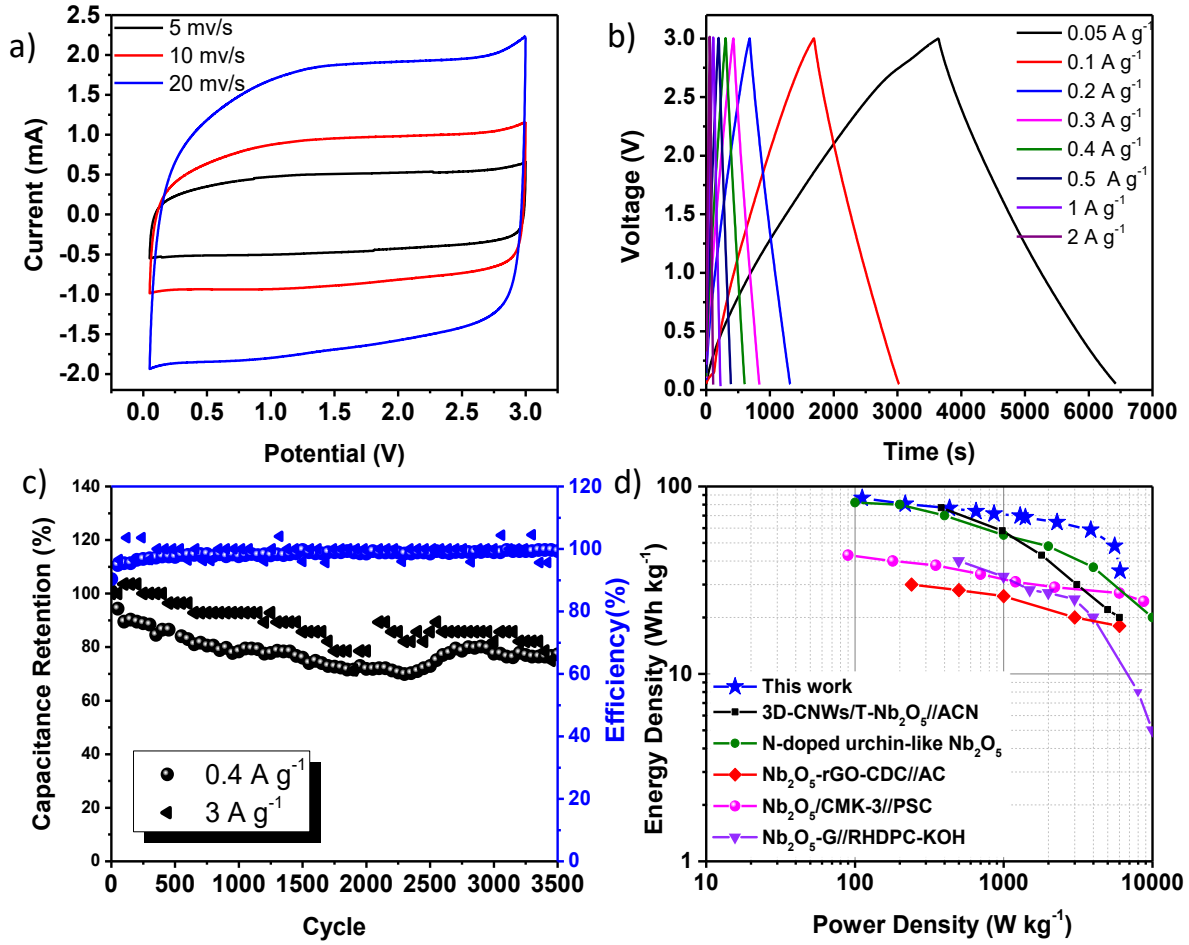

Figure 5-9 Electrochemical performance of N-NbOC//AC (a) CV with various scan rates, (b) Galvanostatic Charge\ Discharge at 0.05- 2 A g^{-1}, (c) Long cycling performance at 0.4 and 3 A g^{-1} within 0.05-3 V vs. Li/Li$^+$, (d) Ragone plot of N-NbOC//AC and other LIC devices. Reproduced in adapted form from ref. 104 with permission from Elsevier.

The corresponding EIS profile of the LIC prepared in this work (**Figure 5-10 (b)**) depicts a small R_{CT}. Besides R_w indicates a high electronic conductivity explaining the high rate capability of the LIC. To the above merits, the low loading of metal oxide in anode is needed to be additionally counted. Despite having only 43.5% of Nb_2O_5 in the anode the performance of the LIC prepared in this work is superior to the similar devices with higher Nb_2O_5 content which denotes the significance of the synergistic effect. Furthermore, the simplicity of the proposed synthesis methodology would facilitate carbon-coated metal oxide-containing nanocomposite utilization in energy storage applications.

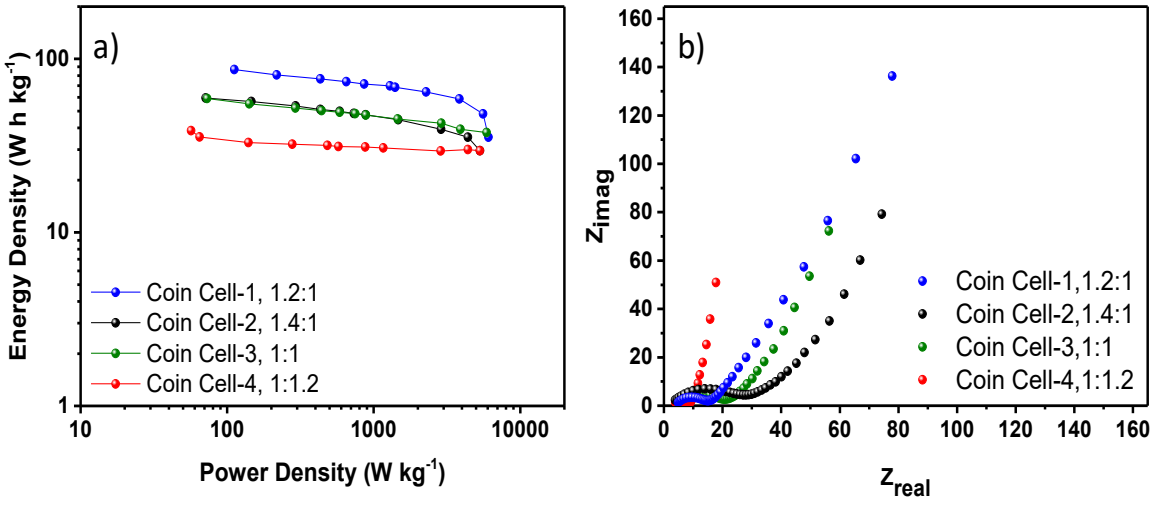

Figure 5-10 Optimization of the electrodes mass ratio ($m_{cathode}/m_{anode}$) (a) Ragone plot for coin cells with various electrodes ratios and (b) corresponding EIS measurements at OCV. Reproduced in adapted form from ref. 104 with permission from Elsevier.

5.4. Summary

In summary, microtubes of carbon with embedded niobium oxide nanoparticles is prepared using the in-situ polymerization of aniline in the presence of the niobium oxide precursor followed

by subsequent hydrothermal and heat treatment to introduce several key features to Li-ion device electrode structure. When used as anode materials, the N-NbOC exhibit a promising Li-ion storage, revealing a synergistic effect between the individual components. Besides, an improved rate capability compared to the pure Nb_2O_5 and excellent cycle stability is realized after 1100 cycles. Also, a N-NbOC//AC full cell is prepared demonstrating a notable electrochemical capacitive behaviour compared to similar devices that stems from the in-situ formed hollow carbon structure and uniformly distributed nanometer-sized orthorhombic niobium oxide with enhanced electronic features, which guarantees shortened diffusion pathway for Li-ions and fast energy storage performance. This work provides a facile strategy to improve the energy density of LICs and could be further extended to study of the in-situ polymerization of aniline in acidic transition metal oxides precursors, thus holding a great promise in nanocomposites preparation for hybrid capacitors applications.

6. MoS_2 nanosheets anchored to a nitrogen-doped crosslinked carbon structure towards a high-energy sodium-ion capacitor

6.1. Introduction

Electrochemical energy storage devices (EESs) have been addressing the progressively higher demand of storing and delivering energy. Among EESs, sodium-based storage systems have received great attention as sustainable and in-expensive devices.[33,35] Many researchers have devoted significant efforts toward designing new materials as sodium-ion hosts.[6,33,34,138] The popularity of this line of research stems from the remarkable electrochemical performances of several sodium-ion batteries (NIBs) and sodium-ion capacitors (NICs) that rival that of lithium-ion devices: the most-developed and forgoing storage systems now commercially available for various applications.[25] Moreover, using the world's non-toxic and abundant sodium resources is preferable to using its costly and finite lithium supply.[33]

Although the similar chemical properties and monovalency of Li and Na considerably ease choosing the best material for SIBs, a few critical criteria must be considered: (1) Na cations are larger and heavier than Li cations (1.06 Å *vs.* 0.76 Å).[98,139] Therefore, graphite, a common and an inexpensive anode material for Li-ion batteries (LIBs), cannot efficiently accommodate sodium ions in its interlayers;[33] (2) The standard electrochemical potential of Na^+/Na is higher than that of Li^+/Li, which critically challenges sustaining comparable energy and power densities; and (3) due to the larger volume expansion during ion intercalation/deintercalation, electrode pulverization is drastic in sodium-based devices compared to in lithium-based ones.[35,138] To address these issues, innovative electrode materials that can enhance sodium-ion storage performance are urgently needed. Recent studies have substantially contributed to meeting this need by developing

nanocomposite anode materials such as graphitized carbon, hard carbon, heteroatom doped carbon materials,[81,139,140] nanostructured transitional metal oxides, conversion materials,[141] and layered transition metal dichalcogenides (TMDs).[142] Yet, their low initial coulombic efficiency (ICE), unsatisfactory rate performance and limited energy density, especially for NICs, still necessitate extensive research.

In recent years TMDs, mainly MoS_2, have received considerable attention as anode materials for SIBs. MoS_2 is characterized by dynamic Van der Waals interactions between the layers and strong in-plane covalent bonds.[142] This structure is beneficial since weak van der Waals forces can theoretically accommodate ion insertion/extraction in an open/close reflex while under load or charging.[143] Binding energy calculations performed between Na and MoS_2 have uncovered their thermodynamically favorable reactions.[144] Despite its firm promise, MoS_2 has shown inferior rate capability due to electrode pulverization, structural degradation, and volume variations upon cycling.[145,146] To circumvent this problem, it is essential to design composite materials with an electrically conductive component that can provide a mechanical buffer during ion insertion. MoS_2 and its hybrids with graphene,[143] graphite,[105] CNT,[147] and carbon nanofibers[148] have been suggested. For instance, a comparison between MoS_2/S-doped graphene's sodium storage performance and that of MoS_2 showed 75% and 55.7% capacity retention, respectively, after 100 cycles, at the current density of 100 mA g^{-1}.[143] In another study, a MoS_2-carbon monolayer interoverlapped structure was used as the NICs anode, showing an excellent energy density of 111.4 Wh kg^{-1} at low rates. At moderate scan rates, however, a resistive behavior is detectable in cyclic voltammograms, which resulted in low energy density at high rates.[82] These studies suggested that the enhanced performance of MoS_2 is due to the synergistic coupling of the components and the composites' improved electronic conductivity. However, how the conductive

backbone affects the Na^+ diffusion coefficient and its variations during charge/ discharge remains unclear.

Herein, we report the use of a 3D hierarchical polyaniline structure on which to deposit molybdenum disulfide and synthesize a new MoS_2/NC hybrid as an anode material for Na^+ storage, as shown in **Scheme 1**. Protonated nitrogen atoms in the polyaniline structure are beneficial for electrostatic adsorption of molybdate anions and uniform dispersion of MoS_2. This unique design provides several improvements to Na^+ storage, including enhanced diffusional properties as well as robust superstructure to buffer volume changes during ion insertion/extraction. The half-cell sodium storage performance of MoS_2-NC shows significantly better rate performance than pure MoS_2. Moreover, a NIC comprising of the MoS_2/NC (anode) and activated carbon (AC, cathode) provides an excellent maximum power density and energy density of 19,060 W kg^{-1} and 58 Wh kg^{-1}, respectively. This device offers superior Na^+ storage behavior over similar reported devices due to the molecular interaction of carbon and MoS_2 that governs enhanced mass transport of Na^+ and boosts the integrity of the electrode upon cycling.

6.2. Experimental

6.2.1. Preparation of crosslinked polyaniline

Crosslinked polyaniline was chosen as a robust framework to buffer the electrode volume change during cycling, enhance the electronic conductivity, and provide immediate electrode/electrolyte contact by preventing nanosheets restacking during synthesis. We followed the synthesis procedure described in our previous work[106] adapted from literature.[50] In brief, 0.458 ml of aniline and 0.921 ml of phytic acid were dispersed in 2 ml of DDI (solution A). Then, 0.572 mg of ammonium persulfate was stirred in 1 ml of DDI (solution B). Solutions B and A were then

mixed, and polymerization of the aniline occurred within 30 minutes, resulting in a dark green hydrogel and crosslinked polyaniline. After immersing the polymer in DDI water for 72 hours and rinsing it repeatedly, the polymer was freeze dried for 2 days. This material was furthered treated for three purposes: (1) to deposit MoS_2 nanosheets (MoS_2/NC), (2) to serve as a cathode (AC) in a full NIC device after the carbonization and activation processes, and (3) to synthesize 3D-NC for comparative morphology and XPS studies.

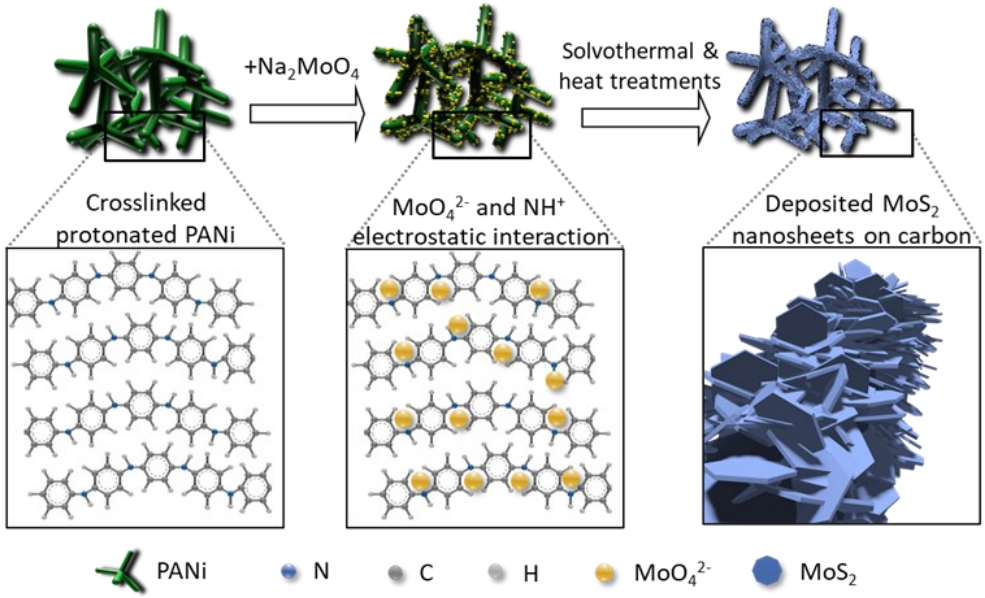

Scheme 6-1 The schematic of MoS_2/NC composites synthesis and how molecular interaction between nitrogen moieties and the molybdenum disulfide precursor during synthesis result in efficiently anchoring MoS_2 on to carbon core. This 3D structure ensures abundant ion insertion channels while buffering volume fluctuations during charge/discharge.

6.2.2. Preparation of MoS_2/NC, MoS_2, AC, and 3D-NC

To synthesize MoS_2/NC, 2-Sodium molybdate dehydrate (200 mg) was dissolved in DDI water (2 mL). The two synthesized polyaniline samples were then immersed in this solution, one for 24 hours and the other for 48, during which Molybdate was electrostatically adsorbed on the

positively charged amine groups. The resulting mixture was then filtered and washed with DDI. Thiourea (200 mg), dissolved in DDI, and sulfur powder (20 mg) dissolved in ethylene glycol and the above filtrate were mixed thoroughly. This dispersion was then transferred to an autoclave and treated at 120 °C for 10 h and another 10 h at 220 °C followed by washing and drying. The resulting powder was annealed to 800 °C in argon and was kept for 6 h at this temperature. The samples are called MoS_2/NC-1 or MoS_2/NC-2, depending on whether they had been immersed for 24 or 48 hours in the sodium molybdate solution, respectively. A bulk MoS_2 sample was prepared under identical conditions without polyaniline. 3D-NC was also prepared form the crosslinked polyaniline with the identical conditions as the nanocomposites without the presence of MoS_2 precursor, thiourea, and sulfur.

To synthesize AC, the crosslinked polyaniline was initially carbonized at 900 °C for 3 h under argon. Then, this sample was further activated with KOH with mass ratio of 3 (KOH /carbonized polymer) at 800 °C for 1 h. AC was repeatedly washed with DDI and ethanol followed by drying in vacuum oven overnight and was used as the cathode of NIC.

6.2.3. Materials characterization

Crystal structures were identified using X-ray diffraction (XRD, X'Pert Pro X-ray diffractometer, Panalytical B.V.) technique. X-ray photoelectron spectroscopy (XPS, Thermal Scientific K-Alpha XPS spectrometer) measurement was done to study the molecular interaction of the components. Using thermogravimetric measurements (TGA, on TA Instruments Q500), with a ramp rate of 10 °C min^{-1} starting from 50 °C to 650 °C, composition of each components was realized. Transmission electron microscopy (TEM, Philips CM10 transmission electron microscope) and scanning electron microscopy (SEM, LEO FESEM 1530) were conducted to

investigate the morphology of the materials. Elemental mappings were determined by electron energy dispersive analysis, EDX.

6.2.4. Electrode fabrication and electrochemical measurements

To prepare the electrodes, a conventional slurry preparation and coating techniques were utilized. The synthesized MoS_2-NC, a conductive agent (SuperP), and a binder (poly (vinylidene fluoride, (PVDF)) were mixed (ratio, 85:5:10) overnight in N-Methyl-2- pyrrolidone (NMP). Cu foils and Al foils were used as the current collectors. After slurry coating on the current collectors, the electrodes were dried in a vacuum oven at 80 ℃ overnight. Then they were cut and pressed before coin cell assembly with a mass loading of ~ 1 mg cm^{-2}. The CR2032 coin cells were assembled in an argon-filled glovebox with the working electrode and a piece of sodium foil as the reference and counter electrodes for half-cell studies. The electrodes were separated by a Celgard 2500 membrane wetted by the 1.0 M $NaClO_4$ in 1:1 (v/v) mixture of ethylene carbonate (EC) and diethyl carbonate (DEC) as the electrolyte. For the NIC devices, MoS_2/NC-1 electrodes were presodiated by direct contact between the electrodes and the Na foil for several hours. AC electrodes were used as the cathode of NICs where the optimized mass ratio of anode to cathode was 2:1, and other components of the NIC were identical to the half-cell assembly. The electrochemical studies including the electrochemical impedance spectroscopy (EIS), cyclic voltammetry (CV) and linear polarization resistance (LPR), were conducted using a Gamry potentiostat (Gamry Instruments, interface 1000). The electrical conductivity was measured using a homemade two-point-probe technique coupled with LPR. The galvanostatic charge/discharge cycling was conducted between 0.05 to 3 V *vs*. Na/Na^+ for the half-cell and between 0.6 to 3.6 V for the full cell at different current densities. Galvanostatic charge/discharge cycling and galvanostatic intermittent titration (GITT) were studied using a Land CT2001A battery tester. For

the GITT measurements, coin cells with sodium foil as the counter and reference electrode and the synthesized materials as the working electrode were charged/discharged with a constant current density of 10 mA g^{-1} for 10 minutes. The current is then removed for 1 h to relax the system back to the equilibrium. This procedure was repeated to reach the cut-off voltage limitations (0.05 to 3 V *vs*. Na/Na^{+}).

6.3. Results and discussion

6.3.1. Morphology, structure, and composition of as-synthesized MoS_2/NC

The MoS_2/NC composite materials were prepared by a facile solvothermal reaction followed by an annealing process using polyaniline as a framework for the deposition of MoS_2 nanosheets. The morphologies of 3D-NC and MoS_2/NC-1 were observed by scanning electron microscopy (SEM). As shown in **Figure 1a**, 3D-NC resembles a 3D microporous structure with branch sizes in a range of~200 nm. Such a structure can hinder MoS_2 aggregation and electrode pulverization during charge and discharge. Moreover, it offers highly conductive pathways (242 S m^{-1}, measured using LPR) for electrons compensating for the bulk MoS_2's low electronic conductivity (10^{-4} S m^{-1}).[149] **Figures 6-1(b-g)** show SEM, TEM and EDX images of MoS_2/NC-1. As evidenced by TEM and the EDX, several layers of MoS_2 with~100 nm dimensions are uniformly distributed on the 3D-NC scaffold. The crystal structures of the as-synthesized products were studied by XRD. **Figure 6-1 (h)** exhibits the XRD pattern of MoS_2/NC-1 and MoS_2/NC-2. The detectable diffraction peaks at 2θ 14.1°, 33.25°, 39.34°, 49.59°, and 59° matched well with the (002), (101), (103), (105), and (110) planes of the 2H-MoS_2 (JCPDS No. 77-1716).

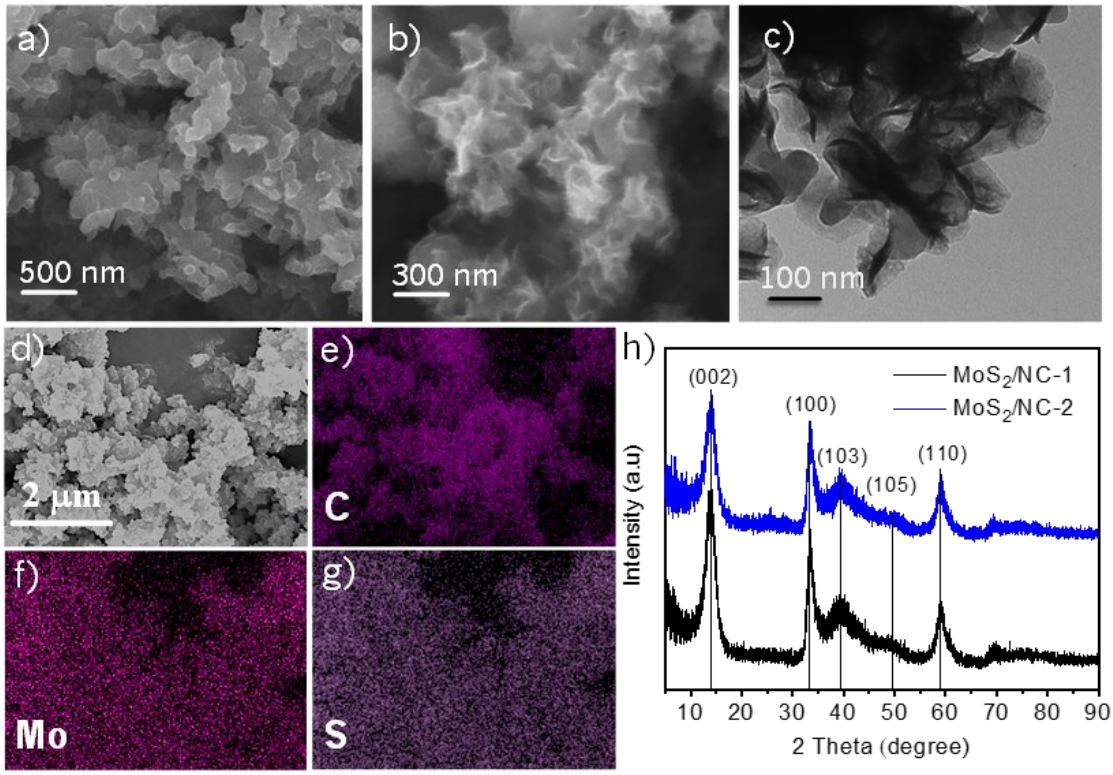

Figure 6-1 (a) SEM images 3D-NC and (b) MoS2/NC-1, (c) TEM image of MoS2/NC-1 (d-g) elemental mapping of C, Mo and S and the corresponding SEM image, (h) XRD pattern of MoS2/NC nanocomposites.

The chemical states of the elements in MoS_2/NC-1 were analyzed using X-ray photoelectron spectroscopy (XPS). The characteristic high-resolution spectra of Mo 3*d* is deconvoluted into 4 major peaks: 229.27 eV and 232.48 eV, which can be assigned to Mo^{4+} $3d_{5/2}$ and Mo^{4+} $3d_{3/2}$, respectively, in agreement with 2H-MoS_2;[150] and 235.71 eV assigned to Mo^{6+}, suggesting partial oxidation of Mo during the solvothermal process; and 226.55 eV for S *2s* (**Figure 6-2 (a)**).[151] **Figure 6-2 (b)** represents the high-resolution S 2p region for MoS_2/NC-1, consisting of a single doublet of 2 $p_{1/2}$ (163.2 eV) and S $2p_{3/2}$ (162.01 eV), attributed to the existence of S^{2-}.[152] Comparison of the Mo *3d* and S *2p* spectra of the bulk MoS_2 and MoS_2/NC-1 illustrates an obvious peak shift to the lower binding energy, presenting a higher electron density

around MoS_2 in the composite. On the other hand, comparison of the N *1s* of 3D-NC and MoS_2/NC-1 in **Figure 6-2 (c)** shows a blue shift for N *1s*-pyrrolic of MoS_2/NC-1, indicating a possible shift of electron density from nitrogen pyrrolic moieties in 3D-NC to MoS_2, as it is generally realized that nitrogen dopants provide electron-rich centers in carbon materials.[153] This finding suggests that pyrrolic moieties plays a pivotal role as the nucleation sites for MoS_2 growth, resulting in a robust composite structure for reversible sodium-ion storage. The composition of each component is studied using thermogravimetric analysis (TGA). As can be seen in **Figure 6-2 (d),** the composites are decomposed in air through two main reactions. According to the derivative thermogravimetric (DTG), MoS_2 decomposes to MoO_3 between 380-425 ℃ demonstrated with the initial peak centered at 400 ℃; and 3D-NC is burnt between 425-520 ℃ reflected with the second peak in DTG, centered at 443 ℃.[154] Based on these curves, the MoS_2 compositions in MoS_2/NC-1 and MoS_2/NC-2 are calculated to be 52% and 65%, respectively.

6.3.2. Electrochemical properties tied with diffusion coefficient analysis

The insertion/extraction properties of Na^+ in the as-synthesized composites were investigated in half-cell configurations with sodium metal foil as both the counter and reference electrodes and the composites as the working electrodes. The cyclic voltammograms of MoS_2/NC-1 and MoS_2/NC-2 for the first three cycles at the scan rate of 0.1 mV s^{-1}, are shown in **Figure 6-3 (a)** and **Figure 6-4**, respectively. The first cathodic scan for these two samples contains three reductive peaks centered at 0.8, 0.5, and below 0.3 V *vs.* Na/Na^+ corresponding to the intercalation of Na^+ in MoS_2 interlayers, the passivating solid-electrolyte interface layer (SEI), and the succeeding conversion reaction of sodiated MoS_2 to Mo and Na_2S, respectively.[155,156]

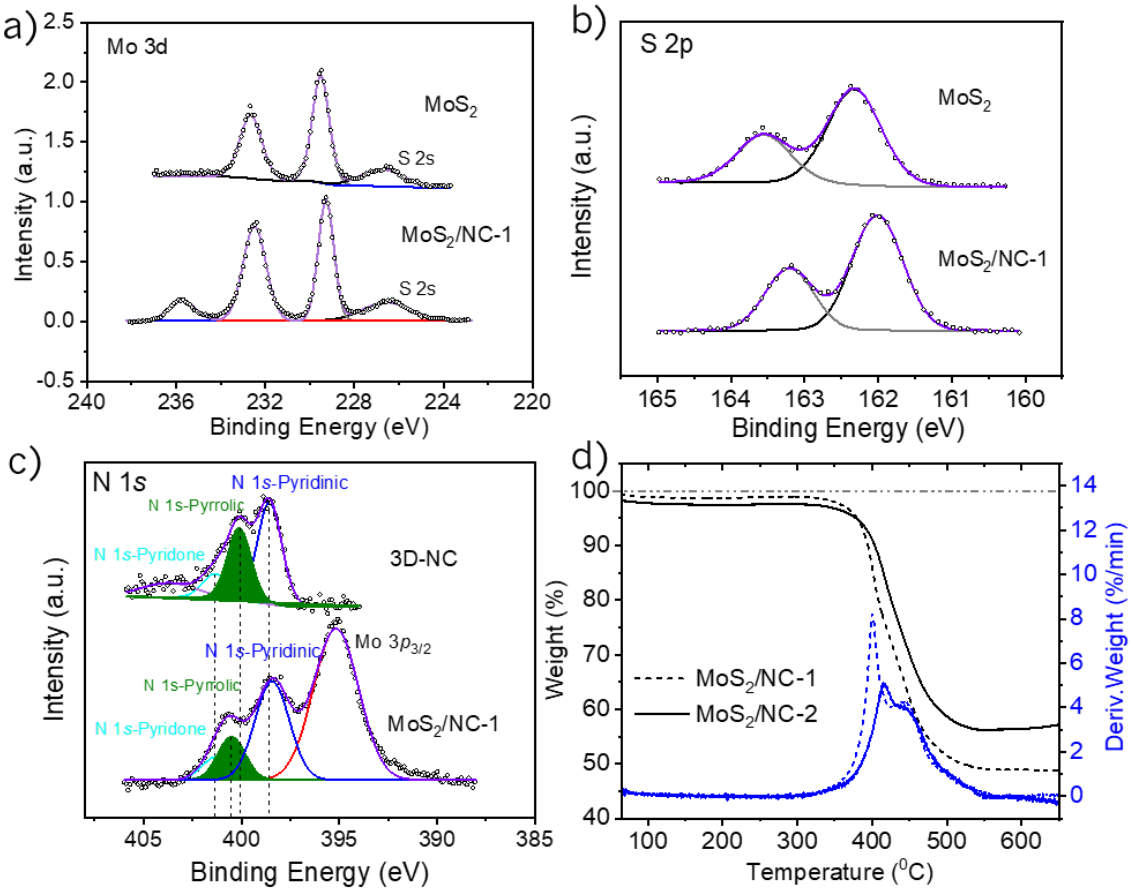

Figure 6-2 (a-b) XPS spectra of Mo 3d, S 2s core level peak regions in MoS_2/NC-1 and MoS_2; (c) comparison of N 1s binding energy before and after the deposition of MoS_2; and (d) TGA and DTG curve of MoS_2/NC nanocomposites.

The second and third cathodic scans of MoS_2/NC-1 and MoS_2/NC-2 present a reversible broad peak at 0.7 V *vs.* Na/Na^+ and the small tail at the end of discharge curves. First anodic scan of the composites show one main peak at 1.7 and a broad peak at 2.49 V that are ascribed to the oxidation of Mo and decomposition of Na_2S according to the following reaction:[155]

$$Na_xMoS_2 + (4-x)Na^+ + (4-x)e^- \Leftrightarrow Mo + 2Na_2S$$

In contrast, the second and the third cathodic scans of MoS_2 (**Figure 6-4 (b)**) do not overlap, signaling an irreversibility in Na^+ storage. These performances may suggest that the MoS_2/NC's structural distortion during ion insertion/extraction is supressed compared to pure MoS_2, highlighting the significance of a mechanical buffer presence in the MoS_2/NC composites.[157]

The initial charge/discharge voltage curves of MoS_2/NC composites were measured between 0.05 and 3.00 V *vs*. Na/Na^+ at a constant current density of 0.05 A g^{-1}. **Figure 6-3 (b)** shows the charge and discharge curves of MoS_2/NC-1, which exhibit a voltage plateau at around 1.8 during the first charge that agrees with the identified peak in the CV curves for MoS_2/NC-1.[157] Here it should be noted that using Raman spectroscopy, the degree of graphitization (I_D/I_G) of the 3D-NC sample was measured to be 1.03 (shown in **Figure 6-5**) indicating that the carbon is partially disordered.[50] The Na^+ intercalation's signature into disordered carbon material is a voltage plateau around 0.1 V *vs*. Na/Na^+.[158] Since there is no observable plateau at the end of the discharge curves of the MoS_2/NC composite, the ion intercalation in carbon component is not considered. The initial capacities based on discharge and charge are 545.8 and 401.1 mA h g^{-1}, corresponding to the ICE of 73.5%. The ICE improves to 91.8% and 96.2% during the second and third cycles, respectively. The charge and discharge curves of the MoS_2 and MoS_2/NC-2 are shown in **Figure 6-6**. Bulk MoS_2 delivers ICEs of 70% for the initial cycle, reaching 91.5% after the third cycle, confirming the immature SEI formation compared to MoS_2/NC-1. Although MoS_2/NC-2 provides higher initial discharge capacity, the initial ICE is only 67%. This low ICE could arise from the high concentration of MoS_2 nanosheets, resulting in more irreversibility due to conversion reactions compared to MoS_2/NC-1.[159,160]

The rate capability of the MoS_2 and its' derivatives was further evaluated at different current densities as shown in **Figure 6-3 (c)**. MoS_2/NC-1 exhibit the best rate performance,

maintaining 67% of its initial capacity when the current density increased from 0.05 to 2 A g^{-1}. This retained capacity is significantly higher than that of MoS_2/NC-2 (40%) and bulk MoS_2 (10%), presumably due to better electronic conductivity and/or diffusional properties. The cycling performance of the three synthesized samples is provided in **Figure 6-3 (d)**.

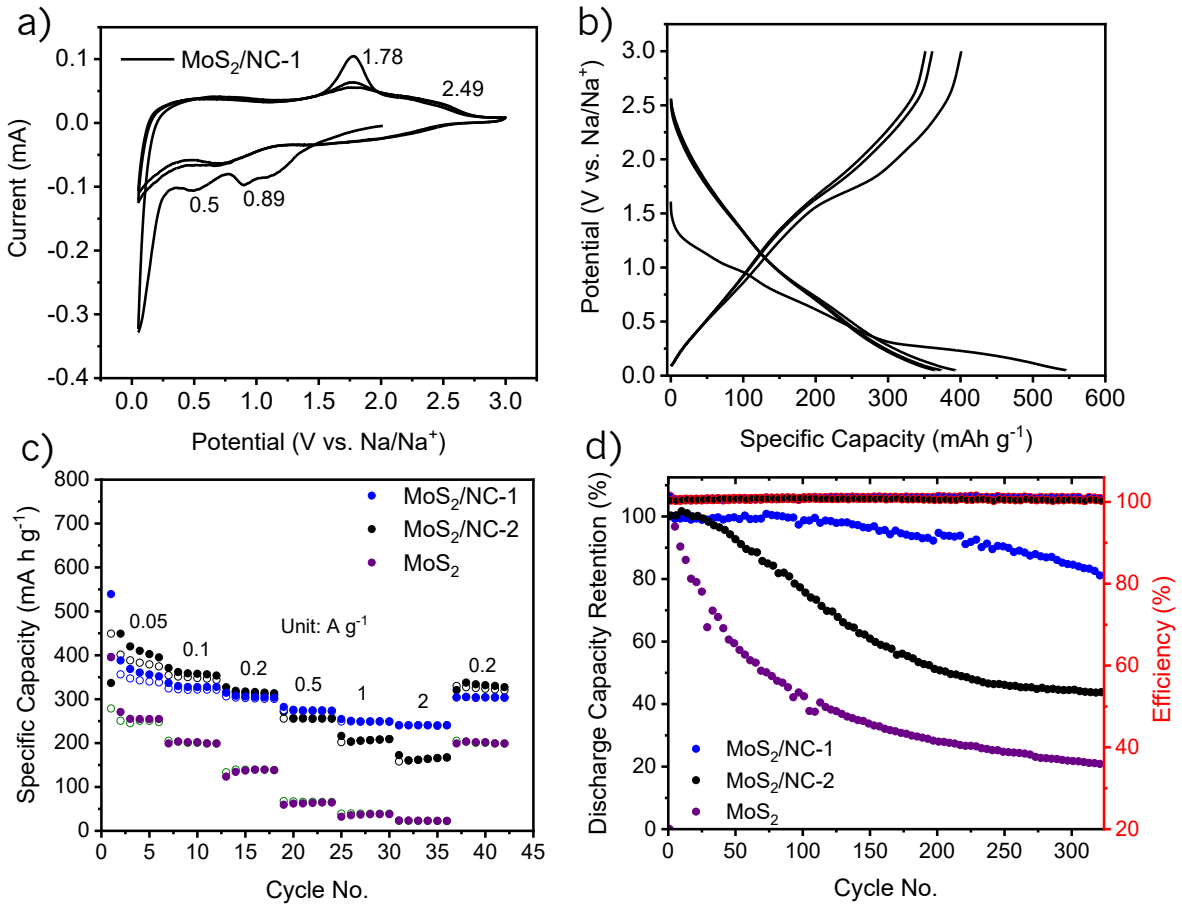

Figure 6-3 (a) First three CV curves of MoS_2/NC-1 nanocomposite electrode at 0.1 mV s^{-1} in a voltage window of 3.0–0.05 V; (b) Galvanostatic charge and discharge curves of MoS_2/NC-1 composite electrode at a current density of 50 mA g^{-1} for the first three cycles; (c) Rate capability of MoS_2/NC nanocomposites and bulk MoS_2 and (d) their corresponding cycling performance.

MoS_2/NC-1 possesses a noticeably higher capacity retention of 81.13% after 320 cycles at 0.5 A g^{-1} compared with MoS_2/NC-2 (43.8%) and MoS_2 (29.8%). The rapid capacity drop of MoS_2 originates from significant volume variation and structure destruction during sodiation/desodiation. Likewise, MoS_2/NC-2 with lower carbon content than that of MoS_2/NC-1 (13% carbon content difference) shows inferior capacity retention.[146] This behavior may have emerged for two primary reasons: (1) inadequate percolation of the conductive network in MoS_2/NC-2 composite and (2) agglomeration of MoS_2 nanosheets due to their high concentration.[161] These hypothesis were further studied by EIS measurements **(shown in Figure 6-7)** The calculated charge-transfer resistance (R_{CT}) of MoS_2/NC-1, MoS_2/NC-2, and MoS_2 are, 166.4 Ω, 163.4 Ω, and 160.5 Ω, respectively. Since the samples' R_{CT}s have maximum difference of 3%, we concluded that change in conductivity may not be the sole reason behind different rate performances of the synthesized samples. To examine the second hypothesis GITT measurements are done.

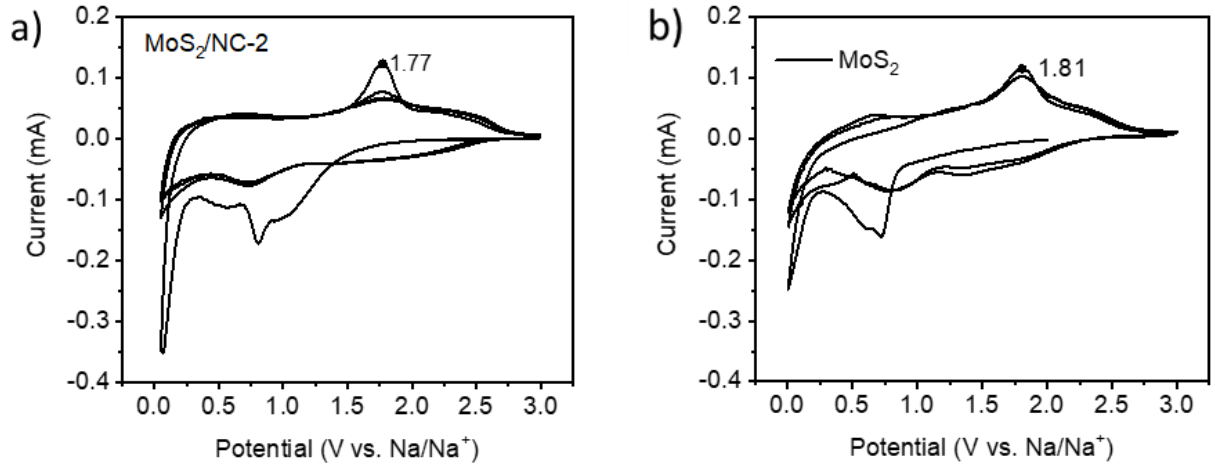

Figure 6-4 Cyclic voltammograms of (a) bulk MoS_2 and (b) MoS_2/NC-2 with scan rate of 0.1 mV s^{-1} with the voltage range of 3-0.05 V vs. Na/Na^+ for the first three cy cycles.

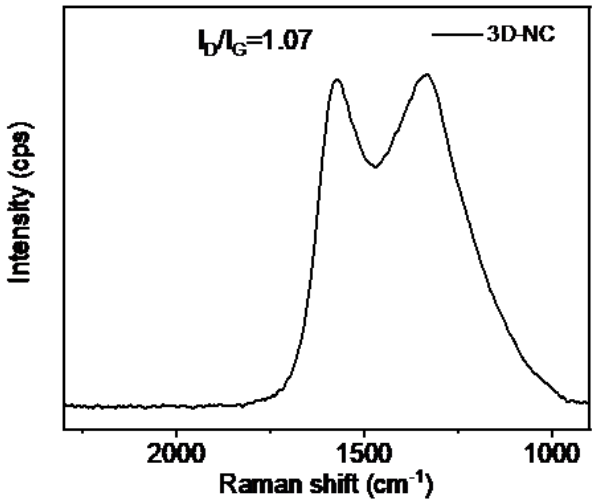

Figure 6-5 Raman spectra of 3D-NC and its relative ratio of I_D to I_G

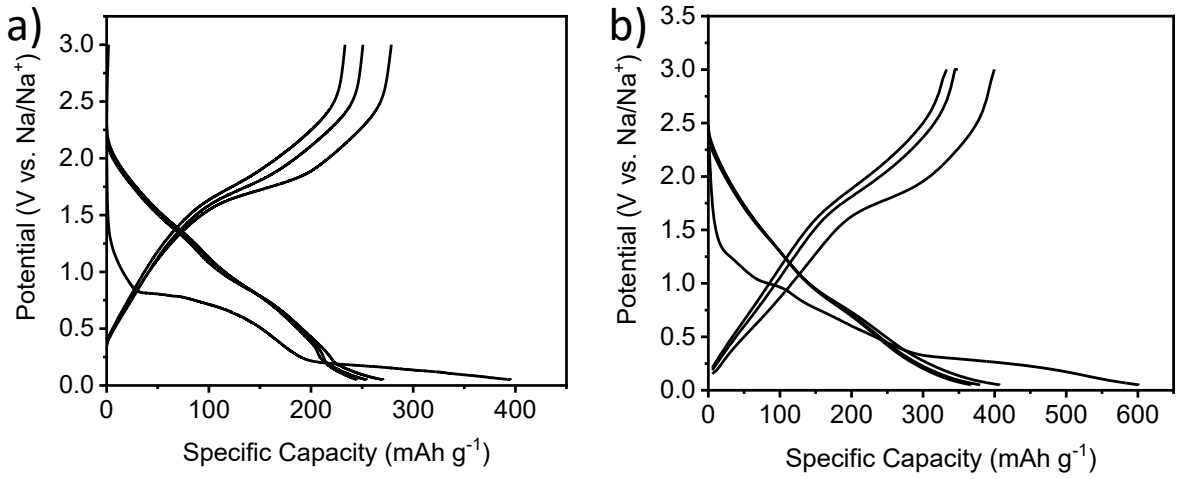

Figure 6-6 Galvanostatic charge/discharge curves of (a) MoS_2, and (b) MoS_2/NC-2 electrode at a current density of 50 mA g^{-1} for the first three cycles.

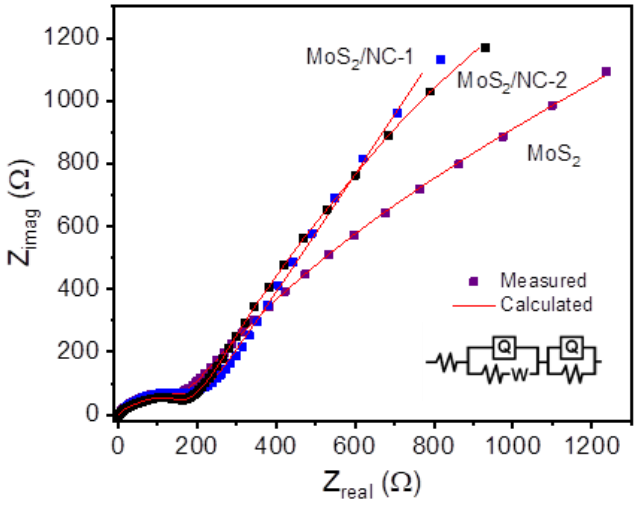

Figure 6-7 EIS spectra of MoS_2, MoS_2/NC-2, MoS_2/NC-1 electrodes at open circuit voltage after 5 galvanostatic charge/discharge cycles.

Figure 6-8 and **Figure 6-9 (a)** depict the GITT steps and curves for MoS_2/NC-1. The Na^+ diffusivity of the synthesized materials is calculated based on the GITT measurements using the following formula:[93]

$$D = \frac{4}{\pi}\left(\frac{IV_m}{Z_A FS}\right)^2 \left(\frac{dE(\delta)}{d\delta} / \frac{dE(t)}{d\sqrt{t}}\right)^2 \quad (6\text{-}1)$$

where I denotes the constant current applied during pulse time; V_m is the molar volume of the electrode; F is the Faraday's constant; S is the electrode/electrolyte interface area; and Z_A is the charge number. dE(δ)/dδ is the change in steady state voltages before and after each titration steps. dE/d$\sqrt{t}$ is the change of the voltages during the charge/discharge time (t).[93] Equation 6-1 can be simplified into Equation 6-2 if (1) dE(δ)/dδ and (2) dE/d$\sqrt{t}$ show a linear behavior.[162] The validity of these assumptions has been confirmed and is shown in **Figures 4b-4d** and equation 2 was used for the calculation of ion diffusitivty.

$$D = \frac{4}{\pi\tau}\left(\frac{m_B V_m}{M_B S}\right)^2 \left(\frac{\Delta E_S}{\Delta E_t}\right)^2 \quad (6\text{-}2)$$

τ is the pulse duration; M_B is the molar weight, and m_B is the mass of the electrode; ΔE_s is the change in two consecutive open circuit potentials after rest; ΔE_t is the difference in potential after each titration step. As shown in **Figure 6-9 (b)**, the steady state voltage is divided in to three different regions within which the $dE(\delta)/d\delta$ is considered linear. This categorization is used as a guidance to verify the linearity of $dE/d\sqrt{t}$ where five galvanostatic pulses are randomely chosen in each region, and voltage changes are plotted against $t^{0.5}$. As can be seen in **Figure 6-9(c)** and **Figure 6-9 (d)**, linearity is controlled in all three regions, validating Equation 6-2 for ion diffusitivity calculations.

Figure 6-9 (e) depicts the apparant diffusion coefficients (D_{Na+}) for the Na^+ obtained from GITT during the second discharge cycle. During sodiation, where Na^+ intercalates to the interlayer of the structures, the MoS_2/NC-1 nanosomposite reveals a superior mass transport of Na^+, agreeing with the rate capability studies. D_{Na+} values for all three samples show fluctuations, signaling the dependence of D_{Na+} on the state of charge, as also reported in the literature.[163–165] The values inside **Figure 6-9 (e)** shows the initial voltage of the galvanostatic pulse, corresponding to the shown composition. The diffusion coefficient variations for all three samples, start with the first few discharge cycles and continue to drop until the voltage is lower than 1.4 V, approximately. From there, for MoS_2, two minima around 0.8 V and 0.3V, are recognized, referring to the two voltage plateaus in the CCCD curves for Na^+ intercalation and conversion reactions, respectively. Generally, the minimas of the diffusion coefficient values in the GITT analysis are indicative of structural rearrangements.[93,163] For instance, insights on Na^+ storage mechanism in hard carbon showed higher diffusitivity values at the beginning of ion insertion during GITT. The author

further explains that initial sodiation is easier than when most of the sites are sodiated, because new ions have to overcome the repulsive charge gradient resulted from previously inserted ions.[166] The drastic and abrupt diffusion coefficient fluctuations for MoS_2 below 0.6 V compared to the small gradual drop for MoS_2/NC-1 may represent several major points: (1) the integrity of the MoS_2/NC-1 nanocomposite in which the 3D-NC has a buffering role, maintaining the nanocomposite's open framework and increasing accessible sites for easier insertion of Na^+ (2) the superior mass transport properties of MoS_2/NC-1, manifesting the highest apparent diffusion coefficient values compared to other samples;[165] and (3) the severe D_{Na+} drop for MoS_2/NC-2 compared to MoS_2/NC-1 before the onset of the conversion reaction (V> 0.5), demonstrating the effect of carbon: MoS_2 composition on Na^+ intercalation kinetics. It is crucial to mention that the higher diffusion coefficients can be also attributed to higher adsorption energy of Na^+ and increased favorable kinetics. However, theoretical studies have shown higher affinity of Na^+ towards MoS_2 than that of, for instance, heterointerphase of MoS_2 and graphene.[167] The higher apparent diffusion coefficient of MoS_2/NC-1 than that of MoS_2/NC-2 indicates the effect of structural arrangments exceeds that of adsorption energy of Na^+ twards the electrode surface. Apparent D_{Na}+ values are also calculated based on galvanostatic charging steps and are presented in **Figure 6-9 (f)**. Again MoS_2/NC-1 shows the highest D_{Na}+ values over the composition range involved in the titration.

6.3.3. MoS_2/NC//AC: a hybrid high-rate sodium-ion capacitor

NICs are designed to provide higher power energy than that of sodium-ion batteries (NIBs) and higher energy density than that of capacitors.[2] They have two electrodes in which reactions (intercalation, conversion, and/or redox) occur on the anode side, and physical separation of charges takes place on the cathode. Although this design ensures fast dynamics on the cathode and

high charge storage on the anode, kinetic imbalance between the two greatly hinder NICs development.[168] As a result, a high-power anode is a crucial component of high-rate NICs. Here, a NIC device with presodiated MoS2/NC-1 as the anode and activated AC as the cathode has been prepared and its electrochemical properties are studied (**Figure 6-10**).

It is well understood that presodiation not only provides higher energy density for NICs by widening the operating voltage window, but also compensates for Na^+ loss during metal dissolution and immobilization in SEI layer during first few cycles.[169] Therefore, to enhance the electrochemical properties of the prepared NIC, the anode has been presodiated by using a direct contact method according to a previous study.[169] The half-cell Na^+ charge storage of AC is provided in Chapter 4 of this thesis, demonstrating a high capacitance of 145 F g^{-1} at 50 mA h g^{-1} and long cycle life with capacitance retention of 80% after 1000 cycles, when charged to 4.4 V *vs.* Na/Na^+. The best voltage range has been chosen based on the CV curves results and long cycling performances (**Figure 4-6**).

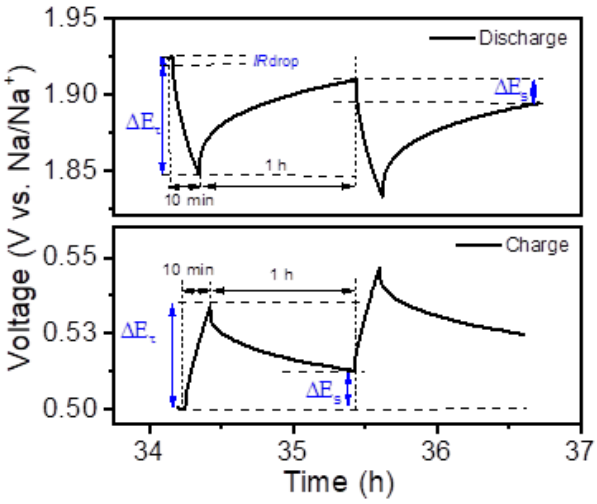

Figure 6-8 GITT program steps during discharge and charge

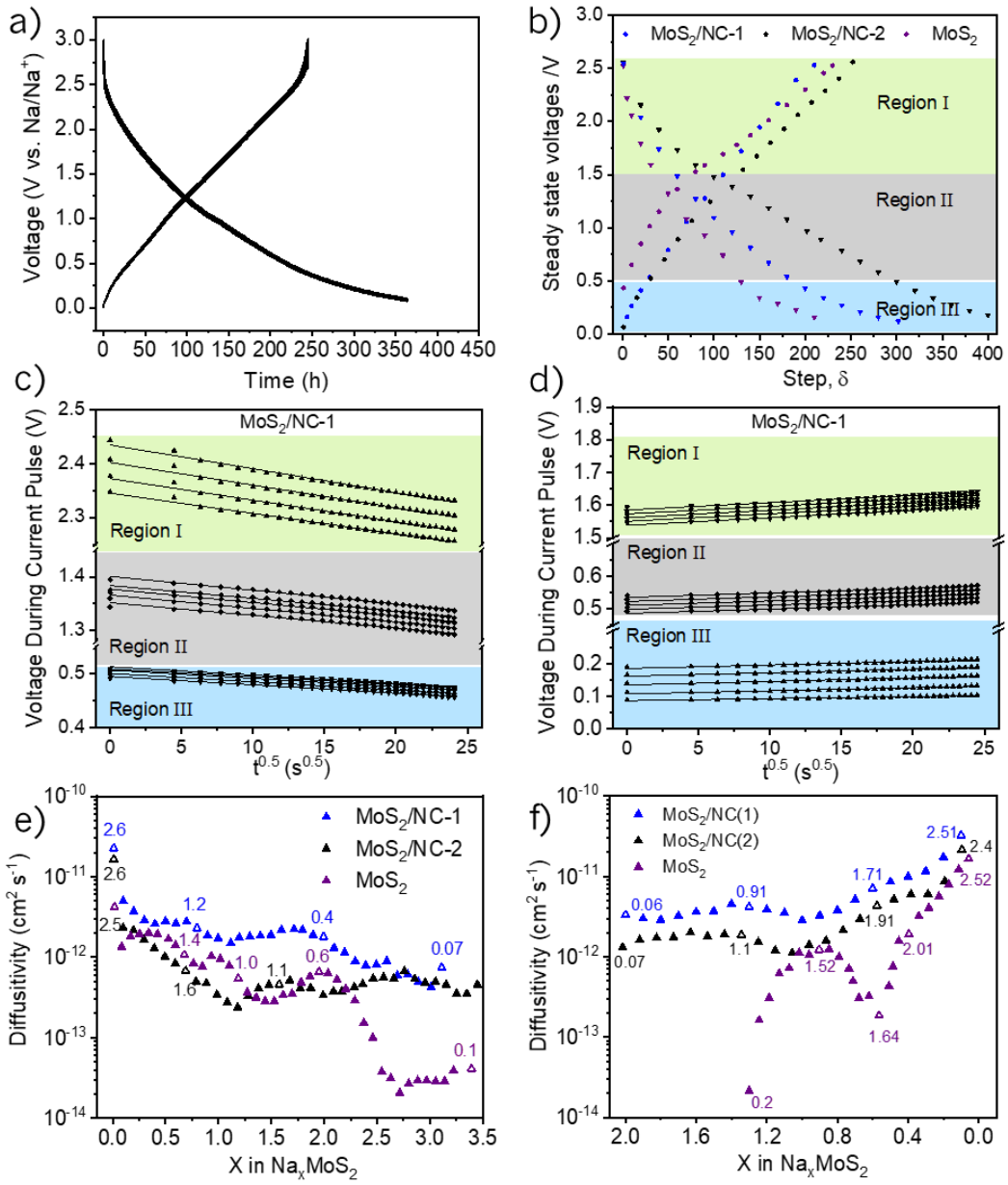

Figure 6-9 (a) GITT curves of MoS2/NC-1. The GITT test was performed by charging/discharging the electrode at a current pulse of 10 mA g^{-1} for 10 min and a relaxation of 60 min; (b) linear dependence of E(δ) on δ is fulfilled; (c) and (d) linearity of voltage during the current pulse with t^0.5 (second criteria of Equation 6-1 is fulfilled); (e) diffusion coefficient calculations based on e)discharge; and f)charge (numbers inside Figure (e) and (f) show the corresponding potential values (V vs. Na/Na^+).

Figure 6-10 (a) shows the optimization of the voltage range. The upper and lower voltage limits are set at 3.6 V and 0.6 V, respectively, to avoid the decomposition of the electrolyte. CV curves at different scan rates show a quasi-rectangular profile with one anodic and one cathodic broad peak, which may be indicative of the intercalation pseudocapacitance behavior (**Figure 6-10 (b)**).[47] Constant current charge/discharge curves, as shown in **Figure 6-10 (c)** and **Figure 6-11**, also resemble a quasi-linear profile, confirming fast surface reactions.[2] It is worth mentioning that the charge storage capacity of presodiated NIC is higher than that of NIC without presodiation at slow rates, suggesting the significance of possible Na^+ deficiency (shown in **Figure 6-12**); the difference, however, continues to decrease since a kinetic barrier is a limiting factor for charge storage at high rates .

The energy and power densities have been calculated based on the total mass of active materials in both electrodes, using charge/discharge curves, and the result is shown in a Ragone plot (**Figure 6-10 (d)**) The NIC device can provide an energy density of 58 Wh kg^{-1} at 197.6 W kg^{-1} and maintain energy density of 32.5 Wh kg^{-1} at 19060 W kg^{-1}. This device clearly shows a distinct power capability over other NICs in the literature,[82,83,170–172] as shown in the graph, owing to its unique structure, containing robust 3D carbon structure that allows for random orientation of MoS_2 nanosheets, resulting in abundant ion insertion channels. This design provides shortened diffusion path for ion transport, while performing a buffering role in limiting the MoS_2's crystal volume variations. Furthermore, the prepared NIC device maintains 70% of its initial capacitance after 5000 cycles at 0.7 A g^{-1}, representing a very stable performance because of suppressed structural degradation offered by anchored MoS_2 nanosheets to the carbon framework upon long cycling.

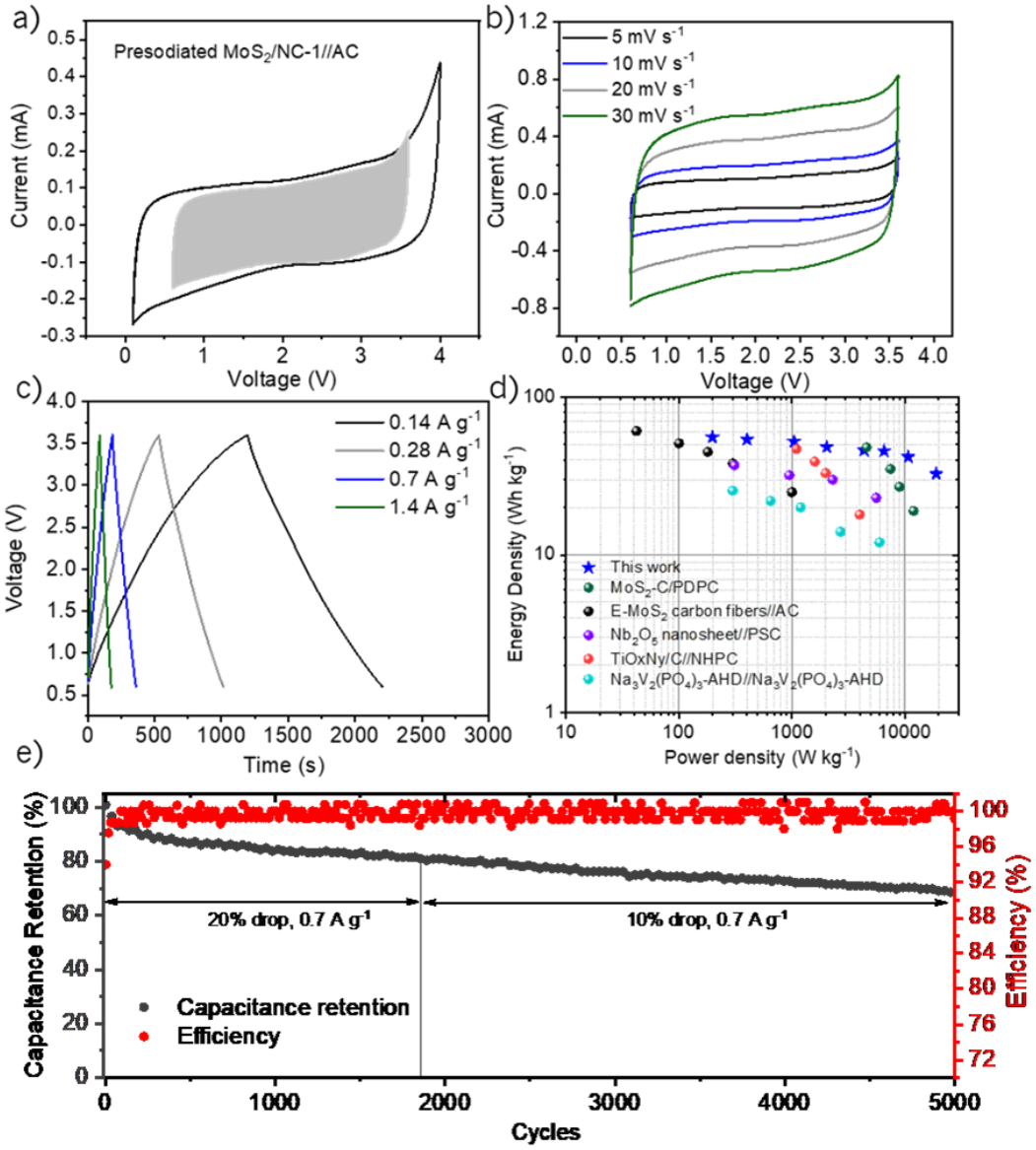

Figure 6-10 (a) Determining the NIC working voltage by CV at 5 mV s^{-1}; (b) CV curves of the NIC at various scan rates; (c) Galvanostatic charge discharge curves at different current densities; (d) Ragone plot of the prepared NIC device compared with MoS_2-C/PDPC,[82] E-MoS_2 carbon fibers//AC,[83] Nb_2O_5 nanosheet//PSC,[170] TiO_xN_y/C//NHPC,[171] $Na_3V_2(PO_4)_3$-AHD// $Na_3V_2(PO_4)_3$-AHD[172]; (e) cyclability of the NIC device at 0.7 A g^{-1}

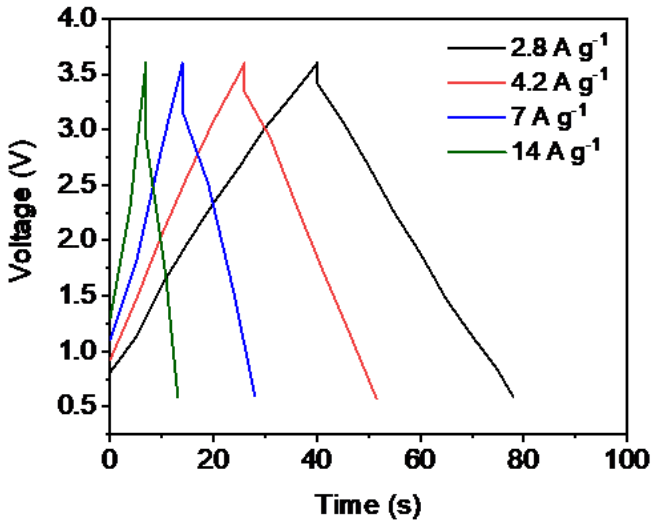

Figure 6-11 Galvanostatic charge/discharge for MoS_2/NC-1//AC with presodiated anode.

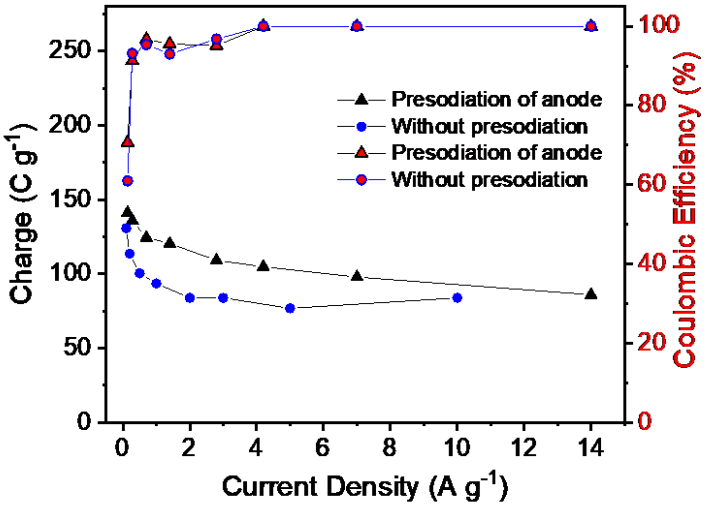

Figure 6-12 Comparison of the charge stored in presodiated MoS_2/NC-1//AC and MoS_2/NC-1//AC.

6.4. Summary

A novel nanocomposite of MoS_2 and a nitrogen-doped crosslinked carbon with 3D heterostructure was synthesized, providing high initial capacity of 545 mA h g^{-1} at 50 mA g^{-1}; and 240 mA h g^{-1}

at 2000 mA g^{-1}. The MoS_2/NC-1 also provides 81.13% of its initial capacity after 320 cycles at 0.5 A g^{-1}. XPS measurements of the nanocomposite reveal that pyrrolic nitrogen in the interconnected carbon has an electronic coupling with MoS_2, suggesting strong interactions between the two; therefore, inhibiting the volume expansion of MoS_2 that is commonly reported in the literature. Electrochemical studies reveal that MoS_2/NC-1 can significantly raise rate performance and cycle life compared to pure MoS_2; and GITT studies attribute the fast and stable Na^+ storage of the composite to an increased apparent Na^+ diffusion coefficient. MoS_2/NC-1 was used as anode in the NIC and at high power density (19060 W kg^{-1}), a high energy density of 58 Wh kg^{-1} was realized. Our findings provide new opportunities for developing high-rate and long-cycling anode materials for NICs and NIBs.

7. Conclusions and Future Work

In this thesis work, various electrode materials have been investigated for use in LICs and NICs. Considering the criteria for the materials selection, we first investigated a carbon material that, if its properties are tuned, can act both as the cathode of the hybrid devices and a framework for the in-situ incorporation or deposition of the intercalation-type materials to serve as the other electrode in hybrid systems. With the physicochemical and electrochemical characterization tools, we have explained the charge storage mechanisms and the underlying cause for any enhancement in electrochemical performances. The objectives described in the beginning of this thesis have been met, and a new understanding been provided of the surface and bulk properties of the synthesized nanocomposites and how they affect the power density and energy density of hybrid devices. This chapter outlines the conclusions from the previous chapters and presents proposed future work based on the work done in this research.

7.1. Conclusions

7.1.1. N-doped interconnected carbon structure from polyaniline as the cathode for hybrid capacitors

In this study, to prepare a nitrogen-doped high surface area carbon, first, an oxidative polymerization of aniline was done in the presence of phytic acid, which protonates nitrogen groups in aniline and directs the polymerization into an interesting interconnected morphology. Then the resulting polymer was heat treated, followed by KOH activation. The effect of activation temperature on the electrochemical performance of the synthesized samples revealed a trade-off between the specific surface area and the electronic conductivity. The maximum charge storage capacitance was obtained from the sample with the highest total pore volume and specific surface

area, confirming the significance of specific surface area on double layer capacitance. The half-cell electrochemical performance showed an improved specific capacitance of NAC-800-3 compared to the commercial activated carbon duo to (1) the unique morphology that enabled easy electrolyte infiltration and facilitated electron transfer, and (2) the heteroatom dopants that introduced pseudocapacitive charge storage. Also, the linear charge/discharge curves depict that the fast and capacitive charge storage mechanism which is expected from the cathode side is fulfilled. This study also provided the realization that the intermolecular interactions during aniline polymerization produce unique morphological features.

7.1.2. 3D N-doped Hybrid Architectures Assembled from 0D T-Nb_2O_5 Embedded in Carbon Microtubes toward High-rate Li-ion capacitors

Inspired by the polymerization of aniline in the presence of a multidentate acid in the first study, microtubes of carbon with embedded niobium oxide nanoparticles were prepared using the in-situ incorporation of the niobium oxide precursor during polymerization of aniline, followed by subsequent hydrothermal and heat treatments. This unique design offered several key features to the anode: (1) an interesting structure of microtubes with hollow interiors that shortened the electron transfer path and enhanced the electrode-electrolyte interface, (2) nano-size and well-distributed orthorhombic niobium oxide particles within the carbon microtubes that improved pseudocapacitive charge storage and enabled high-rate lithium-ion storage through the (001) plane, and (3) improved electronic conductivity as evidenced by EIS. Moreover, XPS analysis revealed a peak shift of Nb 3d, attributed to elevated electron density caused by N substituting for O around the Nb atom. This shift, together with an assigned peak to the O-Nb-N linkage of the sample after burning the carbon composition, confirmed nitrogen doping of the metal oxide, which may reduce the metal oxide band gap and contribute to increased electronic conductivity. The

simultaneous formation of carbon from polymer and niobium oxide from the niobium precursor offered a possible catalytic effect of the Nb atoms on graphitizing the carbon layers, as confirmed by HRTEM. The graphitized carbon layer is beneficial for mechanically maintaining the crystal structure during lithiation and delithiation. Overall, this work presents a new and straightforward strategy for enhancing the electrochemical performance of LICs. Additionally, this synthesis strategy could be further extended to the in-situ polymerization of aniline in the other acidic transition metal oxides precursors, offering a new design procedure.

7.1.3. MoS_2 nanosheets anchored to a nitrogen-doped crosslinked carbon structure towards a high-energy sodium-ion capacitor

In the last study, utilizing the 3D network of polyaniline from the first study, a new heterostructure nanocomposite of MoS_2 nanosheets and a nitrogen-doped crosslinked carbon was prepared. The unique morphology was achieved owing to the intermolecular interaction of doped polyaniline and molybdate moieties. XPS analysis revealed that pyrrolic nitrogen has an electronic coupling with MoS_2; thus, the volume variation of the electrode was suppressed upon cycling. Electrochemical studies revealed that the nanocomposite can significantly raise rate performance and cycle life compared to pure MoS_2 and GITT and EIS studies assigned the fast and stable Na+ storage of the composite to an increased apparent Na^+ diffusion coefficient. Using GITT technique, we not only confirmed that the Na+ apparent diffusion coefficient of nanocomposite showed superior mass transport properties compared to those of MoS_2, but also that the carbon framework plays a role in maintaining accessible sites for electron transfer during different states of charge. It was also realized that the carbon: MoS_2 composition affects the diffusional properties of the electrode. When used as an anode in a full cell NIC, the nanocomposite showed a high energy density and power density with promising cycling stability. The analysis of the surface

properties and the apparent diffusion coefficients of the nanocomposite and its variations during charge/discharge can be applied to other nanocomposites to further explain their electrochemical performances.

7.2. Future work

Future work based on the knowledge gained from this thesis could potentially improve the energy density, power density, and cycle life of hybrid devices. Several recommendations for this work are listed here and further explained later in this section. First, further analysis can be performed to deepen our understanding of the capacity fading of polyaniline-derived porous carbon when acting as the cathodes of hybrid capacitors. Second, doping of the polymer-derived activated carbon can be done with the intrinsic or extrinsic pseudocapacitive materials such as MoO_3 or NiO, to serve as the cathode of hybrid capacitors. Third, in-situ polymerization of aniline can be performed in the presence of multidentate and acidic precursors of pseudocapacitive materials. Another approach could be the use of the crosslinked polymer with doped nitrogen moieties that can serve as a scaffold for the deposition of TMDs as hybrid capacitor's anode materials.

7.2.1. Analysis of capacitance fading of hybrid capacitors' cathodes

To further enhance the cyclability of hybrid devices, a systematic analysis is required to understand the reason behind the cathode's capacitance fading. Using surface area analysis together with other physicochemical characterization after extended charge/discharge cycling, we can realize the relation or any trade-off between the surface area and carbon corrosion. Increasing the surface area, on the one hand, enhances the double layer capacitance. However, a higher degree of carbon activation results in the elevated creation of micropores and more functional groups

concurrently and thus increases the probability of carbon corrosion during cycling. Therefore, there might be a trade-off between the increased microporosity and degrading the electrode upon cycling. Novel strategies can be designed after the realization gained from extended cycling analysis to suppress the capacitance fading.

7.2.2. Doping porous carbon materials with pseudocapacitive materials for cathodes

As discussed in Chapter 1, a hybrid device stores energy with different charge storage mechanisms on its anode and cathode. This hybridization can be designed in more advances level, in which each electrode could store energy using multiple charge storage mechanisms, being capacitive, redox pseudocapacitive or intercalation pseudocapacitive. This hybridization level has been utilized to design various anodes in the literature. However, on the cathode side, the research has been mainly focused on capacitive mechanism using porous carbon materials doped with heteroatoms. The charge storage capacity of these materials could be further enhanced by doping these materials with pseudocapacitive metal oxides nanoparticles with suitable redox potential. For instance, the study performed in Chapter 4 can be extended to introducing metal oxides to the interconnected and highly porous carbon. The atomic composition of the metal oxide and carbon should be engineered such that the criteria of the cathode's electrochemical performance explained in Chapter 1 is fulfilled. It is critical to maintain the hierarchical structure of the electrode to prevent compromising on the device's rate performance.

7.2.3. Novel composites as hybrid capacitors anodes

In Chapter 5 and Chapter 6, novel synthesis routes are provided. Using the in-situ polymerization concept in Chapter 5, it is possible to design composite materials possessing novel morphology, enhanced electronic conductivity, and developed charge transport property. The benefits also

include fast and simple synthetic routes without using templates that can incorporate the insertion component in-situ. The 3D continuous electrical conduction pathway would benefit the realization of all the active sites for charge storage as it ensures fast electron and ion accessibility to the electrode. The design must be based on the acidity of the synthesis media and molecular interactions of the monomer/polymer and the metal oxide precursor. The synthesis methodologies introduced in Chapter 5 and 6 are recommended to be employed for various other metal oxides and transition metal dichalcogenides with precise morphological and compositional control that plays a vital role on the physical and electrochemical property of the anode.

REFRENCES

(1) *International Energy Outlook 2016*; 2016.

(2) Simon, P.; Gogotsi, Y.; Dunn, B. Where Do Batteries End and Supercapacitors Begin? *Science (80-.).* **2014**, *343* (6176), 1210–1211. https://doi.org/10.1126/science.1249625.

(3) Slater, M. D.; Kim, D.; Lee, E.; Johnson, C. S. Sodium-Ion Batteries. *Adv. Funct. Mater.* **2013**, *23* (8), 947–958. https://doi.org/10.1002/adfm.201200691.

(4) Cao, J.; Emadi, A. A New Battery/Ultracapacitor Hybrid Energy Storage System for Electric, Hybrid, and Plug-in Hybrid Electric Vehicles. *IEEE Trans. Power Electron.* **2012**, *27* (1), 122–132. https://doi.org/10.1109/TPEL.2011.2151206.

(5) Li, B.; Zheng, J.; Zhang, H.; Jin, L.; Yang, D.; Lv, H.; Shen, C.; Shellikeri, A.; Zheng, Y.; Gong, R.; Zheng, J. P.; Zhang, C. Electrode Materials, Electrolytes, and Challenges in Nonaqueous Lithium-Ion Capacitors. *Adv. Mater.* **2018**, *1705670*, 1–19. https://doi.org/10.1002/adma.201705670.

(6) Zhang, H.; Hu, M.; Lv, Q.; Huang, Z. H.; Kang, F.; Lv, R. Advanced Materials for Sodium-Ion Capacitors with Superior Energy–Power Properties: Progress and Perspectives. *Small* **2019**, *1902843*, 1–22. https://doi.org/10.1002/smll.201902843.

(7) Wang, G.; Zhang, L.; Zhang, J. A Review of Electrode Materials for Electrochemical Supercapacitors. *Chem. Soc. Rev.* **2012**, *41* (2), 797–828. https://doi.org/10.1039/c1cs15060j.

(8) Dubal, D. P.; Ayyad, O.; Ruiz, V.; Gómez-Romero, P. Hybrid Energy Storage: The Merging of Battery and Supercapacitor Chemistries. *Chem. Soc. Rev.* **2015**, *44* (7), 1777–1790. https://doi.org/10.1039/C4CS00266K.

(9) Plitz, I.; Dupasquier, A.; Badway, F.; Gural, J.; Pereira, N.; Gmitter, A.; Amatucci, G. G.

The Design of Alternative Nonaqueous High Power Chemistries. *Appl. Phys. A Mater. Sci. Process.* **2006**, *82* (4 SPEC. ISS.), 615–626. https://doi.org/10.1007/s00339-005-3420-0.

(10) Aravindan, V.; Cheah, Y. L.; Mak, W. F.; Wee, G.; Chowdari, B. V. R.; Madhavi, S. Fabrication of High Energy-Density Hybrid Supercapacitors Using Electrospun V2O5 Nanofibers with a Self-Supported Carbon Nanotube Network. *Chempluschem* **2012**, *77* (7), 570–575. https://doi.org/10.1002/cplu.201200023.

(11) Lim, E.; Jo, C.; Kim, H.; Kim, M.-H.; Mun, Y.; Chun, J.; Ye, Y.; Hwang, J.; Ha, K.-S.; Roh, K. C.; Kang, K.; Yoon, S.; Lee, J. Facile Synthesis of Nb 2 O 5 @Carbon Core–Shell Nanocrystals with Controlled Crystalline Structure for High-Power Anodes in Hybrid Supercapacitors. *ACS Nano* **2015**, *9* (7), 7497–7505. https://doi.org/10.1021/acsnano.5b02601.

(12) Kim, H.; Cho, M.-Y.; Kim, M.-H.; Park, K.-Y.; Gwon, H.; Lee, Y.; Roh, K. C.; Kang, K. A Novel High-Energy Hybrid Supercapacitor with an Anatase TiO 2 -Reduced Graphene Oxide Anode and an Activated Carbon Cathode. *Adv. Energy Mater.* **2013**, *3* (11), 1500–1506. https://doi.org/10.1002/aenm.201300467.

(13) Aravindan, V.; Reddy, M. V.; Madhavi, S.; Mhaisalkar, S. G.; Subba Rao, G. V.; Chowdari, B. V. R. Hybrid Supercapacitor with Nano-TiP2O7 as Intercalation Electrode. *J. Power Sources* **2011**, *196* (20), 8850–8854. https://doi.org/10.1016/j.jpowsour.2011.05.074.

(14) Gao, L.; Huang, D.; Shen, Y.; Wang, M. Rutile-TiO 2 Decorated Li 4 Ti 5 O 12 Nanosheet Arrays with 3D Interconnected Architecture as Anodes for High Performance Hybrid Supercapacitors. *J. Mater. Chem. A* **2015**, *3* (46), 23570–23576. https://doi.org/10.1039/C5TA07666H.

(15) Jain, A.; Aravindan, V.; Jayaraman, S.; Kumar, P. S.; Balasubramanian, R.; Ramakrishna,

S.; Madhavi, S.; Srinivasan, M. P. Activated Carbons Derived from Coconut Shells as High Energy Density Cathode Material for Li-Ion Capacitors. *Sci. Rep.* **2013**, *3* (1), 3002. https://doi.org/10.1038/srep03002.

(16) Li, B.; Dai, F.; Xiao, Q.; Yang, L.; Shen, J.; Zhang, C.; Cai, M. Nitrogen-Doped Activated Carbon for a High Energy Hybrid Supercapacitor. *Energy Environ. Sci.* **2016**, *9* (1), 102–106. https://doi.org/10.1039/C5EE03149D.

(17) Fan, W.; Zhang, C.; Tjiu, W. W.; Pramoda, K. P.; He, C.; Liu, T. Graphene-Wrapped Polyaniline Hollow Spheres As Novel Hybrid Electrode Materials for Supercapacitor Applications. *ACS Appl. Mater. Interfaces* **2013**, *5* (8), 3382–3391. https://doi.org/10.1021/am4003827.

(18) Kim, B. K.; Sy, S.; Yu, A.; Zhang, J. Electrochemical Supercapacitors for Energy Storage and Conversion. In *Handbook of Clean Energy Systems*; John Wiley & Sons, Ltd: Chichester, UK, 2015; pp 1–25. https://doi.org/10.1002/9781118991978.hces112.

(19) Conway, B. E. *Electrochemical Supercapacitors : Scientific Fundamentals and Technological Applications*; New York: Kluwer Academic / Plenum Press, 1999.

(20) Shao, Y.; El-Kady, M. F.; Sun, J.; Li, Y.; Zhang, Q.; Zhu, M.; Wang, H.; Dunn, B.; Kaner, R. B. Design and Mechanisms of Asymmetric Supercapacitors. *Chem. Rev.* **2018**, *118* (18), 9233–9280. https://doi.org/10.1021/acs.chemrev.8b00252.

(21) Zhang, L. L.; Zhao, X. S. Carbon-Based Materials as Supercapacitor Electrodes. *Chem. Soc. Rev.* **2009**, *38* (9), 2520. https://doi.org/10.1039/b813846j.

(22) Yu, G.; Xie, X.; Pan, L.; Bao, Z.; Cui, Y. Hybrid Nanostructured Materials for High-Performance Electrochemical Capacitors. *Nano Energy* **2013**, *2* (2), 213–234. https://doi.org/10.1016/j.nanoen.2012.10.006.

(23) Jiang, Y.; Liu, J. Definitions of Pseudocapacitive Materials: A Brief Review. *ENERGY Environ. Mater.* **2019**, *2* (1), 30–37. https://doi.org/10.1002/eem2.12028.

(24) Augustyn, V.; Simon, P.; Dunn, B. Pseudocapacitive Oxide Materials for High-Rate Electrochemical Energy Storage. *Energy Environ. Sci.* **2014**, *7* (5), 1597. https://doi.org/10.1039/c3ee44164d.

(25) Li, M.; Lu, J.; Chen, Z.; Amine, K. 30 Years of Lithium-Ion Batteries. *Adv. Mater.* **2018**, *30* (33), 1800561. https://doi.org/10.1002/adma.201800561.

(26) Goodenough, J. B.; Park, K.-S. The Li-Ion Rechargeable Battery: A Perspective. *J. Am. Chem. Soc.* **2013**, *135* (4), 1167–1176. https://doi.org/10.1021/ja3091438.

(27) Hausbrand, R.; Cherkashinin, G.; Ehrenberg, H.; Gröting, M.; Albe, K.; Hess, C.; Jaegermann, W. Fundamental Degradation Mechanisms of Layered Oxide Li-Ion Battery Cathode Materials: Methodology, Insights and Novel Approaches. *Mater. Sci. Eng. B* **2015**, *192*, 3–25. https://doi.org/10.1016/j.mseb.2014.11.014.

(28) Xu, Qiang, and T. K. *Advanced Materials for Clean Energy*; Boca Raton, Florida : CRC Press, 2015.

(29) Deng, D. Li-Ion Batteries: Basics, Progress, and Challenges. *Energy Sci. Eng.* **2015**, *3* (5), 385–418. https://doi.org/10.1002/ese3.95.

(30) Goodenough, J. B.; Park, K. The Li-Ion Rechargeable Battery: A Perspective. *J. Am. Chem. Soc.* **2013**, *135* (4), 1167–1176. https://doi.org/10.1021/ja3091438.

(31) Liu, C.; Neale, Z. G.; Cao, G. Understanding Electrochemical Potentials of Cathode Materials in Rechargeable Batteries. *Mater. Today* **2016**, *19* (2), 109–123. https://doi.org/10.1016/j.mattod.2015.10.009.

(32) Collins, J.; Gourdin, G.; Foster, M.; Qu, D. Carbon Surface Functionalities and SEI

Formation during Li Intercalation. *Carbon N. Y.* **2015**, *92*, 193–244. https://doi.org/10.1016/j.carbon.2015.04.007.

(33) Delmas, C. Sodium and Sodium-Ion Batteries: 50 Years of Research. *Adv. Energy Mater.* **2018**, *8* (17), 1703137. https://doi.org/10.1002/aenm.201703137.

(34) Zhang, W.; Zhang, F.; Ming, F.; Alshareef, H. N. Sodium-Ion Battery Anodes : Status and Future Trends. *EnergyChem* **2019**, *1* (2), 100012. https://doi.org/10.1016/j.enchem.2019.100012.

(35) Liang, Y.; Lai, W.-H.; Miao, Z.; Chou, S.-L. Nanocomposite Materials for the Sodium-Ion Battery: A Review. *Small* **2018**, *14* (5), 1702514. https://doi.org/10.1002/smll.201702514.

(36) Wang, H.; Zhu, C.; Chao, D.; Yan, Q.; Fan, H. J. Nonaqueous Hybrid Lithium-Ion and Sodium-Ion Capacitors. *Adv. Mater.* **2017**, *29* (46), 1–18. https://doi.org/10.1002/adma.201702093.

(37) Wu, Z.-S.; Ren, W.; Wang, D.-W.; Li, F.; Liu, B.; Cheng, H.-M. High-Energy MnO 2 Nanowire/Graphene and Graphene Asymmetric Electrochemical Capacitors. *ACS Nano* **2010**, *4* (10), 5835–5842. https://doi.org/10.1021/nn101754k.

(38) Amatucci, G. G.; Badway, F.; Du Pasquier, A.; Zheng, T. An Asymmetric Hybrid Nonaqueous Energy Storage Cell. *J. Electrochem. Soc.* **2001**, *148* (8), A930. https://doi.org/10.1149/1.1383553.

(39) Jezowski, P.; Crosnier, O.; Deunf, E.; Poizot, P.; Béguin, F.; Brousse, T. Safe and Recyclable Lithium-Ion Capacitors Using Sacrificial Organic Lithium Salt. *Nat. Mater.* **2018**, *17* (2), 167–173. https://doi.org/10.1038/NMAT5029.

(40) Zuo, W.; Li, R.; Zhou, C.; Li, Y.; Xia, J.; Liu, J. Battery-Supercapacitor Hybrid Devices: Recent Progress and Future Prospects. *Adv. Sci.* **2017**, *4* (7), 1–21.

https://doi.org/10.1002/advs.201600539.

(41) Lee, B.-G.; Yoon, J.-R. Preparation and Characteristics of Li 4 Ti 5 O 12 Anode Material for Hybrid Supercapacitor. *J. Electr. Eng. Technol.* **2012**, *7* (2), 207–211. https://doi.org/10.5370/JEET.2012.7.2.207.

(42) Zhong, C.; Deng, Y.; Hu, W.; Qiao, J.; Zhang, L.; Zhang, J. A Review of Electrolyte Materials and Compositions for Electrochemical Supercapacitors. *Chem. Soc. Rev.* **2015**, *44* (21), 7484–7539. https://doi.org/10.1039/C5CS00303B.

(43) Ding, J.; Hu, W.; Paek, E.; Mitlin, D. Review of Hybrid Ion Capacitors: From Aqueous to Lithium to Sodium. *Chem. Rev.* **2018**, *118* (14), 6457–6498. https://doi.org/10.1021/acs.chemrev.8b00116.

(44) Borchardt, L.; Oschatz, M.; Kaskel, S. Tailoring Porosity in Carbon Materials for Supercapacitor Applications. *Mater. Horiz.* **2014**, *1* (2), 157–168. https://doi.org/10.1039/C3MH00112A.

(45) Wang, J.; Kaskel, S. KOH Activation of Carbon-Based Materials for Energy Storage. *J. Mater. Chem.* **2012**, *22* (45), 23710. https://doi.org/10.1039/c2jm34066f.

(46) Sun, F.; Gao, J.; Liu, X.; Pi, X.; Yang, Y.; Wu, S. Porous Carbon with a Large Surface Area and an Ultrahigh Carbon Purity via Templating Carbonization Coupling with KOH Activation as Excellent Supercapacitor Electrode Materials. *Appl. Surf. Sci.* **2016**, *387*, 857–863. https://doi.org/10.1016/j.apsusc.2016.06.176.

(47) Brousse, T.; Bélanger, D.; Long, J. W. To Be or Not To Be Pseudocapacitive? *J. Electrochem. Soc.* **2015**, *162* (5), A5185–A5189. https://doi.org/10.1149/2.0201505jes.

(48) Paraknowitsch, J. P.; Thomas, A. Doping Carbons beyond Nitrogen: An Overview of Advanced Heteroatom Doped Carbons with Boron, Sulphur and Phosphorus for Energy

Applications. *Energy Environ. Sci.* **2013**, *6* (10), 2839. https://doi.org/10.1039/c3ee41444b.

(49) Deng, Y.; Xie, Y.; Zou, K.; Ji, X. Review on Recent Advances in Nitrogen-Doped Carbons: Preparations and Applications in Supercapacitors. *J. Mater. Chem. A* **2016**, *4* (4), 1144–1173. https://doi.org/10.1039/C5TA08620E.

(50) To, J. W. F.; Chen, Z.; Yao, H.; He, J.; Kim, K.; Chou, H. H.; Pan, L.; Wilcox, J.; Cui, Y.; Bao, Z. Ultrahigh Surface Area Three-Dimensional Porous Graphitic Carbon from Conjugated Polymeric Molecular Framework. *ACS Cent. Sci.* **2015**, *1* (2), 68–76. https://doi.org/10.1021/acscentsci.5b00149.

(51) Puthusseri, D.; Aravindan, V.; Madhavi, S.; Ogale, S. Improving the Energy Density of Li-Ion Capacitors Using Polymer-Derived Porous Carbons as Cathode. *Electrochim. Acta* **2014**, *130*, 766–770. https://doi.org/10.1016/j.electacta.2014.03.079.

(52) Aida, T.; Yamada, K.; Morita, M. An Advanced Hybrid Electrochemical Capacitor That Uses a Wide Potential Range at the Positive Electrode. *Electrochem. Solid-State Lett.* **2006**, *9* (12), A534. https://doi.org/10.1149/1.2349495.

(53) Aravindan, V.; Gnanaraj, J.; Lee, Y. S.; Madhavi, S. Insertion-Type Electrodes for Nonaqueous Li-Ion Capacitors. *Chem. Rev.* **2014**, *114* (23), 11619–11635. https://doi.org/10.1021/cr5000915.

(54) Surya Bhaskaram, D.; Cheruku, R.; Govindaraj, G. Reduced Graphene Oxide Wrapped V2O5 Nanoparticles: Green Synthesis and Electrical Properties. *J. Mater. Sci. Mater. Electron.* **2016**, *27* (10), 10855–10863. https://doi.org/10.1007/s10854-016-5194-x.

(55) Lim, E.; Jo, C.; Kim, H.; Kim, M.-H.; Mun, Y.; Chun, J.; Ye, Y.; Hwang, J.; Ha, K.-S.; Roh, K. C.; Kang, K.; Yoon, S.; Lee, J. Facile Synthesis of Nb2O5@Carbon Core-Shell Nanocrystals with Controlled Crystalline Structure for High-Power Anodes in Hybrid

Supercapacitors. *ACS Nano* **2015**, *9* (7), 7497–7505. https://doi.org/10.1021/acsnano.5b02601.

(56) Zheng, J.; Ma, D.; Wu, X.; Dou, P.; Cao, Z.; Wang, C.; Xu, X. A Novel MWCNT/Nanotubular TiO2(B) Loaded with SnO2 Nanocrystals Ternary Composite as Anode Material for Lithium-Ion Batteries. *J. Mater. Sci.* **2017**, *52* (6), 3016–3027. https://doi.org/10.1007/s10853-016-0578-0.

(57) Foo, C. Y.; Sumboja, A.; Tan, D. J. H.; Wang, J.; Lee, P. S. Flexible and Highly Scalable V 2 O 5 -RGO Electrodes in an Organic Electrolyte for Supercapacitor Devices. *Adv. Energy Mater.* **2014**, *4* (12), 1400236. https://doi.org/10.1002/aenm.201400236.

(58) Nagaraju, D. H.; Wang, Q.; Beaujuge, P.; Alshareef, H. N. Two-Dimensional Heterostructures of V 2 O 5 and Reduced Graphene Oxide as Electrodes for High Energy Density Asymmetric Supercapacitors. *J. Mater. Chem. A* **2014**, *2* (40), 17146–17152. https://doi.org/10.1039/C4TA03731F.

(59) Murugan, M.; Kumar, R. M.; Alsalme, A.; Alghamdi, A.; Jayavel, R. Facile Hydrothermal Preparation of Niobium Pentaoxide Decorated Reduced Graphene Oxide Nanocomposites for Supercapacitor Applications. *Chem. Phys. Lett.* **2016**, *650*, 35–40. https://doi.org/10.1016/j.cplett.2016.02.059.

(60) Chen, Z.; Augustyn, V.; Jia, X.; Xiao, Q.; Dunn, B.; Lu, Y. High-Performance Sodium-Ion Pseudocapacitors Based on Hierarchically Porous Nanowire Composites. *ACS Nano* **2012**, *6* (5), 4319–4327. https://doi.org/10.1021/nn300920e.

(61) Karthikeyan, K.; Amaresh, S.; Aravindan, V.; Kim, H.; Kang, K. S.; Lee, Y. S. Unveiling Organic–Inorganic Hybrids as a Cathode Material for High Performance Lithium-Ion Capacitors. *J. Mater. Chem. A* **2013**, *1* (3), 707–714. https://doi.org/10.1039/C2TA00553K.

(62) Kim, T.; Jung, G.; Yoo, S.; Suh, K. S.; Ruoff, R. S. Activated Graphene-Based Carbons as Supercapacitor Electrodes with Macro- and Mesopores. *ACS Nano* **2013**, *7* (8), 6899–6905. https://doi.org/10.1021/nn402077v.

(63) Stoller, M. D.; Murali, S.; Quarles, N.; Zhu, Y.; Potts, J. R.; Zhu, X.; Ha, H.-W.; Ruoff, R. S. Activated Graphene as a Cathode Material for Li-Ion Hybrid Supercapacitors. *Phys. Chem. Chem. Phys.* **2012**, *14* (10), 3388. https://doi.org/10.1039/c2cp00017b.

(64) Zhang, J.; Yang, Z.; Wang, X.; Ren, T.; Qiao, Q. Homogeneous Sulphur-Doped Composites: Porous Carbon Materials with Unique Hierarchical Porous Nanostructure for Super-Capacitor Application. *RSC Adv.* **2016**, *6* (88), 84847–84853. https://doi.org/10.1039/C6RA17231H.

(65) Cheng, C.-F.; Chen, Y.-M.; Zou, F.; Liu, K.; Xia, Y.; Huang, Y.-F.; Tung, W.-Y.; Krishnan, M. R.; Vogt, B. D.; Wang, C.-L.; Ho, R.-M.; Zhu, Y. Li-Ion Capacitor Integrated with Nano-Network-Structured Ni/NiO/C Anode and Nitrogen-Doped Carbonized Metal–Organic Framework Cathode with High Power and Long Cyclability. *ACS Appl. Mater. Interfaces* **2019**, *11* (34), 30694–30702. https://doi.org/10.1021/acsami.9b06354.

(66) Wang, H.; Xu, Z.; Li, Z.; Cui, K.; Ding, J.; Kohandehghan, A.; Tan, X.; Zahiri, B.; Olsen, B. C.; Holt, C. M. B.; Mitlin, D. Hybrid Device Employing Three-Dimensional Arrays of MnO in Carbon Nanosheets Bridges Battery–Supercapacitor Divide. *Nano Lett.* **2014**, *14* (4), 1987–1994. https://doi.org/10.1021/nl500011d.

(67) Wang, P.; Wang, R.; Lang, J.; Zhang, X.; Chen, Z.; Yan, X. Porous Niobium Nitride as a Capacitive Anode Material for Advanced Li-Ion Hybrid Capacitors with Superior Cycling Stability. *J. Mater. Chem. A* **2016**, *4* (25), 9760–9766. https://doi.org/10.1039/C6TA02971J.

(68) Dong, S.; Shen, L.; Li, H.; Nie, P.; Zhu, Y.; Sheng, Q.; Zhang, X. Pseudocapacitive Behaviours of Na 2 Ti 3 O 7 @CNT Coaxial Nanocables for High-Performance Sodium-Ion Capacitors. *J. Mater. Chem. A* **2015**, *3* (42), 21277–21283. https://doi.org/10.1039/C5TA05714K.

(69) Wang, S.; Wang, R.; Zhang, Y.; Jin, D.; Zhang, L. Scalable and Sustainable Synthesis of Carbon Microspheres via a Purification-Free Strategy for Sodium-Ion Capacitors. *J. Power Sources* **2018**, *379*, 33–40. https://doi.org/10.1016/j.jpowsour.2018.01.019.

(70) Wei, Q.; Jiang, Y.; Qian, X.; Zhang, L.; Li, Q.; Tan, S.; Zhao, K.; Yang, W.; An, Q.; Guo, J.; Mai, L. Sodium Ion Capacitor Using Pseudocapacitive Layered Ferric Vanadate Nanosheets Cathode. *iScience* **2018**, *6*, 212–221. https://doi.org/10.1016/j.isci.2018.07.020.

(71) Barpanda, P.; Oyama, G.; Nishimura, S.; Chung, S.-C.; Yamada, A. A 3.8-V Earth-Abundant Sodium Battery Electrode. *Nat. Commun.* **2014**, *5* (1), 4358. https://doi.org/10.1038/ncomms5358.

(72) Xie, X.; Zhao, M.-Q.; Anasori, B.; Maleski, K.; Ren, C. E.; Li, J.; Byles, B. W.; Pomerantseva, E.; Wang, G.; Gogotsi, Y. Porous Heterostructured MXene/Carbon Nanotube Composite Paper with High Volumetric Capacity for Sodium-Based Energy Storage Devices. *Nano Energy* **2016**, *26*, 513–523. https://doi.org/10.1016/j.nanoen.2016.06.005.

(73) Karthikeyan, K.; Amaresh, S.; Lee, S. N.; Sun, X.; Aravindan, V.; Lee, Y.-G.; Lee, Y. S. Construction of High-Energy-Density Supercapacitors from Pine-Cone-Derived High-Surface-Area Carbons. *ChemSusChem* **2014**, *7* (5), 1435–1442. https://doi.org/10.1002/cssc.201301262.

(74) Aravindan, V.; Ulaganathan, M.; Madhavi, S. Research Progress in Na-Ion Capacitors. *J.*

Mater. Chem. A **2016**, *4* (20), 7538–7548. https://doi.org/10.1039/c6ta02478e.

(75) Jayaraman, S.; Jain, A.; Ulaganathan, M.; Edison, E.; Srinivasan, M. P.; Balasubramanian, R.; Aravindan, V.; Madhavi, S. Li-Ion vs. Na-Ion Capacitors: A Performance Evaluation with Coconut Shell Derived Mesoporous Carbon and Natural Plant Based Hard Carbon. *Chem. Eng. J.* **2017**, *316*, 506–513. https://doi.org/10.1016/j.cej.2017.01.108.

(76) Ding, R.; Qi, L.; Wang, H. An Investigation of Spinel NiCo2O4 as Anode for Na-Ion Capacitors. *Electrochim. Acta* **2013**, *114*, 726–735. https://doi.org/10.1016/j.electacta.2013.10.113.

(77) Bhat, S. S. M.; Babu, B.; Feygenson, M.; Neuefeind, J. C.; Shaijumon, M. M. Nanostructured Na 2 Ti 9 O 19 for Hybrid Sodium-Ion Capacitors with Excellent Rate Capability. *ACS Appl. Mater. Interfaces* **2018**, *10* (1), 437–447. https://doi.org/10.1021/acsami.7b13300.

(78) Jiang, Y.; Shen, Y.; Dong, J.; Tan, S.; Wei, Q.; Xiong, F.; Li, Q.; Liao, X.; Liu, Z.; An, Q.; Mai, L. Surface Pseudocapacitive Mechanism of Molybdenum Phosphide for High-Energy and High-Power Sodium-Ion Capacitors. *Adv. Energy Mater.* **2019**, *9* (27), 1900967. https://doi.org/10.1002/aenm.201900967.

(79) Zhao, X.; Cai, W.; Yang, Y.; Song, X.; Neale, Z.; Wang, H.-E.; Sui, J.; Cao, G. MoSe2 Nanosheets Perpendicularly Grown on Graphene with Mo–C Bonding for Sodium-Ion Capacitors. *Nano Energy* **2018**, *47*, 224–234. https://doi.org/10.1016/j.nanoen.2018.03.002.

(80) Huang, Y.; Li, X.; Ding, R.; Ying, D.; Yan, T.; Huang, Y.; Tan, C.; Sun, X.; Gao, P.; Liu, E. Tetragonal MF2 (M=Ni, Co) Micro/Nanocrystals Anodes for Lithium/Sodium-Ion Capacitors. *Electrochim. Acta* **2020**, *329*, 135138. https://doi.org/10.1016/j.electacta.2019.135138.

(81) Yan, R.; Leus, K.; Hofmann, J. P.; Antonietti, M.; Oschatz, M. Porous Nitrogen-Doped Carbon/Carbon Nanocomposite Electrodes Enable Sodium Ion Capacitors with High Capacity and Rate Capability. *Nano Energy* **2020**, *67* (July 2019), 104240. https://doi.org/10.1016/j.nanoen.2019.104240.

(82) Wang, R.; Wang, S.; Peng, X.; Zhang, Y.; Jin, D.; Chu, P. K.; Zhang, L. Elucidating the Intercalation Pseudocapacitance Mechanism of MoS 2 –Carbon Monolayer Interoverlapped Superstructure: Toward High-Performance Sodium-Ion-Based Hybrid Supercapacitor. *ACS Appl. Mater. Interfaces* **2017**, *9* (38), 32745–32755. https://doi.org/10.1021/acsami.7b09813.

(83) Zhao, C.; Yu, C.; Zhang, M.; Sun, Q.; Li, S.; Norouzi Banis, M.; Han, X.; Dong, Q.; Yang, J.; Wang, G.; Sun, X.; Qiu, J. Enhanced Sodium Storage Capability Enabled by Super Wide-Interlayer-Spacing MoS2 Integrated on Carbon Fibers. *Nano Energy* **2017**, *41* (June), 66–74. https://doi.org/10.1016/j.nanoen.2017.08.030.

(84) Zhao, Q.; Yang, D.; Whittaker, A. K.; Zhao, X. S. A Hybrid Sodium-Ion Capacitor with Polyimide as Anode and Polyimide-Derived Carbon as Cathode. *J. Power Sources* **2018**, *396*, 12–18. https://doi.org/10.1016/j.jpowsour.2018.06.010.

(85) Goldstein, J. I.; Newbury, D. E.; Echlin, P.; Joy, D. C.; Lyman, C. E.; Lifshin, E.; Sawyer, L.; Michael, J. R. *Scanning Electron Microscopy and X-Ray Microanalysis*; Springer US: Boston, MA, 2003. https://doi.org/10.1007/978-1-4615-0215-9.

(86) Severin, K. P. *Energy Dispersive Spectrometry of Common Rock Forming Minerals*; KLUWER ACADEMIC PUBLISHERS, 2004.

(87) Reimer, Ludwig, Kohl, H. *Transmission Electron Microscopy*; Springer Series in Optical Sciences; Springer New York: New York, NY, 2008; Vol. 36. https://doi.org/10.1007/978-

0-387-40093-8.

(88) Hollinger, G. Photoelectron Spectroscopies: Probes of Chemical Bonding and Electronic Properties at Semiconductor Interfaces; 1987; pp 210–231. https://doi.org/10.1007/978-3-642-72967-6_18.

(89) Fadley, C. S.; Baird, R. J.; Siekhaus, W.; Novakov, T.; Bergström, S. Å. L. Surface Analysis and Angular Distributions in X-Ray Photoelectron Spectroscopy. *J. Electron Spectros. Relat. Phenomena* **1974**, *4* (2), 93–137. https://doi.org/10.1016/0368-2048(74)90001-2.

(90) Groen, J. C.; Peffer, L. A. .; Pérez-Ramírez, J. Pore Size Determination in Modified Micro- and Mesoporous Materials. Pitfalls and Limitations in Gas Adsorption Data Analysis. *Microporous Mesoporous Mater.* **2003**, *60* (1–3), 1–17. https://doi.org/10.1016/S1387-1811(03)00339-1.

(91) Galarneau, A.; Villemot, F.; Rodriguez, J.; Fajula, F.; Coasne, B. Validity of the T-Plot Method to Assess Microporosity in Hierarchical Micro/Mesoporous Materials. *Langmuir* **2014**, *30* (44), 13266–13274. https://doi.org/10.1021/la5026679.

(92) Bokobza, L.; Bruneel, J.-L.; Couzi, M. Raman Spectra of Carbon-Based Materials (from Graphite to Carbon Black) and of Some Silicone Composites. *C* **2015**, *1* (1), 77–94. https://doi.org/10.3390/c1010077.

(93) Zhu, Y.; Gao, T.; Fan, X.; Han, F.; Wang, C. Electrochemical Techniques for Intercalation Electrode Materials in Rechargeable Batteries. *Acc. Chem. Res.* **2017**, *50* (4), 1022–1031. https://doi.org/10.1021/acs.accounts.7b00031.

(94) Zhang, S.; Pan, N. Supercapacitors Performance Evaluation. *Adv. Energy Mater.* **2015**, *5* (6), 1401401. https://doi.org/10.1002/aenm.201401401.

(95) Stoller, M. D.; Ruoff, R. S. Best Practice Methods for Determining an Electrode Material's

Performance for Ultracapacitors. *Energy Environ. Sci.* **2010**, *3* (9), 1294. https://doi.org/10.1039/c0ee00074d.

(96) Gogotsi, Y.; Simon, P. True Performance Metrics in Electrochemical Energy Storage. *Science (80-.).* **2011**, *334* (6058), 917–918. https://doi.org/10.1126/science.1213003.

(97) SIMON, P.; GOGOTSI, Y. Materials for Electrochemical Capacitors. In *Materials for Sustainable Energy*; Co-Published with Macmillan Publishers Ltd, UK, 2010; pp 138–147. https://doi.org/10.1142/9789814317665_0021.

(98) Zhang, Y.; Jiang, J.; An, Y.; Wu, L.; Dou, H.; Zhang, J.; Zhang, Y.; Wu, S.; Dong, M.; Zhang, X.; Guo, Z. Sodium-Ion Capacitors: Materials, Mechanism, and Challenges. *ChemSusChem* **2020**, 1–19. https://doi.org/10.1002/cssc.201903440.

(99) Liu, C.; Koyyalamudi, B. B.; Li, L.; Emani, S.; Wang, C.; Shaw, L. L. Improved Capacitive Energy Storage via Surface Functionalization of Activated Carbon as Cathodes for Lithium Ion Capacitors. *Carbon N. Y.* **2016**, *109*, 163–172. https://doi.org/10.1016/j.carbon.2016.07.071.

(100) Su, F.; Poh, C. K.; Chen, J. S.; Xu, G.; Wang, D.; Li, Q.; Lin, J.; Lou, X. W. Nitrogen-Containing Microporous Carbon Nanospheres with Improved Capacitive Properties. *Energy Environ. Sci.* **2011**, *4* (3), 717–724. https://doi.org/10.1039/C0EE00277A.

(101) Shen, Z.; Xue, R. Preparation of Activated Mesocarbon Microbeads with High Mesopore Content. *Fuel Process. Technol.* **2003**, *84* (1–3), 95–103. https://doi.org/10.1016/S0378-3820(03)00050-X.

(102) Long, C.; Chen, X.; Jiang, L.; Zhi, L.; Fan, Z. Porous Layer-Stacking Carbon Derived from in-Built Template in Biomass for High Volumetric Performance Supercapacitors. *Nano Energy* **2015**, *12*, 141–151. https://doi.org/10.1016/j.nanoen.2014.12.014.

(103) Li, Z.; Xu, Z.; Tan, X.; Wang, H.; Holt, C. M. B.; Stephenson, T.; Olsen, B. C.; Mitlin, D. Mesoporous Nitrogen-Rich Carbons Derived from Protein for Ultra-High Capacity Battery Anodes and Supercapacitors. *Energy Environ. Sci.* **2013**, *6* (3), 871. https://doi.org/10.1039/c2ee23599d.

(104) Quílez-Bermejo, J.; González-Gaitán, C.; Morallón, E.; Cazorla-Amorós, D. Effect of Carbonization Conditions of Polyaniline on Its Catalytic Activity towards ORR. Some Insights about the Nature of the Active Sites. *Carbon N. Y.* **2017**, *119*, 62–71. https://doi.org/10.1016/j.carbon.2017.04.015.

(105) Yu, F.; Liu, Z.; Zhou, R.; Tan, D.; Wang, H.; Wang, F. Pseudocapacitance Contribution in Boron-Doped Graphite Sheets for Anion Storage Enables High-Performance Sodium-Ion Capacitors. *Mater. Horizons* **2018**, *5* (3), 529–535. https://doi.org/10.1039/C8MH00156A.

(106) Hemmati, S.; Li, G.; Wang, X.; Ding, Y.; Pei, Y.; Yu, A.; Chen, Z. 3D N-Doped Hybrid Architectures Assembled from 0D T-Nb2O5 Embedded in Carbon Microtubes toward High-Rate Li-Ion Capacitors. *Nano Energy* **2019**, *56* (August 2018), 118–126. https://doi.org/10.1016/j.nanoen.2018.10.048.

(107) Jezowski, P.; Crosnier, O.; Deunf, E.; Poizot, P.; Béguin, F.; Brousse, T. Safe and Recyclable Lithium-Ion Capacitors Using Sacrificial Organic Lithium Salt. *Nat. Mater.* **2018**, *17* (2), 167–173. https://doi.org/10.1038/NMAT5029.

(108) Yao, F.; Pham, D. T.; Lee, Y. H. Carbon-Based Materials for Lithium-Ion Batteries, Electrochemical Capacitors, and Their Hybrid Devices. *ChemSusChem* **2015**, *8* (14), 2284–2311. https://doi.org/10.1002/cssc.201403490.

(109) Gu, H.; Zhu, Y.-E.; Yang, J.; Wei, J.; Zhou, Z. Nanomaterials and Technologies for Lithium-Ion Hybrid Supercapacitors. *ChemNanoMat* **2016**, *2* (7), 578–587.

https://doi.org/10.1002/cnma.201600068.

(110) Augustyn, V.; Come, J.; Lowe, M. A.; Kim, J. W.; Taberna, P.-L.; Tolbert, S. H.; Abruña, H. D.; Simon, P.; Dunn, B. High-Rate Electrochemical Energy Storage through Li+ Intercalation Pseudocapacitance. *Nat. Mater.* **2013**, *12* (6), 518–522. https://doi.org/10.1038/nmat3601.

(111) Kim, J. W.; Augustyn, V.; Dunn, B. The Effect of Crystallinity on the Rapid Pseudocapacitive Response of Nb 2O 5. *Adv. Energy Mater.* **2012**, *2* (1), 141–148. https://doi.org/10.1002/aenm.201100494.

(112) Yan, L.; Rui, X.; Chen, G.; Xu, W.; Zou, G.; Luo, H. Recent Advances in Nanostructured Nb-Based Oxides for Electrochemical Energy Storage. *Nanoscale* **2016**, *8* (16), 8443–8465. https://doi.org/10.1039/C6NR01340F.

(113) Kim, K.; Woo, S.-G.; Jo, Y. N.; Lee, J.; Kim, J.-H. Niobium Oxide Nanoparticle Core–Amorphous Carbon Shell Structure for Fast Reversible Lithium Storage. *Electrochim. Acta* **2017**, *240*, 316–322. https://doi.org/10.1016/j.electacta.2017.04.051.

(114) Wang, X.; Li, G.; Chen, Z.; Augustyn, V.; Ma, X.; Wang, G.; Dunn, B.; Lu, Y. High-Performance Supercapacitors Based on Nanocomposites of Nb2O5 Nanocrystals and Carbon Nanotubes. *Adv. Energy Mater.* **2011**, *1* (6), 1089–1093. https://doi.org/10.1002/aenm.201100332.

(115) Chen, Z.; Li, H.; Lu, X.; Wu, L.; Jiang, J.; Jiang, S.; Wang, J.; Dou, H.; Zhang, X. Nitrogenated Urchin-like Nb 2 O 5 Microspheres with Extraordinary Pseudocapacitive Properties for Lithium-Ion Capacitors. *ChemElectroChem* **2018**, *5* (11), 1516–1524. https://doi.org/10.1002/celc.201701390.

(116) Wang, X.; Yan, C.; Yan, J.; Sumboja, A.; Lee, P. S. Orthorhombic Niobium Oxide

Nanowires for next Generation Hybrid Supercapacitor Device. *Nano Energy* **2015**, *11*, 765–772. https://doi.org/10.1016/j.nanoen.2014.11.020.

(117) Lai, C.-H.; Ashby, D.; Moz, M.; Gogotsi, Y.; Pilon, L.; Dunn, B. Designing Pseudocapacitance for Nb 2 O 5 /Carbide-Derived Carbon Electrodes and Hybrid Devices. *Langmuir* **2017**, *33* (37), 9407–9415. https://doi.org/10.1021/acs.langmuir.7b01110.

(118) Lim, E.; Kim, H.; Jo, C.; Chun, J.; Ku, K.; Kim, S.; Lee, H. I.; Nam, I. S.; Yoon, S.; Kang, K.; Lee, J. Advanced Hybrid Supercapacitor Based on a Mesoporous Niobium Pentoxide/Carbon as High-Performance Anode. *ACS Nano* **2014**, *8* (9), 8968–8978. https://doi.org/10.1021/nn501972w.

(119) Chen, D.; Wang, J.-H.; Chou, T.-F.; Zhao, B.; El-Sayed, M. A.; Liu, M. Unraveling the Nature of Anomalously Fast Energy Storage in T-Nb 2 O 5. *J. Am. Chem. Soc.* **2017**, *139* (20), 7071–7081. https://doi.org/10.1021/jacs.7b03141.

(120) Lee, W. J.; Maiti, U. N.; Lee, J. M.; Lim, J.; Han, T. H.; Kim, S. O. Nitrogen-Doped Carbon Nanotubes and Graphene Composite Structures for Energy and Catalytic Applications. *Chem. Commun.* **2014**, *50* (52), 6818. https://doi.org/10.1039/c4cc00146j.

(121) Li, L.; Peng, S.; Lee, J. K. Y.; Ji, D.; Srinivasan, M.; Ramakrishna, S. Electrospun Hollow Nanofibers for Advanced Secondary Batteries. *Nano Energy* **2017**, *39* (June), 111–139. https://doi.org/10.1016/j.nanoen.2017.06.050.

(122) Ōya, A.; Marsh, H. Phenomena of Catalytic Graphitization. *J. Mater. Sci.* **1982**, *17* (2), 309–322. https://doi.org/10.1007/BF00591464.

(123) Bitencourt, C. S.; Luz, A. P.; Pagliosa, C.; Pandolfelli, V. C. Role of Catalytic Agents and Processing Parameters in the Graphitization Process of a Carbon-Based Refractory Binder. *Ceram. Int.* **2015**, *41* (10), 13320–13330. https://doi.org/10.1016/j.ceramint.2015.07.115.

(124) Atchudan, R.; Perumal, S.; Karthikeyan, D.; Pandurangan, A.; Lee, Y. R. Synthesis and Characterization of Graphitic Mesoporous Carbon Using Metal-Metal Oxide by Chemical Vapor Deposition Method. *Microporous Mesoporous Mater.* **2015**, *215*, 123–132. https://doi.org/10.1016/j.micromeso.2015.05.032.

(125) Murayama, T.; Chen, J.; Hirata, J.; Matsumoto, K.; Ueda, W. Hydrothermal Synthesis of Octahedra-Based Layered Niobium Oxide and Its Catalytic Activity as a Solid Acid. *Catal. Sci. Technol.* **2014**, *4* (12), 4250–4257. https://doi.org/10.1039/C4CY00713A.

(126) Zhao, W.; Zhao, W.; Zhu, G.; Lin, T.; Xu, F.; Huang, F. Black Nb $_2$ O $_5$ Nanorods with Improved Solar Absorption and Enhanced Photocatalytic Activity. *Dalt. Trans.* **2016**, *45* (9), 3888–3894. https://doi.org/10.1039/C5DT04578A.

(127) Arunkumar, P. . b; Ashish, A. G. .; Babu, B. .; Sarang, S. .; Suresh, A. .; Sharma, C. H. .; Thalakulam, M. .; Shaijumon, M. M. . Nb2O5/Graphene Nanocomposites for Electrochemical Energy Storage. *RSC Adv.* **2015**, *5* (74), 59997–60004. https://doi.org/10.1039/c5ra07895d.

(128) Deng, B.; Lei, T.; Zhu, W.; Xiao, L.; Liu, J. In-Plane Assembled Orthorhombic Nb $_2$ O $_5$ Nanorod Films with High-Rate Li $^+$ Intercalation for High-Performance Flexible Li-Ion Capacitors. *Adv. Funct. Mater.* **2017**, *1704330*, 1704330. https://doi.org/10.1002/adfm.201704330.

(129) Huang, H.; Wang, C.; Huang, J.; Wang, X.; Du, Y.; Yang, P. Structure Inherited Synthesis of N-Doped Highly Ordered Mesoporous Nb $_2$ O $_5$ as Robust Catalysts for Improved Visible Light Photoactivity. *Nanoscale* **2014**, *6* (13), 7274–7280. https://doi.org/10.1039/C4NR00505H.

(130) Kulkarni, A. K.; Praveen, C. S.; Sethi, Y. A.; Panmand, R. P.; Arbuj, S. S.; Naik, S. D.;

Ghule, A. V.; Kale, B. B. Nanostructured N-Doped Orthorhombic Nb $_2$ O $_5$ as an Efficient Stable Photocatalyst for Hydrogen Generation under Visible Light. *Dalt. Trans.* **2017**, *46* (43), 14859–14868. https://doi.org/10.1039/C7DT02611K.

(131) Biemolt, J.; Denekamp, I. M.; Slot, T. K.; Rothenberg, G.; Eisenberg, D. Boosting the Supercapacitance of Nitrogen-Doped Carbon by Tuning Surface Functionalities. *ChemSusChem* **2017**, *10* (20), 4018–4024. https://doi.org/10.1002/cssc.201700902.

(132) Wang, R.; Zhu, Y.; Qiu, Y.; Leung, C. F.; He, J.; Liu, G.; Lau, T. C. Synthesis of Nitrogen-Doped KNbO3 Nanocubes with High Photocatalytic Activity for Water Splitting and Degradation of Organic Pollutants under Visible Light. *Chem. Eng. J.* **2013**, *226*, 123–130. https://doi.org/10.1016/j.cej.2013.04.049.

(133) Lou, S.; Cheng, X.; Zhao, Y.; Lushington, A.; Gao, J.; Li, Q.; Zuo, P.; Wang, B.; Gao, Y.; Ma, Y.; Du, C.; Yin, G.; Sun, X. Superior Performance of Ordered Macroporous TiNb2O7anodes for Lithium Ion Batteries: Understanding from the Structural and Pseudocapacitive Insights on Achieving High Rate Capability. *Nano Energy* **2017**, *34* (February), 15–25. https://doi.org/10.1016/j.nanoen.2017.01.058.

(134) Wang, J.; Polleux, J.; Lim, J.; Dunn, B. Pseudocapacitive Contributions to Electrochemical Energy Storage in TiO2 (Anatase) Nanoparticles. *J. Phys. Chem. C* **2007**, *111* (40), 14925–14931. https://doi.org/10.1021/jp074464w.

(135) Petkovich, N. D.; Rudisill, S. G.; Wilson, B. E.; Mukherjee, A.; Stein, A. Control of TiO2 Grain Size and Positioning in Three-Dimensionally Ordered Macroporous TiO2/C Composite Anodes for Lithium Ion Batteries. *Inorg. Chem.* **2014**, *53* (2), 1100–1112. https://doi.org/10.1021/ic402648f.

(136) Song, M. Y.; Kim, N. R.; Yoon, H. J.; Cho, S. Y.; Jin, H. J.; Yun, Y. S. Long-Lasting

Nb2o5-Based Nanocomposite Materials for Li-Ion Storage. *ACS Appl. Mater. Interfaces* **2017**, *9* (3), 2267–2274. https://doi.org/10.1021/acsami.6b11444.

(137) Wang, J.; Li, H.; Shen, L.; Dong, S.; Zhang, X. Nb $_2$ O $_5$ Nanoparticles Encapsulated in Ordered Mesoporous Carbon Matrix as Advanced Anode Materials for Li Ion Capacitors. *RSC Adv.* **2016**, *6* (75), 71338–71344. https://doi.org/10.1039/C6RA11460A.

(138) Kim, H.; Kim, H.; Ding, Z.; Lee, M. H.; Lim, K.; Yoon, G.; Kang, K. Recent Progress in Electrode Materials for Sodium-Ion Batteries. *Adv. Energy Mater.* **2016**, *6* (19), 1600943. https://doi.org/10.1002/aenm.201600943.

(139) Xu, Z.; Park, J.; Yoon, G.; Kim, H.; Kang, K. Graphitic Carbon Materials for Advanced Sodium-Ion Batteries. *Small Methods* **2019**, *3* (4), 1800227. https://doi.org/10.1002/smtd.201800227.

(140) Kim, J.; Choi, M. S.; Shin, K. H.; Kota, M.; Kang, Y.; Lee, S.; Lee, J. Y.; Park, H. S. Rational Design of Carbon Nanomaterials for Electrochemical Sodium Storage and Capture. *Adv. Mater.* **2019**, *31* (34), 1803444. https://doi.org/10.1002/adma.201803444.

(141) Fang, S.; Bresser, D.; Passerini, S. Transition Metal Oxide Anodes for Electrochemical Energy Storage in Lithium- and Sodium-Ion Batteries. *Adv. Energy Mater.* **2020**, *10* (1), 1902485. https://doi.org/10.1002/aenm.201902485.

(142) Mukherjee, S.; Turnley, J.; Mansfield, E.; Holm, J.; Soares, D.; David, L.; Singh, G. Exfoliated Transition Metal Dichalcogenide Nanosheets for Supercapacitor and Sodium Ion Battery Applications. *R. Soc. Open Sci.* **2019**, *6* (8), 190437. https://doi.org/10.1098/rsos.190437.

(143) Li, G.; Luo, D.; Wang, X.; Seo, M. H.; Hemmati, S.; Yu, A.; Chen, Z. Enhanced Reversible Sodium-Ion Intercalation by Synergistic Coupling of Few-Layered MoS2 and S-Doped

Graphene. *Adv. Funct. Mater.* **2017**, *27* (40), 1–8. https://doi.org/10.1002/adfm.201702562.

(144) Li, Q.; Yao, Z.; Wu, J.; Mitra, S.; Hao, S.; Sahu, T. S.; Li, Y.; Wolverton, C.; Dravid, V. P. Intermediate Phases in Sodium Intercalation into MoS2 Nanosheets and Their Implications for Sodium-Ion Batteries. *Nano Energy* **2017**, *38* (June), 342–349. https://doi.org/10.1016/j.nanoen.2017.05.055.

(145) Li, H.; Ma, L.; Chen, W.; Wang, J. Synthesis of MoS2/C Nanocomposites by Hydrothermal Route Used as Li-Ion Intercalation Electrode Materials. *Mater. Lett.* **2009**, *63* (15), 1363–1365. https://doi.org/10.1016/j.matlet.2009.03.017.

(146) Sun, D.; Ye, D.; Liu, P.; Tang, Y.; Guo, J.; Wang, L.; Wang, H. MoS 2 /Graphene Nanosheets from Commercial Bulky MoS 2 and Graphite as Anode Materials for High Rate Sodium-Ion Batteries. *Adv. Energy Mater.* **2018**, *8* (10), 1702383. https://doi.org/10.1002/aenm.201702383.

(147) Wang, S.; Zhu, J.; Shao, Y.; Li, W.; Wu, Y.; Zhang, L.; Hao, X. Three-Dimensional MoS2@CNT/RGO Network Composites for High-Performance Flexible Supercapacitors. *Chem. - A Eur. J.* **2017**, *23* (14), 3438–3446. https://doi.org/10.1002/chem.201605465.

(148) Wang, Y.; Qu, Q.; Li, G.; Gao, T.; Qian, F.; Shao, J.; Liu, W.; Shi, Q.; Zheng, H. 3D Interconnected and Multiwalled Carbon@MoS 2 @Carbon Hollow Nanocables as Outstanding Anodes for Na-Ion Batteries. *Small* **2016**, *12* (43), 6033–6041. https://doi.org/10.1002/smll.201602268.

(149) Wang, T.; Liu, C.; Xu, J.; Zhu, Z.; Liu, E.; Hu, Y.; Li, C.; Jiang, F. Thermoelectric Performance of Restacked MoS 2 Nanosheets Thin-Film. *Nanotechnology* **2016**, *27* (28), 285703. https://doi.org/10.1088/0957-4484/27/28/285703.

(150) Fan, X.; Xu, P.; Zhou, D.; Sun, Y.; Li, Y. C.; Nguyen, M. A. T.; Terrones, M.; Mallouk, T.

E. Fast and Efficient Preparation of Exfoliated 2H MoS 2 Nanosheets by Sonication-Assisted Lithium Intercalation and Infrared Laser-Induced 1T to 2H Phase Reversion. *Nano Lett.* **2015**, *15* (9), 5956–5960. https://doi.org/10.1021/acs.nanolett.5b02091.

(151) Yang, Q.; Wang, Z.; Dong, L.; Zhao, W.; Jin, Y.; Fang, L.; Hu, B.; Dong, M. Activating MoS 2 with Super-High Nitrogen-Doping Concentration as Efficient Catalyst for Hydrogen Evolution Reaction. *J. Phys. Chem. C* **2019**, *123* (17), 10917–10925. https://doi.org/10.1021/acs.jpcc.9b00059.

(152) Wang, J.; Luo, C.; Gao, T.; Langrock, A.; Mignerey, A. C.; Wang, C. An Advanced MoS 2 /Carbon Anode for High-Performance Sodium-Ion Batteries. *Small* **2015**, *11* (4), 473–481. https://doi.org/10.1002/smll.201401521.

(153) Yang, M.; Zhou, Z. Recent Breakthroughs in Supercapacitors Boosted by Nitrogen-Rich Porous Carbon Materials. *Adv. Sci.* **2017**, *4* (8), 1600408. https://doi.org/10.1002/advs.201600408.

(154) Wei, Y.; Kong, Z.; Pan, Y.; Cao, Y.; Long, D.; Wang, J.; Qiao, W.; Ling, L. Sulfur Film Sandwiched between Few-Layered MoS 2 Electrocatalysts and Conductive Reduced Graphene Oxide as a Robust Cathode for Advanced Lithium–Sulfur Batteries. *J. Mater. Chem. A* **2018**, *6* (14), 5899–5909. https://doi.org/10.1039/C8TA00222C.

(155) Lu, Y.; Zhao, Q.; Zhang, N.; Lei, K.; Li, F.; Chen, J. Facile Spraying Synthesis and High-Performance Sodium Storage of Mesoporous MoS 2 /C Microspheres. *Adv. Funct. Mater.* **2016**, *26* (6), 911–918. https://doi.org/10.1002/adfm.201504062.

(156) Li, M.; Wu, Z.; Wang, Z.; Yu, S.; Zhu, Y.; Nan, B.; Shi, Y.; Gu, Y.; Liu, H.; Tang, Y.; Lu, Z. Facile Synthesis of Ultrathin MoS 2 /C Nanosheets for Use in Sodium-Ion Batteries. *RSC Adv.* **2017**, *7* (1), 285–289. https://doi.org/10.1039/C6RA24800D.

(157) Qin, W.; Chen, T.; Pan, L.; Niu, L.; Hu, B.; Li, D.; Li, J.; Sun, Z. MoS2-Reduced Graphene Oxide Composites via Microwave Assisted Synthesis for Sodium Ion Battery Anode with Improved Capacity and Cycling Performance. *Electrochim. Acta* **2015**, *153*, 55–61. https://doi.org/10.1016/j.electacta.2014.11.034.

(158) Xiao, B.; Rojo, T.; Li, X. Hard Carbon as Sodium-Ion Battery Anodes: Progress and Challenges. *ChemSusChem* **2019**, *12* (1), 133–144. https://doi.org/10.1002/cssc.201801879.

(159) Luo, F.; Xia, X.; Zeng, L.; Chen, X.; Feng, X.; Wang, J.; Xu, L.; Qian, Q.; Wei, M.; Chen, Q. A Composite of Ultra-Fine Few-Layer MoS 2 Structures Embedded on N,P-Co-Doped Bio-Carbon for High-Performance Sodium-Ion Batteries. *New J. Chem.* **2020**, *44* (5), 2046–2052. https://doi.org/10.1039/C9NJ05921K.

(160) Muñoz-Márquez, M. Á.; Saurel, D.; Gómez-Cámer, J. L.; Casas-Cabanas, M.; Castillo-Martínez, E.; Rojo, T. Na-Ion Batteries for Large Scale Applications: A Review on Anode Materials and Solid Electrolyte Interphase Formation. *Adv. Energy Mater.* **2017**, *7* (20), 1700463. https://doi.org/10.1002/aenm.201700463.

(161) Chen, Z.; Yin, D.; Zhang, M. Sandwich-like MoS 2 @SnO 2 @C with High Capacity and Stability for Sodium/Potassium Ion Batteries. *Small* **2018**, *14* (17), 1703818. https://doi.org/10.1002/smll.201703818.

(162) Verma, A.; Smith, K.; Santhanagopalan, S.; Abraham, D.; Yao, K. P.; Mukherjee, P. P. Galvanostatic Intermittent Titration and Performance Based Analysis of LiNi 0.5 Co 0.2 Mn 0.3 O 2 Cathode. *J. Electrochem. Soc.* **2017**, *164* (13), A3380–A3392. https://doi.org/10.1149/2.1701713jes.

(163) Bucher, N.; Hartung, S.; Franklin, J. B.; Wise, A. M.; Lim, L. Y.; Chen, H.-Y.; Weker, J.

N.; Toney, M. F.; Srinivasan, M. P2–Na x Co y Mn 1– y O 2 (y = 0, 0.1) as Cathode Materials in Sodium-Ion Batteries—Effects of Doping and Morphology To Enhance Cycling Stability. *Chem. Mater.* **2016**, *28* (7), 2041–2051. https://doi.org/10.1021/acs.chemmater.5b04557.

(164) Wu, J.; Liu, J.; Cui, J.; Yao, S.; Ihsan-Ul-Haq, M.; Mubarak, N.; Quattrocchi, E.; Ciucci, F.; Kim, J.-K. Dual-Phase MoS 2 as a High-Performance Sodium-Ion Battery Anode. *J. Mater. Chem. A* **2020**, *8* (4), 2114–2122. https://doi.org/10.1039/C9TA11913B.

(165) Li, Y.; Liang, Y.; Robles Hernandez, F. C.; Deog Yoo, H.; An, Q.; Yao, Y. Enhancing Sodium-Ion Battery Performance with Interlayer-Expanded MoS2–PEO Nanocomposites. *Nano Energy* **2015**, *15*, 453–461. https://doi.org/10.1016/j.nanoen.2015.05.012.

(166) Bommier, C.; Surta, T. W.; Dolgos, M.; Ji, X. New Mechanistic Insights on Na-Ion Storage in Nongraphitizable Carbon. *Nano Lett.* **2015**, *15* (9), 5888–5892. https://doi.org/10.1021/acs.nanolett.5b01969.

(167) Xie, X.; Ao, Z.; Su, D.; Zhang, J.; Wang, G. MoS 2 /Graphene Composite Anodes with Enhanced Performance for Sodium-Ion Batteries: The Role of the Two-Dimensional Heterointerface. *Adv. Funct. Mater.* **2015**, *25* (9), 1393–1403. https://doi.org/10.1002/adfm.201404078.

(168) Thangavel, R.; Moorthy, B.; Kim, D. K.; Lee, Y.-S. Pushing the Energy Output and Cyclability of Sodium Hybrid Capacitors at High Power to New Limits. *Adv. Energy Mater.* **2017**, *7* (14), 1602654. https://doi.org/10.1002/aenm.201602654.

(169) Moeez, I.; Jung, H.; Lim, H.; Chung, K. Y. Presodiation Strategies and Their Effect on Electrode–Electrolyte Interphases for High-Performance Electrodes for Sodium-Ion Batteries. *ACS Appl. Mater. Interfaces* **2019**, *11* (44), 41394–41401.

https://doi.org/10.1021/acsami.9b14381.

(170) Li, H.; Zhu, Y.; Dong, S.; Shen, L.; Chen, Z.; Zhang, X.; Yu, G. Self-Assembled Nb2O5 Nanosheets for High Energy-High Power Sodium Ion Capacitors. *Chem. Mater.* **2016**, *28* (16), 5753–5760. https://doi.org/10.1021/acs.chemmater.6b01988.

(171) Chen, H.; Dai, C.; Li, Y.; Zhan, R.; Wang, M.-Q.; Guo, B.; Zhang, Y.; Liu, H.; Xu, M.; Bao, S. An Excellent Full Sodium-Ion Capacitor Derived from a Single Ti-Based Metal–Organic Framework. *J. Mater. Chem. A* **2018**, *6* (48), 24860–24868. https://doi.org/10.1039/C8TA09072F.

(172) Jian, Z.; Raju, V.; Li, Z.; Xing, Z.; Hu, Y.-S.; Ji, X. A High-Power Symmetric Na-Ion Pseudocapacitor. *Adv. Funct. Mater.* **2015**, *25* (36), 5778–5785. https://doi.org/10.1002/adfm.201502433.